

CAPITAL UNIVERSITY OF SCIENCE AND  
TECHNOLOGY, ISLAMABAD



# Elevated Temperature Modeling of Wide Bandgap High Electron Mobility Transistors

by

Muhammad Naeem Khan

A thesis submitted in partial fulfillment for the  
degree of Doctor of Philosophy

in the

Faculty of Engineering

Department of Electrical Engineering

2018

# Elevated Temperature Modeling of Wide Bandgap High Electron Mobility Transistors

By

Muhammad Naeem Khan

(PE-141005)

Prof. Dr. Jianiun Gao, PhD

East China Normal University, P. R. China

Dr. Arif Khan

Charles Sturt University, Australia

Prof. Dr. M. Mansoor Ahmed

(Thesis Supervisor)

Prof. Dr. Noor Muhammad Khan

(Head, Department of Electrical Engineering)

Prof. Dr. Imtiaz Ahmed Taj

(Dean, Faculty of Engineering)

DEPARTMENT OF ELECTRICAL ENGINEERING  
CAPITAL UNIVERSITY OF SCIENCE AND TECHNOLOGY  
ISLAMABAD

2018

Copyright © 2018 by Muhammad Naeem Khan

All rights reserved. No part of this thesis may be reproduced, distributed, or transmitted in any form or by any means, including photocopying, recording, or other electronic or mechanical methods, by any information storage and retrieval system without the prior written permission of the author.

*Dedicated to my supervisor Prof. Dr. M. Mansoor Ahmed*



**CAPITAL UNIVERSITY OF SCIENCE & TECHNOLOGY  
ISLAMABAD**

Expressway, Kahuta Road, Zone-V, Islamabad  
Phone: +92-51-111-555-666 Fax: +92-51-4486705  
Email: [info@cust.edu.pk](mailto:info@cust.edu.pk) Website: <https://www.cust.edu.pk>

**CERTIFICATE OF APPROVAL**

This is to certify that the research work presented in the thesis, entitled “**Elevated Temperature Modeling of Wide Bandgap High Electron Mobility Transistors**” was conducted under the supervision of **Dr. Muhammad Mansoor Ahmed**. No part of this thesis has been submitted anywhere else for any other degree. This thesis is submitted to the **Department of Electrical Engineering, Capital University of Science and Technology** in partial fulfillment of the requirements for the degree of Doctor in Philosophy in the field of **Electrical Engineering**. The open defence of the thesis was conducted on **October 24, 2018**.

Student Name: Mr. Muhammad Naeem Khan (PE141005)



---

---

The Examining Committee unanimously agrees to award PhD degree in the mentioned field.

**Examination Committee :**

(a) External Examiner 1: Dr. Junaid Mughal  
Professor  
COMSATS University, Islamabad




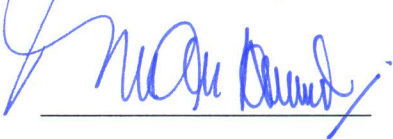
---

(b) External Examiner 2: Dr. Shabbir Majeed Chaudhry  
Associate Professor  
UET, Taxila



---

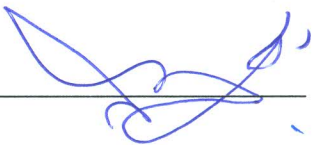
(c) Internal Examiner : Dr. Muhammad Ashraf  
Professor  
CUST, Islamabad

---

**Supervisor Name :** Dr. Muhammad Mansoor Ahmed  
Professor  
CUST, Islamabad

**Name of HoD :** Dr. Noor Muhammad Khan .  
Professor  
CUST, Islamabad



---

**Name of Dean :** Dr. Imtiaz Ahmad Taj  
Professor  
CUST, Islamabad




---

## AUTHOR'S DECLARATION

I, **Mr. Muhammad Naeem Khan** (Registration No. PE-141005), hereby state that my PhD thesis titled, '**Elevated Temperature Modeling of Wide Bandgap High Electron Mobility Transistors**' is my own work and has not been submitted previously by me for taking any degree from Capital University of Science and Technology, Islamabad or anywhere else in the country/ world.

At any time, if my statement is found to be incorrect even after my graduation, the University has the right to withdraw my PhD Degree.



(Mr. Muhammad Naeem Khan)

Dated: 24 October, 2018

Registration No : PE-141005


## PLAGIARISM UNDERTAKING

I solemnly declare that research work presented in the thesis titled “**Elevated Temperature Modeling of Wide Bandgap High Electron Mobility Transistors**” is solely my research work with no significant contribution from any other person. Small contribution/help wherever taken has been duly acknowledged and that complete thesis has been written by me.

I understand the zero tolerance policy of the HEC and Capital University of Science and Technology towards plagiarism. Therefore, I as an author of the above titled thesis declare that no portion of my thesis has been plagiarized and any material used as reference is properly referred/ cited.

I undertake that if I am found guilty of any formal plagiarism in the above titled thesis even after award of PhD Degree, the University reserves the right to withdraw/ revoke my PhD degree and that HEC and the University have the right to publish my name on the HEC/ University Website on which names of students are placed who submitted plagiarized thesis.

Dated: 24 October, 2018

  
\_\_\_\_\_  
(Mr. Muhammad Naeem Khan)  
Registration No. PE-141005

## *List of Publications*

It is certified that following publication(s) have been made out of the research work that has been carried out for this thesis:-

1. **M. N. Khan**, U. F. Ahmed, M. M. Ahmed, and S. Rehman, “An improved model to assess temperature-dependent DC characteristics of submicron GaN HEMTs,” *Journal of Computational Electronics*, vol. 17, no. 2, pp. 653–662, 2018.
2. **M. N. Khan**, U. F. Ahmed, M. M. Ahmed, and S. Rehman, “An Improved Temperature Dependent Analytical Model to Predict AlGa<sub>N</sub>/Ga<sub>N</sub> HEMTs AC Characteristics,” *Submitted to Electrical Engineering*, 2018.
3. **M. N. Khan**, U. F. Ahmed, M. M. Ahmed, and S. Rehman, “Simulation and Comparative Analysis of Submicron GaN HEMTs DC Characteristics for CAD,” *Submitted to Journal of Computational Electronics*, 2018.

**(Muhammad Naeem Khan)**

Registration No: PE-141005



## *Acknowledgements*

All praise be to almighty ALLAH who has been bestowing me with his great bounties and enabled me to complete my dissertation.

I would like to express my heartiest gratitude to my supervisor Prof. Dr. Muhammad Mansoor Ahmed, Vice Chancellor, Capital University of Science and Technology (CUST), for his efforts to established research environments and activities at CUST. It was a wonderful experience and learning opportunity to work with him as a PhD student. I am really indebted to his kind support and all out help to complete this research work successfully. His continuous encouragement, support and constructive criticism made me able to complete this task. In spite of his administrative and managerial engagements, his dedication, as a supervisor, is highly appreciable.

I would also like to extend my gratitude to the Dean Faculty of Engineering Prof. Dr. Imtiaz Ahmad Taj and Head of Department Prof. Dr. Noor M. Khan for their continuous encouragement and support during the entire span of my stay at CUST.

I feel honor to express my feeling of appreciation for the support I have received from the members of Research Group of Microelectronics and RF Engineering, especially, Mr. Umer Farooq Ahmed, Mr. Umair Rafique, Mr. Saif ur Rehman, Mr. Waseem Abbasi and Mr. Usama Munir who helped me in my research work and documentation of the thesis.

---

# Abstract

This thesis presents elevated temperature modeling of the 3<sup>rd</sup> generation wide bandgap GaN High Electron Mobility Transistors (HEMTs). In AlGa<sub>N</sub>/Ga<sub>N</sub> HEMTs, Two Dimensional Electron Gas (2-DEG) can be achieved without having a dopant layer, because of the piezoelectric effect found inherently in Ga<sub>N</sub> semiconductor. This provides an increased saturation velocity and Ga<sub>N</sub> HEMT, therefore, is a considered promising candidate for microwave power applications.

In the first part of thesis, an analytical model is developed to predict temperature dependent DC characteristics of AlGa<sub>N</sub>/Ga<sub>N</sub> HEMTs. The model comprehensively incorporates, temperature dependent variation in Schottky barrier height,  $\phi_b(T)$ ; bandgap discontinuity,  $\Delta E_c(T)$ ; sheet carrier concentration of 2-DEG,  $n_s(T)$ ; saturation velocity,  $v_{sat}(T)$  and carriers mobility,  $\mu(T)$ . It has been shown that by increasing the ambient temperature, there is a decrease in  $\phi_b$ ; an increase in  $n_s$ ; a decrease in  $v_{sat}$  of 2-DEG carriers and a decrease in  $\mu_T$ . A comparative analysis revealed that the proposed model's accuracy is at least 30% better than its counterparts.

In the second part of thesis, AlGa<sub>N</sub>/Ga<sub>N</sub> HEMTs AC characteristics are modeled by developing an analytical technique. In the proposed technique, temperature dependent  $n_s(T)$  of 2-DEG is first assessed to predict the DC characteristics of AlGa<sub>N</sub>/Ga<sub>N</sub> HEMTs. Engaging the modeled DC data and by evaluating depletion layer capacitors, device's intrinsic small signal parameters are determined. By employing assessed small signal parameters, S-parameters of the device are calculated and their compliance with the measured data ensures the validity of the proposed mechanism.

In the third part of thesis, a numerical model to simulate output and transfer characteristics of Ga<sub>N</sub> HEMTs is developed. The model takes into account dependence of output conductance on the device drain and gate bias, and simulates both positive and negative conductance to a good degree of accuracy. Appearance of peak transconductance to a relatively higher negative gate bias is a routinely

observed phenomenon in GaN HEMTs, and the proposed model has the ability to simulate such 2<sup>nd</sup> order effects with a good degree of accuracy. A comparative study revealed that the proposed model offers at least 17% improved accuracy compared to other such models reported in literature. The accuracy of the model was also checked at elevated temperature and found significantly better than its counterparts. As, the model is based on a single expression, it is therefore easy to handle with and can comfortably be used in computer aided design software to assess the temperature dependent performance of GaN HEMTs for their possible integration into power circuitries.

# Contents

<b>Author’s Declaration</b>	<b>v</b>
<b>Plagiarism Undertaking</b>	<b>vi</b>
<b>List of Publications</b>	<b>vii</b>
<b>Acknowledgments</b>	<b>viii</b>
<b>Abstract</b>	<b>ix</b>
<b>List of Figures</b>	<b>xiii</b>
<b>List of Tables</b>	<b>xvi</b>
<b>Abbreviations</b>	<b>xviii</b>
<b>Symbols</b>	<b>xx</b>
<b>1 Introduction</b>	<b>1</b>
1.1 Wide Bandgap Semiconductors . . . . .	4
1.2 Figure of Merit . . . . .	5
1.3 Carrier Concentration vs Temperature . . . . .	7
1.4 GaN HEMT . . . . .	9
1.5 Functional Description of HEMT’s Layers . . . . .	14
1.5.1 Substrate . . . . .	14
1.5.2 Nucleation Layer . . . . .	15
1.5.3 Channel Layer . . . . .	15
1.5.4 Spacer Layer . . . . .	16
1.5.5 Barrier layer . . . . .	16
1.5.6 Cap or Contact layer . . . . .	17
1.6 Spontaneous and Piezoelectric Polarization in AlGa <sub>N</sub> /Ga <sub>N</sub> HEMTs	18
1.7 Temperature Dependent Characteristics . . . . .	21
1.8 RF Performance of AlGa <sub>N</sub> /Ga <sub>N</sub> HEMTs . . . . .	24
1.9 Summary and Thesis Outline . . . . .	25

---

<b>2</b>	<b>Literature Review</b>	<b>28</b>
2.1	Introduction . . . . .	28
2.2	Wide Bandgap Semiconductors . . . . .	29
2.3	GaN Based Technology . . . . .	31
2.4	GaN HEMTs RF High Power Performance . . . . .	34
2.5	Self-Heating Effects . . . . .	37
2.6	Temperature Dependent DC Performance . . . . .	38
2.7	Temperature Dependent AC Performance . . . . .	40
2.8	AlGaN/GaN HEMTs Analytical Models . . . . .	43
2.9	AlGaN/GaN HEMTs Numerical Models . . . . .	45
2.10	Research Gaps . . . . .	47
2.11	Methodology . . . . .	49
2.12	Summary . . . . .	51
<b>3</b>	<b>HEMT's Temperature Dependent Analytical DC Model</b>	<b>53</b>
3.1	Introduction . . . . .	53
3.2	Model Development . . . . .	56
3.2.1	$I - V$ Characteristics . . . . .	63
3.2.1.1	Linear Region Current ( $V_{ds} < V_{d(sat)}$ ) . . . . .	63
3.2.1.2	Saturation Point ( $V_{ds} = V_{d(sat)}$ ) . . . . .	65
3.2.1.3	Saturation Current ( $V_{ds} > V_{d(sat)}$ ) . . . . .	67
3.3	Modeled Characteristics . . . . .	71
3.4	Summary . . . . .	80
<b>4</b>	<b>HEMT Analytical Model to Assess AC Parameters</b>	<b>82</b>
4.1	Introduction . . . . .	82
4.2	Model Development . . . . .	85
4.2.1	DC Characteristics . . . . .	87
4.2.2	AC Characteristics . . . . .	92
4.3	Result and Discussion . . . . .	98
4.4	Summary . . . . .	108
<b>5</b>	<b>Simulation and Comparative Analysis of Submicron GaN HEMTs</b>	
	<b>DC Characteristics</b>	<b>109</b>
5.1	Introduction . . . . .	109
5.2	Model Development . . . . .	112
5.2.1	Particle Swarm Optimization . . . . .	115
5.3	Results and Discussion . . . . .	118
5.4	Summary . . . . .	127
<b>6</b>	<b>Conclusion and Future Work</b>	<b>129</b>
6.1	Future Work . . . . .	134
	<b>Bibliography</b>	<b>136</b>

# List of Figures

1.1	Energy band vs. wavevector ( $k$ ) diagrams of various semiconductors: (a) Si indicating indirect bandgap of 1.1 eV, (b) Ge direct bandgap of 0.67 eV, (c) GaAs having direct bandgap of 1.43 eV and (d) GaN with a direct bandgap of 3.4 eV. It also shows that a quanta of energy is released with a de-excitation of a carrier. . . . .	3
1.2	Variation in intrinsic and extrinsic carriers concentration as a function of temperature. . . . .	8
1.3	Intrinsic carrier concentration of different semiconductor materials as a function of temperature [7]. . . . .	9
1.4	Detailed layer structure of an AlGa <sub>N</sub> /Ga <sub>N</sub> HEMT [16]. . . . .	10
1.5	Typical (a) output $I-V$ characteristics and (b) output conductance ( $g_d$ ) of a submicron ( $.25 \times 200$ ) $\mu\text{m}^2$ Ga <sub>N</sub> HEMT. . . . .	12
1.6	Typical (a) $I-V$ characteristics and (b) $g_m$ of a Ga <sub>N</sub> HEMT as a function of $V_{gs}$ . . . . .	13
1.7	Atomic layout of Ga-face and N-face of Ga <sub>N</sub> crystal, illustrating the direction and formation of spontaneous polarization, ( $P_{SP}$ ) vectors caused by non-symmetric nature of Ga <sub>N</sub> crystal [32]. . . . .	19
1.8	Pictorial illustration of spontaneous ( $P_{SP}$ ) and piezoelectric polarization ( $P_{PE}$ ) effects present in an AlGa <sub>N</sub> /Ga <sub>N</sub> HEMT structure. . . . .	20
1.9	Difference of conduction band energy levels of AlGa <sub>N</sub> and Ga <sub>N</sub> materials at thermal equilibrium, which caused formation of bandgap discontinuity, $\Delta E_c$ when both the materials brought in contact with each other; resulting into generation of 2-DEG. . . . .	21
1.10	Epitaxially grown AlGa <sub>N</sub> /Ga <sub>N</sub> layers showing polarized nature of films. At AlGa <sub>N</sub> /Ga <sub>N</sub> interface accumulation of electrons in Ga <sub>N</sub> layer get trapped into $\Delta E_c$ generating 2-DEG. . . . .	21
1.11	Experimental current-voltage characteristics at $V_{gs} = 0\text{V}$ of a submicron AlGa <sub>N</sub> /Ga <sub>N</sub> HEMT at various temperatures. . . . .	23
1.12	Breakdown voltage ( $V_{Br}$ ) vs unity gain frequency ( $f_T$ ) trend of various types of transistors commonly used in power electronics [37]. . . . .	25
3.1	Variation in Schottky barrier, $\phi_b$ and bandgap discontinuity, $\Delta E_c$ as a function of temperature for an AlGa <sub>N</sub> /Ga <sub>N</sub> heterojunction HEMT. . . . .	58
3.2	A cross-sectional view of an AlGa <sub>N</sub> /Ga <sub>N</sub> HEMT. . . . .	58
3.3	Variation in mobility, $\mu$ of an AlGa <sub>N</sub> /Ga <sub>N</sub> 2-DEG carriers as a function of temperature and gate bias. . . . .	61

3.4	Variation in $v_{sat}$ of an AlGaIn/GaN 2-DEG as a function of temperature. . . . .	62
3.5	AlGaIn/GaN HEMT with two distinct depletion layers underneath Schottky barrier gate. . . . .	68
3.6	$I_{ds} - V_{ds}$ characteristics of an AlGaIn/GaN HEMT. Experimental data from [17] represented by ( $\bullet$ ), whereas ( $-$ ) represents characteristics by the proposed model: a) at $T = 300$ K and b) at $T = 500$ K. . . . .	76
3.7	Temperature dependent $I_{ds} - V_{ds}$ characteristics of an AlGaIn/GaN HEMT for $V_{gs} = 0$ V. Experimental data from [17] represented by ( $\bullet$ ), whereas ( $-$ ) represents characteristics by the proposed model. . . . .	78
3.8	Output conductance of a submicron AlGaIn/GaN HEMT at: a) $T = 300$ K; b) $T = 400$ K and c) $T = 500$ K. ( $\bullet$ ) represents experimental data from [17] and other symbols represent modeled output conductance. . . . .	79
4.1	AC equivalent model of an AlGaIn/GaN HEMT. . . . .	93
4.2	Modeled variation in gate to source and gate to drain capacitances as a function of (a) $V_{ds}$ and (b) $V_{gs}$ for an AlGaIn/GaN HEMT. . . . .	96
4.3	Temperature dependent observed (symbols) and modeled (solid line) $I - V$ characteristics of an AlGaIn/GaN HEMT having $0.15 \mu\text{m}$ gate length where; (a) represents this work, (b) represents Wang model and (c) represents Chattopadhyay model. . . . .	99
4.4	Channel temperature vs power handling at $V_{ds} = 0$ V to $15$ V of a $0.15 \mu\text{m} \times 200 \mu\text{m}$ AlGaIn/GaN HEMT. . . . .	101
4.5	Effect of temperature on the capacitances and the transconductance of an AlGaIn/GaN HEMT having gate length $0.15 \mu\text{m}$ at $V_{ds} = 15$ V and $V_{gs} = -4.8$ V. . . . .	102
4.6	Effect of temperature on the resistances of an AlGaIn/GaN HEMT having gate length $0.15 \mu\text{m}$ at $V_{ds} = 15$ V and $V_{gs} = -4.8$ V. . . . .	104
4.7	Effect of temperature on transient time and unity gain frequency of an AlGaIn/GaN HEMT having gate length $0.15 \mu\text{m}$ at $V_{ds} = 15$ V and $V_{gs} = -4.8$ V. . . . .	105
4.8	Effect of temperature on the sheet carrier concentration and mobility of an AlGaIn/GaN HEMT having gate length $0.15 \mu\text{m}$ at $V_{ds} = 15$ V and $V_{gs} = -4.8$ V. . . . .	106
4.9	Measured [23, 141] and modeled S-parameters of $0.15 \mu\text{m}$ AlGaIn/GaN HEMT at $T = 398$ K for $V_{gs} = -4.8$ V and $V_{ds} = 15$ V. . . . .	107
5.1	Simulated (line) and observed (symbols) $I - V$ characteristics of GaN HEMTs having gate length: a) $0.25 \mu\text{m}$ ; b) $0.30 \mu\text{m}$ ; c) $0.35 \mu\text{m}$ and d) $0.70 \mu\text{m}$ . . . . .	120
5.2	Simulated and observed output conductance of GaN HEMTs having gate length: a) $0.25 \mu\text{m}$ ; b) $0.30 \mu\text{m}$ ; c) $0.35 \mu\text{m}$ and d) $0.70 \mu\text{m}$ . . . . .	123

---

5.3	Temperature dependent simulated (line) and observed (symbols) output characteristics of a $0.12 \mu\text{m}$ gate length GaN HEMT [155]: a) $T = 298 \text{ K}$ ; b) $T = 573 \text{ K}$ and c) $T = 773 \text{ K}$ . . . . .	124
5.4	Variation in transconductance as a function of temperature of a $0.12 \mu\text{m}$ gate length GaN HEMT. Lines indicate simulated results whilst symbols show experimental transconductance. . . . .	126
5.5	Slope of $I - V$ curves of GaN HEMTs and associated power after the onset of saturation at $V_{gs} = 0 \text{ V}$ . . . . .	128



# List of Tables

1.1	Comparison of different semiconductor materials properties [8]. . . . .	7
2.1	A brief overview of wide bandgap devices. . . . .	31
2.2	A brief overview of GaN based technology. . . . .	34
2.3	RF power performance of GaN-based HEMTs. . . . .	35
2.4	Effects of self-heating on the performance of GaN-based HEMTs. . .	37
2.5	Temperature dependent DC performance of GaN-based HEMTs. . .	39
2.6	Temperature dependent AC performance of GaN-based HEMTs. . .	42
2.7	Temperature dependent models of GaN-based HEMTs. . . . .	44
2.8	Non-linear models of GaN-based HEMTs. . . . .	46
3.1	Device dimensions and constants. . . . .	71
3.2	Optimized model parameters at various temperatures for an Al-GaN/GaN HEMT output characteristics. . . . .	73
3.3	Gate to source voltage ( $V_{gs}$ ) dependent simulation parameters at various temperatures for an AlGaIn/GaN submicron HEMT. . . . .	74
3.4	Comparison of various analytical models used to predict temperature dependent $I - V$ characteristics of HEMTs. . . . .	77
3.5	Comparison of RMSE of various analytical models reported in the literature for temperature dependent $I - V$ characteristics of HEMTs. . . . .	78
4.1	RMS error comparison of various models for $I - V$ characteristics of a submicron AlGaIn/GaN HEMT at $V_{gs} = 0V$ . . . . .	100
4.2	Charge density and temperature coefficient values of an AlGaIn/GaN HEMT at different ambient temperature. . . . .	102
4.3	Comparison between average RMS errors for the proposed and Alim model in assessing intrinsic small signal parameters of a GaN HEMT for temperature range 233 K to 423 K. . . . .	105
4.4	Calculated intrinsic parameters by the proposed technique at $T = 398$ K for a $0.15 \mu\text{m}$ AlGaIn/GaN HEMT at $V_{gs} = -4.8$ V and $V_{ds} = 15$ V. . . . .	106
5.1	Physical dimensions and constants of four ( $T_1 - T_4$ ) submicron GaN HEMTs, employed to establish the validity of the proposed model. . . . .	119
5.2	Optimized values for the variables of the proposed model given by Eq. (5.4) for four submicron GaN HEMTs. $I_{dss}$ is in mA. . . . .	119

---

5.3	RMS errors of different models for the device $T_1$ at $T = 298$ K. Observed average improvement in RMSE relative to the 2 <sup>nd</sup> best model is 31% and is shown in bold. . . . .	119
5.4	RMS errors in $I - V$ characteristics of different numerical models for the device $T_2$ at $T = 298$ K. Observed improvement in average RMSE relative to the 2 <sup>nd</sup> best model is 22% and is shown in bold. . . . .	120
5.5	RMS errors in $I - V$ characteristics of different numerical models for the device $T_3$ at $T = 298$ K. Observed improvement in average RMSE relative to the 2 <sup>nd</sup> best model is 17% and is shown in bold. . . . .	121
5.6	RMS errors in $I - V$ characteristics of different numerical models for device $T_4$ at $T = 298$ K. Observed improvement in average RMSE relative to 2 <sup>nd</sup> best model is 50% and is shown in bold. . . . .	122
5.7	Temperature dependent RMS errors in $I - V$ characteristics of different numerical models for a $0.12 \mu\text{m}$ gate length GaN HEMT [155] at various ambient temperatures. Lowest RMSE are shown in bold. . . . .	125
5.8	Temperature dependent RMS errors in transfer characteristics of different numerical models at $V_{ds} = 11$ V for a $0.12 \mu\text{m}$ gate length GaN HEMT [155]. Lowest RMSE are shown in bold. . . . .	127

# Abbreviations

<b>AC</b>	Alternating current
<b>AlGaN</b>	Aluminium gallium nitride
<b>Al<sub>2</sub>O<sub>3</sub></b>	Aluminium oxide
<b>AlN</b>	Aluminium nitride
<b>BJT</b>	Bipolar junction transistor
<b>BFOM</b>	Baliga figure of merit
<b>CAD</b>	Computer aided design
<b>DC</b>	Direct current
<b>EQF</b>	Eliza quality factor
<b>FOM</b>	Figure of merit
<b>GaAs</b>	Gallium arsenide
<b>GaN</b>	Gallium nitride
<b>Ge</b>	Germanium
<b>GIT</b>	Gate injection transistor
<b>HEMT</b>	High electron mobility transistor
<b>InP</b>	Indium phosphide
<b>IGBT</b>	Insulated-gate bipolar transistor
<b>JFOM</b>	Johnson figure of merit
<b><i>I-V</i></b>	Current-voltage
<b>LED</b>	Light emitting diode
<b>MATLAB</b>	Matrix laboratory
<b>MBE</b>	Molecular beam epitaxy
<b>MESFET</b>	Metal semiconductor field effect transistor
<b>MMIC</b>	Monolithic microwave integrated circuit

<b>MOS</b>	Metal oxide semiconductor
<b>MODFET</b>	Modulation doped field effect transistor
<b>MOCVD</b>	Metal organic chemical vapor
<b>MOVPE</b>	Metal organic vapor phase epitaxy
<b>PSO</b>	Particle swarm optimization
<b>RF</b>	Radio frequency
<b>RMSE</b>	Root mean square error
<b>Si, SiC</b>	Silicon and silicon carbide
<b>2-DEG</b>	Two-dimensional electron gas

# Symbols

$C_{ds}, C_{gd}, C_{gs}$	Drain-to-source, gate-to-drain and gate-to-source capacitances
$d$	Separation of the 2DEG from the Schottky barrier gate
$d_{sat}$	Height of depletion after the onset of current saturation
$E_c, E_d$	Energy of conduction and donor bands
$E_{cri}$	Critical electric field
$E_F$	Energy of fermi level
$E_g$	Bandgap of semiconductor
$E_g^A, E_g^G$	Bandgaps of AlGa <sub>N</sub> and GaN
$E_x$	Applied field inside the channel at location $x$
$E_{sat}$	Saturation field
$\Delta E_c$	Bandgap discontinuity
$f_{max}, f_T$	Maximum and unity gain frequency
$G$	Gain
$g_d$	Output conductance
$g_m, g_{m0}$	Extrinsic and intrinsic transconductance
$I_{ds}$	Drain-to-source current
$I_{d(lin)}$	Linear region current
$I_{d(sat)}$	Saturation region current
$I_{dss}$	Saturation current at $V_{gs} = 0$ V
$I_{d(sim)}, I_{d(exp)}$	Simulated and experimental current
$I_{dsT}$	Temperature dependent drain current
$J_d$	Current density

---

$k$	Boltzman constant
$k_{1,2,3}$	Constants
$\kappa$	Thermal conductivity
$L_g, \Delta L_g$	Gate length and change in gate length
$m_n^*$	Effective mass of electron
$N_d$	Doping concentration
$N_C, N_D$	Density of states available in the conduction and donor bands
$NF_{min}$	Minimum noise figure
$n_0$	Extrinsic carrier concentration
$n_s$	Sheet charge concentration
$n_i, n_r$	Intrinsic and reference carrier concentrations
$P_{dis}, P_{max}$	Dissipation and maximum power
$P_{out}$	Output power
$P_{PE}, P_{SP}$	Piezoelectric and spontaneous polarizations
$Q_g$	Charge accumulated under the Schottky barrier gate
$Q_{T(gd)}, Q_{T(gs)}$	Charges responsible in defining $C_{gd}$ and $C_{gs}$
$q$	Electron charge
$R_s, R_i$	Source and input resistances
$R_{th}$	Channel resistance
$R_{ds}$	Drain-to-source resistance
$R_{on}$	On resistance
$S_{11}, S_{12}, S_{21}, S_{22}$	Scattering parameters
$T_{sub}$	Temperature of the substrate
$T_r, T_{ch}$	Reference and channel temperatures
$T_i, T_f$	Initial and final temperatures
$T_{max}$	Maximum temperature
$\Delta T$	Change in temperature
$\tau$	Transit time
$\mu$	Carrier mobility
$\mu_0$	Constant mobility

---

$\mu_{min}, \mu_{max}$	Minimum and maximum mobilities
$\mu_T$	Temperature dependent mobility
$V_{gs}$	Gate-to-source voltage
$V_{ds}$	Drain-to-source voltage
$V_{d(sat)}$	Saturation voltage
$V_{th}$	Threshold voltage
$V(x)$	Potential drop inside the channel at location $x$
$\Delta V_{th}$	Adjustment in threshold voltage
$V_L$	Voltage at length $L$
$V_{Br}$	Breakdown voltage
$V_{ij}$	Velocity of swarm particles
$v_{sat}$	Saturation velocity
$v_0$	Velocity of 2DEG carriers
$v_{d(x)}$	Drift velocity of electrons inside the channel at location $x$
$W$	Channel width
$X_{ij}$	Position of swarm particles
$X_{best(ij)}, X_{global(ij)}$	Local and global best position of swarm particles
$Z_0$	Characteristics impedance
$\phi_b$	Schottky barrier gate
$\epsilon_s$	Permittivity of the semiconductor
$\hbar$	Plank's constant
$\sigma$	Polarization surface charge density
$\alpha, \beta, \eta, \gamma, \theta, \lambda_{1,2,3,4}$	Fitting paramters
$\lambda_c$	Heat conduction coefficient
$\lambda_m$	Thermal conductivity of semiconductor material
$\xi_{1,2,3,4}$	Temperature dependent constants

# Chapter 1

## Introduction

In a modern electronic systems, semiconductor devices are the main building blocks, which lead to more advanced electronic applications. For optimum functionality of electronic devices, it is imperative that they should be subjected to an environment, which should not exceed their normal operating limits. Because, performance of an electronic device deteriorates when operated in an extreme environment; such as high temperature, high power, etc [1]. The degradation in the characteristics and in the performance of an electronic device is primarily associated with the material chosen for its fabrication [2]. In the 1<sup>st</sup> generation monolithic electronic circuitries, devices were fabricated mostly on Silicon (Si) and rarely on Germanium (Ge); both are referred to as elemental semiconductors. Si and Ge are classified as narrow bandgap semiconductors as shown in Fig. 1.1, and it is hard for them to retain their electrical characteristics under intense conditions [3]. Thus, their use in extreme environments and in power applications is limited.

Compound semiconductors; such as Gallium Arsenide (GaAs) are considered as the 2<sup>nd</sup> generation semiconductors, which allow better mobility relative to Si and Ge; resultantly devices fabricated on compound semiconductors substituted many of the 1<sup>st</sup> generation devices, especially in the field of microwave applications. Monolithic Microwave Integrated Circuits (MMICs) is a famous example of 2<sup>nd</sup> generation semiconductor devices. In addition to enhanced drift velocity profile, GaAs and other such compound semiconductors of the 2<sup>nd</sup> generation have higher



dielectric constants than Si and Ge, which encouraged direct growth of microwave devices on such substrates. Moreover, GaAs has direct bandgap of 1.3 eV, shown in Fig. 1.1, which is relatively better than the 1<sup>st</sup> generation semiconductors, but is not enough to meet the stringent requirements imposed by the harsh environment on electronic devices [3]. Owing to that, their use in such conditions is therefore, restricted, and they also lose quite rapidly their electrical performance with deteriorating environmental conditions.

The 3<sup>rd</sup> generation semiconductors are wide bandgap ( $> 3$  eV) semiconductors; such as Silicon Carbide (SiC) and Gallium Nitride (GaN) [4–6]. Energy band diagram of GaN is shown in Fig. 1.1, which illustrates that it is a direct bandgap material having bandgap of 3.4 eV [4–6]. The 3<sup>rd</sup> generation semiconductors have better velocity-field profile than the 2<sup>nd</sup> generation semiconductors. In addition to that, they can withhold their electrical properties at much higher temperature (500 °C) compared to their counterparts [6]. Thus, preferred to be employed for the fabrication of microwave and power devices, both for room as well as for elevated temperature applications. The improved electrical performance offered by the 3<sup>rd</sup> generation semiconductors is essentially associated with their wide bandgap nature and good thermal conductivity. Good thermal conductivity allows the device to mitigate the heating effect caused by the internal field or by the external ambient temperature, and to maintain its electrical performance. Furthermore, rate of the intrinsic carriers generation in such devices, as a function of temperature, is five times lower than their competitors, ensuring their operational functionality at relatively much higher temperature compared to the conventional semiconductors devices [7].

There are numerous devices, which have been fabricated using the 3<sup>rd</sup> generation semiconductors, such as GaN and Aluminium Gallium Nitride (AlGaN) based light emitting diodes (LEDs). One of the highly fascinating examples of the 3<sup>rd</sup> generation semiconductors devices would be the heterojunction devices, where two materials, such as AlGaN and GaN, are brought together resulting in the formation of bandgap discontinuity to generate free carriers referred to as Two Dimensional Electron Gas (2-DEG). Since, the carriers trapped into the quantum

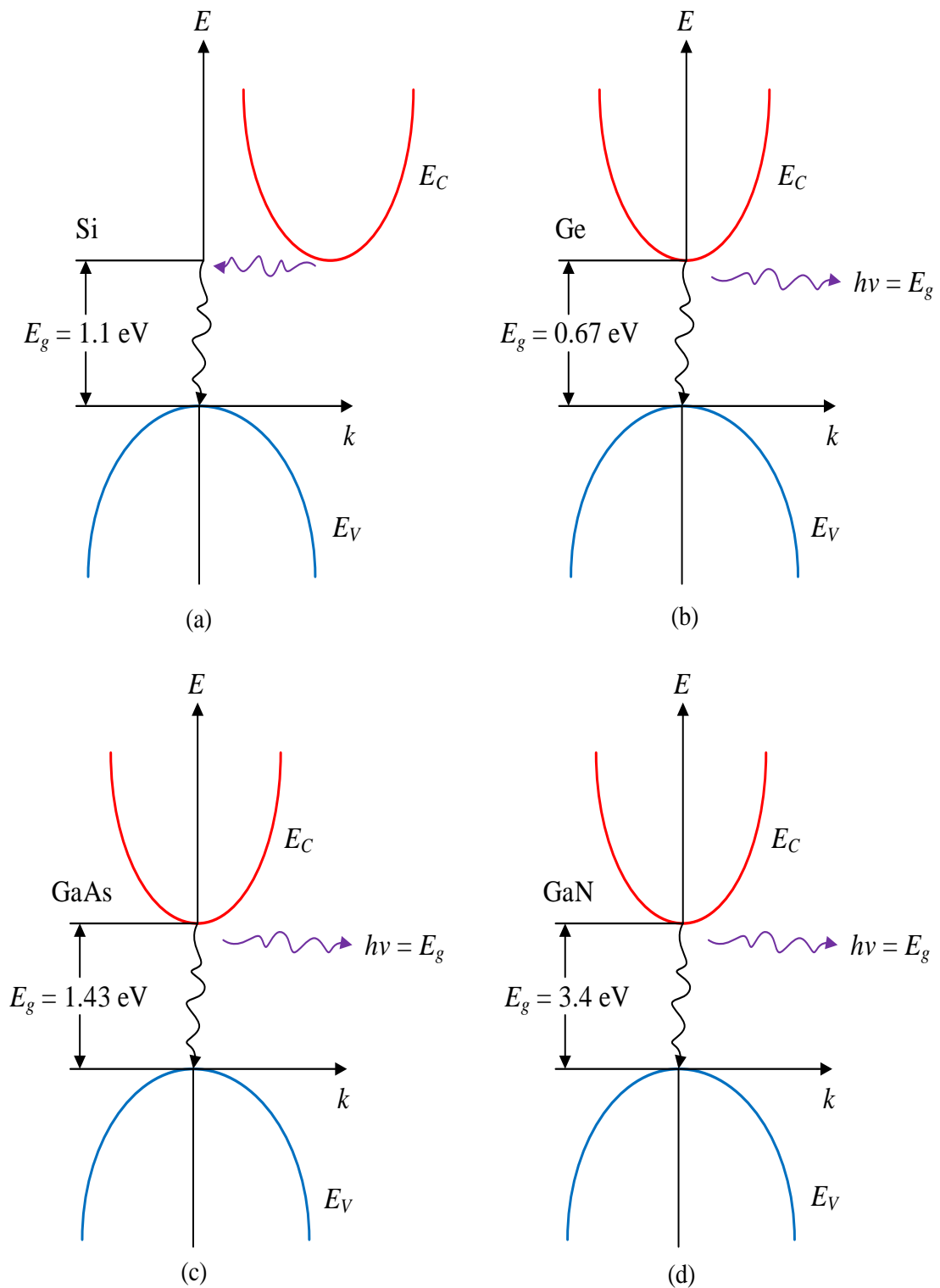


FIGURE 1.1: Energy band vs. wavevector ( $k$ ) diagrams of various semiconductors: (a) Si indicating indirect bandgap of 1.1 eV, (b) Ge direct bandgap of 0.67 eV, (c) GaAs having direct bandgap of 1.43 eV and (d) GaN with a direct bandgap of 3.4 eV. It also shows that a quanta of energy is released with a de-excitation of a carrier.

states at the interface of the two materials; provide relatively higher mobility under applied field therefore, a transistor defined by such a process is referred to as High Electron Mobility Transistor (HEMT). A HEMT when fabricated using high bandgap materials offers dual benefits: (a) to function at high speed; and (b) to maintain its characteristics at high temperature and under high applied electric field [6]. Thus, these devices are preferred to be employed in high power microwave systems and in high temperature environments.

## 1.1 Wide Bandgap Semiconductors

There is no absolute definition by which a wide bandgap semiconductor can be marked. In fact, according to the bandgap theory, semiconductors, in general, are those materials having intermediate bandgaps when compared with conductors ( $E_g = 0$  eV) and insulators ( $E_g \sim 4.50$  eV) [4–6]. The 1<sup>st</sup> generation semiconductors have approximately  $E_g \sim 1$  eV, with this reference, a material having  $E_g \sim 3$  eV or higher can fairly be treated as a wide bandgap material, like GaN and SiC, etc [4–6]. There are four fundamental characteristics, which could be considered while assuring the suitability of semiconductor for a given device need:

1. carriers mobility;
2. breakdown under applied electric field;
3. intrinsic carrier generation rate as a function of temperature and
4. thermal conductivity.

GaN is a material, which can comfortably qualify the criteria listed above.

A basic reason, which made GaN material to be a competitor for such a criteria is its wide bandgap nature. GaN or other 3<sup>rd</sup> generation semiconductors have wide bandgap relative to other semiconductors routinely engaged in microelectronic industry for the device fabrication.

It is pertinent to mention here that wide bandgap based microelectronic technology is not as matured as that of narrow bandgap semiconductor technology. However, wide bandgap devices are catching up with a very fast pace and it is expected that in the near future, the major chunk of high-tech microelectronic industry would be based on wide bandgap devices [2]. This is expected because of the versatility offered by these devices and the improvement noticed in wide bandgap wafer growth.

Devices fabricated using GaN offer high current density, low leakage current and high thermal stability. These properties, inherently possessed by GaN, made it a highly preferred choice for the fabrication of high-speed and high power devices, which can retain their characteristics at elevated temperature and in harsh environments [8]. GaN is used in the industry as a single material to fabricate high power microwave transistors such as GaN Metal Semiconductor Field Effect Transistor (MESFET). Alternatively, GaN can be modulated with another material of similar nature like AlGaIn to achieve Modulation Doped Field Effect Transistor (MODFET), also known as HEMT.

## 1.2 Figure of Merit

There are a number of parameters commonly known as Figure of Merits (FOM), which are used to compare the performance of a semiconductor material for high frequency and high power applications, especially at elevated temperature [9, 10]. Johnson et al. in 1965 [11], defined a criterion called Johnson Figure of Merit (JFOM), which defines the power and high frequency handling capability of a device. The JFOM also takes into account, the critical field,  $E_{cri}$  and the saturation drift velocity,  $v_{sat}$  as per the following equation:

$$\text{JFOM} = \frac{E_{cri}v_{sat}}{2\pi}, \quad (1.1)$$

This expression speaks that as per JFOM any material which would offer relatively high  $E_{cri}$  coupled with relatively high  $v_{sat}$  could be considered a preferred

material for the fabrication of high-tech devices. Reasons that JFOM has considered product  $E_{cri}v_{sat}$  in the numerator of Eq. (1.1) are: that the expression wants to ensure, simultaneously, that the material under consideration has high  $E_{cri}$  to ensure high power applications; whereas, a relative high value of  $v_{sat}$  will allow it to operate at microwave frequencies. So, such a material would be a suitable one for devices intended for microwave power applications.

Similar to JFOM Baliga in 1982, [12] proposed another mechanism to assess figure of merit of materials involved in high-tech device fabrication. It is known as a Baliga Figure of Merit (BFOM) principle. The BFOM involves material parameters to assess the effects of conduction losses caused by the power devices and is given by

$$\text{BFOM} = \varepsilon_s \mu E_g^3 \quad (1.2)$$

In the above equation,  $\mu$  is the mobility of free carriers,  $E_g$  represents the bandgap of the semiconductor under consideration and  $\varepsilon_s$  is its permittivity. Eq. (1.2) uses variable  $E_g$ , which primarily is a reflective of  $E_{cri}$ . A material having a relatively large  $E_g$  will sustain a large applied field; resultantly it will exhibit a large  $E_{cri}$ .

In addition to knowing the thermal performance of a material for high-tech device fabrication, a parameter known as Eliza Quality Factor (EQF) is proposed in [8] and is given by

$$\text{EQF} = \lambda_m \varepsilon_s \mu E_{cri}^3 \quad (1.3)$$

where  $\lambda_m$  represents the thermal conductivity of the material. EQF proposed in Eq. (1.3) is a useful criterion for assessing the quality of a material for high power microwave device fabrication. Its construction is more or less the same as that of Eq. (1.2). Variable  $\lambda_m$  gives an additional information which was not there in Eq. (1.2), and a relatively high value of this variable would mean that the device would be allowing the heat, caused by the intense channel conditions, to dissipate quickly; resultantly, it would maintain its characteristics for longer range of applied voltages and/or at higher ambient temperature.

Table 1.1 shows a comparison of different semiconductors, which are routinely

TABLE 1.1: Comparison of different semiconductor materials properties [8].

Parameter	Unit	Si	GaAs	Diamond	SiC	GaN
Energy bandgap ( $E_g$ )	eV	1.12	1.43	5.45	3.2	3.4
Relative dielectric constant ( $\epsilon_s$ )	-	11.9	12.5	5.5	10.0	9.5
Electron mobility ( $\mu$ )	cm <sup>2</sup> /Vs	1500	8500	2200	700	900
Thermal conductivity	W/Kcm	1.5	0.54	22	4	1.3
Breakdown electric field ( $E_{cri}$ )	MV/cm	0.3	0.4	10000	3.5	3.3
Saturated electron velocity ( $v_{sat}$ )	10 <sup>7</sup> cm/s	1	1	1	2	2.5
Maximum temperature ( $T_{max}$ )	°C	300	300	2100	600	700
BFOM	-	1	9.6	-	3.1	24.6
JFOM	-	1	3.5	-	60	80
EQF	-	1	9.4	198100	90	910

used in microelectronics industry. Data of the table suggest that GaN as a base material would be a relatively better choice for these indices. The data also reflect the suitability of GaN based devices for high frequency and high power applications. Apart from the listed features, another important characteristic is carrier concentration and the detail of which is presented in the next section.

### 1.3 Carrier Concentration vs Temperature

Carrier concentration,  $n_0$  of a semiconductor material, apart from the other parameters, is also dependent upon the temperature and is given by [13]

$$n_0 = \sqrt{N_C N_D} \exp\left(-\frac{E_c - E_d}{2kT}\right) \quad (1.4)$$

$$N_C = 2 \left(\frac{2\pi m_n^* kT}{\hbar^2}\right)^{3/2} \quad (1.5)$$

where  $N_C$  and  $N_D$  represent density of states available in the conduction and donor bands, respectively,  $E_d$  represents donor energy level,  $m_n^*$  effective mass of electron,  $\hbar$  plank constant,  $k$  is the Boltzman constant and  $T$  is the absolute temperature.

Figure 1.2 demonstrates variation of carrier concentration in a semiconductor over a wide range of temperature achieved using Eq. (1.4). It is obvious from the plot

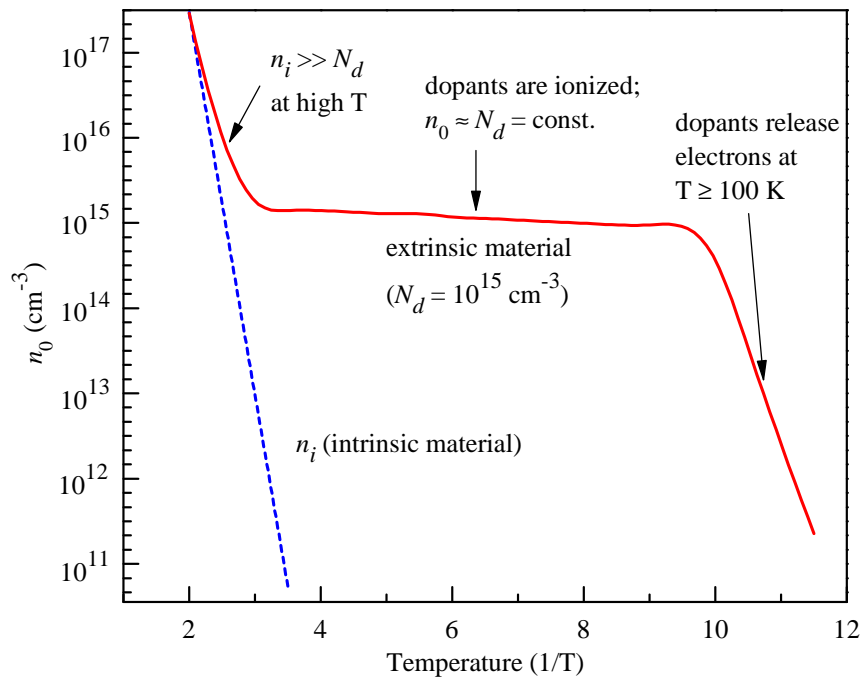


FIGURE 1.2: Variation in intrinsic and extrinsic carriers concentration as a function of temperature.

that the carrier concentration is directly affected by the change in temperature. As the temperature increases (moving towards the origin), the rate of generation of carrier concentration also increases, which is represented by the increasing slope of the red solid line. A point reaches where all donors are ionized and at that temperature  $n_0 \approx N_d$ , where  $N_d$  represents the doping concentration. Then for a reasonable temperature span, this condition persists and that is the span which is known as the safe operating temperature range for a given semiconductor device. A further increase in temperature will initiate electron-hole pair production and this process will continue to an extent that  $n_i > n_0$  as represented by the dotted line in Fig. 1.2. On that very temperature, the characteristics of the device will no more as per its design and it will start generating uncontrolled current due to abundant generation of  $n_i$ , referred to as breakdown of the device.

Figure 1.3 shows variation in  $n_i$  as function of temperature for various semiconductor normally employed in microelectronic industry [7]. Whenever, variation in ambient temperature, the carriers density concentration also varied in the channel.

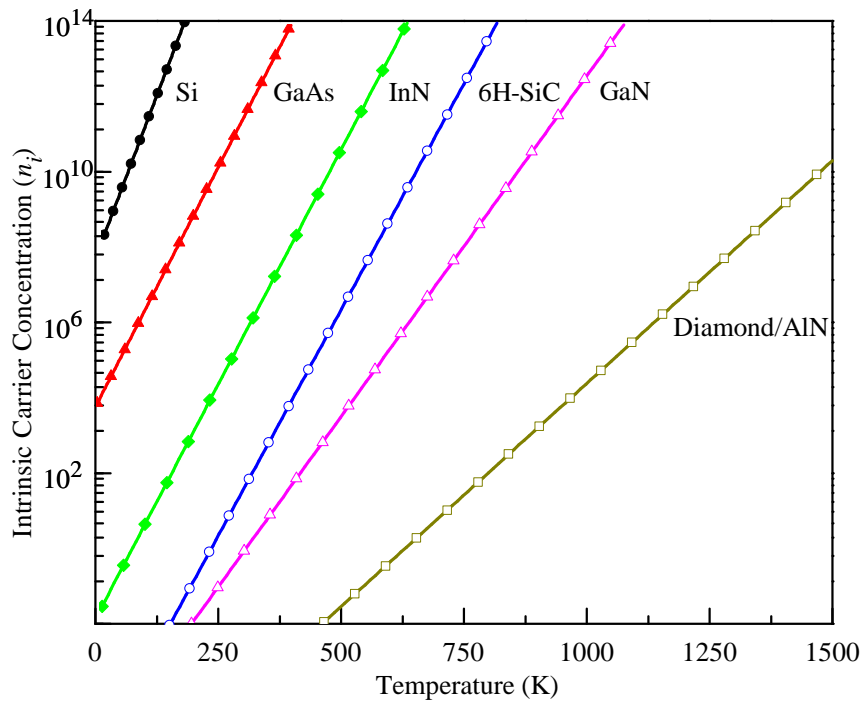


FIGURE 1.3: Intrinsic carrier concentration of different semiconductor materials as a function of temperature [7].

Because carriers generation are directly effected from temperature. Moreover, Figure 1.3 represents a contrast of  $n_i$  generation between narrow and wide bandgap semiconductors. It is evident from the figure, that by increasing temperature Si based devices are very quickly attaining  $1.0 \times 10^{14} \text{cm}^{-3}$  whereas, the same concentration is attained by GaN based devices at a temperature which is 5 times higher than Si. Thus, for high temperature applications GaN would be a preferred choice for device fabrication.

## 1.4 GaN HEMT

In 1993, for the first time, Asif Khan et. al [14] introduced AlGaN/GaN HEMT and its basic structure is shown in Fig. 1.4. A lot of progress has been made afterwards in GaN HEMTs, both from power as well as from high frequency perspective. Keeping in view the current state of technology, one can safely claim



that GaN HEMTs offer exceptionally improved performance compared to AlGaAs/GaAs HEMTs. This improved performance is predominantly associated with the properties associated with GaN semiconductor [15]. In the beginning, GaN HEMTs were fabricated on  $\text{Al}_2\text{O}_3/\text{SiC}$ , but now with the availability of GaN substrates, the quality of epi-layers, defining the channel of the device, improved many folds, which led to further improvement in the device characteristics.

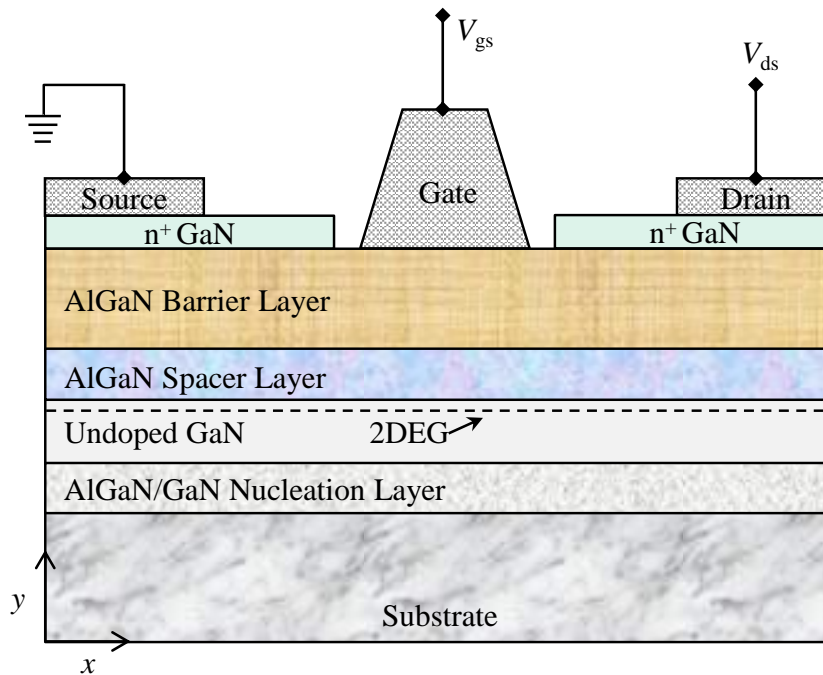


FIGURE 1.4: Detailed layer structure of an AlGaN/GaN HEMT [16].

Figure 1.4 shows an operating GaN HEMT having an undoped AlGaN donor layer covered with a heavily doped GaN contact layer [17, 18]. A heavily doped ( $\sim 10^{18} \text{ cm}^{-3}$ ) contact layer is used to reduce the ohmic contact resistance of the device. Furthermore, keeping GaN as the top layer reduces the risk of aluminum (Al) oxidation available in the 2<sup>nd</sup> layer of the device as shown in Fig. 1.4. A thin sheet of electrons referred to as two dimensional electron gas, 2-DEG is created due to a bandgap mismatch between AlGaN and GaN layers. This creates a quantum-well, wherein carriers are trapped permanently; defining  $n_s$ , which controls current of a HEMT.

Communication with the 2-DEG is made via drain-source ohmic electrodes, which penetrate all the way from the surface to the 2-DEG of the device. The Schottky barrier gate, shown in Fig. 1.4, controls the flow of carriers between drain and source by changing the thickness of 2-DEG. Carriers density, which defines the drain current ( $J_d = qn_s v$ ) is nothing but merely the 2-DEG carrier density, which is normally  $\sim 10^{12} \text{ cm}^{-2}$  [19]. Since carriers are free from their parent atoms and they are trapped in the quantum-well therefore, they experience nominal scattering and as a result, their mobility is considerably higher than the mobility of carriers observed in conventional FETs. To avoid parasitic conductance from the donor layer, it is ensured by the design process that the Schottky barrier depletion at  $V_{gs}=0 \text{ V}$ , should deplete the entire donor layer (AlGaIn), and it should be touching the 2-DEG of the device under built-in conditions. Thus, any change in gate biasing shall have an effect on 2-DEG that in return will change the drain current [19].

Figure 1.5 presents typical  $I - V$  characteristics and output conductance,  $g_d$  of a GaN HEMT. It is obvious from Fig. 1.5(a) that for a given  $V_{gs}$  and with changing  $V_{ds}$ , there is a linear increase in the magnitude of drain current,  $I_{ds}$ , which eventually saturates defining the device saturation current,  $I_{ds(sat)}$ . In GaN HEMTs, saturation is caused by the velocity saturation ( $v_{sat}$ ) of the drifting carriers, and the value of  $v_{sat}$  for GaN based devices is relatively higher as depicted in Table 1.1. This also allows the device to respond at relatively higher frequency. Thus, dependent upon the gate length of the device, it offers higher maximum frequency ( $f_{max}$ ) of operation relative to its counterparts. Figure 1.5(a) also exhibits that with increasing  $V_{gs}$  bias (negatively), there is a voltage referred to as  $V_{th}$ , where  $I_{ds}$  approaches to zero, indicating the pinch-off conditions of the devices. This results into three distinct region of operation: a region where the carriers are drifting below  $v_{sat}$ , commonly known as linear region of operation, a region where carriers have attained  $v_{sat}$  called saturation region of operation and a region where  $I_{ds} \sim 0 \text{ A}$ , referred to as pinch off (threshold) region of operation. Under usual conditions, GaN HEMTs are operated in the saturation region with appropriate bias conditions necessary to avoid distortion.

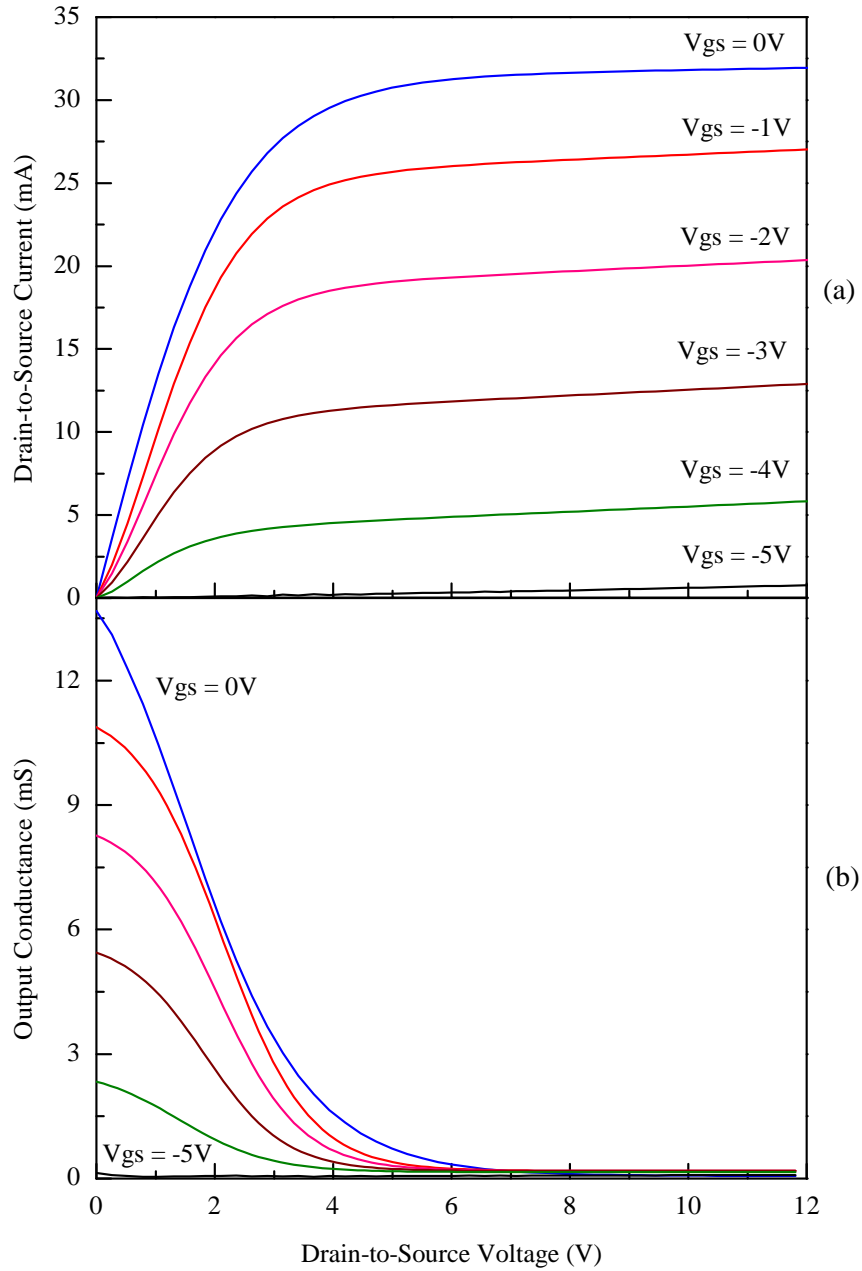


FIGURE 1.5: Typical (a) output  $I - V$  characteristics and (b) output conductance ( $g_d$ ) of a submicron ( $.25 \times 200$ )  $\mu\text{m}^2$  GaN HEMT.

Figure 1.5(b) represents  $g_d$  of a GaN HEMT whose  $I - V$  characteristics are shown in Fig. 1.5(a). The characteristics of Fig. 1.5(b) show variation in  $I_{ds}$  as a function of  $V_{ds}$  for different values of  $V_{gs}$ . It is evident from the figure that the device  $g_d = \partial I_{ds} / \partial V_{ds}$  [20, 21], is sharply declining and then it saturates to a negligible value, which, basically, represents the saturation region where ideally there is no change in  $I_{ds}$  and the device should have  $g_d \sim 0$  mS. The value of  $g_d$

in the saturation region of operation plays a significant role in determining the behavior of the device. GaN HEMT could exhibit negative value of  $g_d$ , after the onset of current saturation, indicative of the fact that the magnitude of  $I_{ds}$  is declining beyond  $V_{ds(sat)}$ . Such an indication leads to the concept of self-heating effect, which could cause a major shift in the device characteristics, and is an important factor to be kept under consideration while designing a high quality GaN HEMT [22].

Figure 1.6 demonstrate Transconductance,  $g_m$  of a HEMT depends upon the input swing of  $V_{gs}$  at a given  $V_{ds}$  and can simply be written as

$$g_m = \left. \frac{\partial I_{ds}}{\partial V_{gs}} \right|_{V_{ds}=\text{constant}} \quad (1.6)$$

Transconductance is one of the important parameter which defines the device performance for microwave application, i.e. high value of  $g_m$  at  $V_{gs}=0$  indicates that the device gain will also be high. Characteristic curves for  $g_m$  and  $I_{ds}$  in response to the variation in  $V_{gs}$  for a GaN HEMT are shown in the Fig. 1.6.

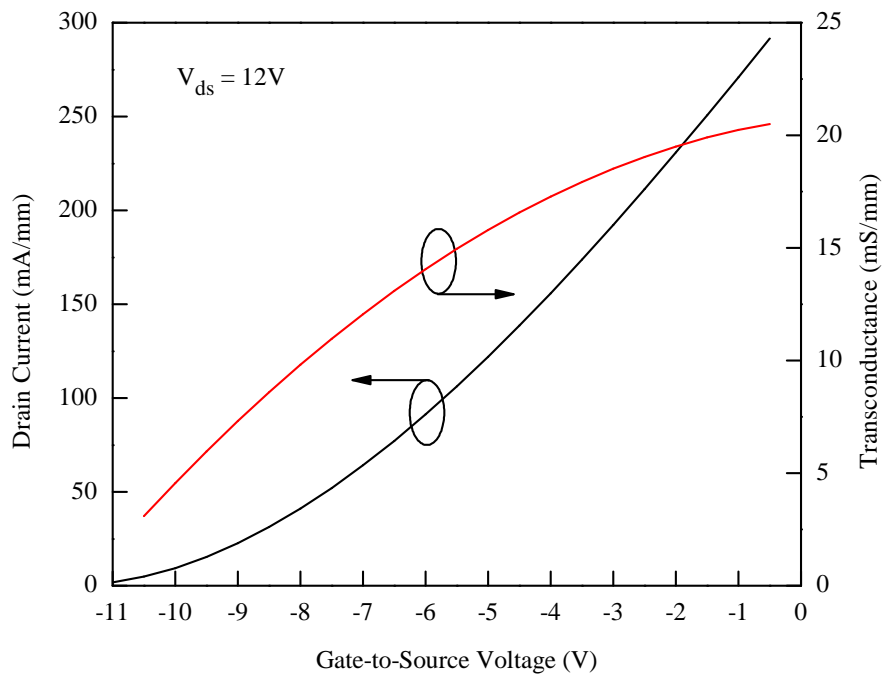


FIGURE 1.6: Typical (a)  $I - V$  characteristics and (b)  $g_m$  of a GaN HEMT as a function of  $V_{gs}$ .

## 1.5 Functional Description of HEMT's Layers

GaN HEMTs operational capabilities can be enhanced by adding the layers to its structure or by modifying the material configuration, or by changing the thicknesses, or doping of the layers affecting the device channel. This could lead to a more refined structure of the device whose fundamental layers are identified in Fig. 1.4. The figure illustrates that the structural arrangement is, usually, composed of: a) substrate, b) nucleation layer, c) channel layer, d) spacer layer, e) barrier or carrier supply, and f) a cap layer. A device could be fabricated either by using all or few of those, dependent upon its target specifications. Subsequent paragraphs of this section will deliberate upon the importance as well as utility of these layers in determining the performance of the device.

### 1.5.1 Substrate

Substrate is a starting and an essential element in HEMT's fabrication, and it has a significant influence on the RF performance of the device. It is also a cost determining factor of a finished HEMT. Its usual thickness is  $\sim 500 \mu\text{m}$ , but its actual thickness is evaluated by knowing the power and the RF requirements for which the device is being designed [17, 23, 24]. Its electrical properties are closer to insulator thus, referred to as semi-insulator. Semi-insulating properties are achieved by adding trapping centers during its growth therefore, it provides a platform for active circuitry to be grown on it without causing any short circuit at the bottom. Substrate ingot are normally grown using one of the bulk growth mechanism, like Bridgman crystal growth technique.

Commonly, three types of substrates are used to support the subsequent layers of the device. They are: SiC, Sapphire ( $\text{Al}_2\text{O}_3$ ) or Si in some cases. SiC offers 3.1%,  $\text{Al}_2\text{O}_3$  13% and Si has 17% mismatch relative to GaN lattice structure [23]. The use of SiC semi-insulating substrate is quite frequent, because of its high thermal conductivity and high resistivity with minimum thermal expansion. Furthermore, it offers low mismatch (only 3.1%) to GaN layers, which are subsequently grown

upon it by using some refined crystal growth technique, like Molecular Beam Epitaxy (MBE) or Metal Organic Chemical Vapor (MOCVD) [25]. A cross-sectional view of a GaN HEMT is shown in Fig. 1.4, indicating the placement of the substrate relative to other layers of the device. At earlier stages, GaN HEMTs had been routinely fabricated using Sapphire/SiC substrates, but currently, due to the advancement in GaN bulk crystal growth, semi-insulating GaN substrate is preferred in high-tech GaN HEMT fabrication.

### 1.5.2 Nucleation Layer

Insertion of this layer, as shown in Fig. 1.4, depends on the material of the substrate and selection of epitaxial growth technique such as MBE or MOCVD. Generally, a thin layer of AlGaN/AlN/GaN is grown to act as seed followed by a thicker GaN channel layer which also acts as a buffer layer. Purpose of the nucleation layer is to reduce stress and lattice mismatch to the non-native substrate and to suppress leakage current, especially, for the cases in which bias is also applied to the substrate [26].

### 1.5.3 Channel Layer

Channel layer is normally grown by MBE or MOCVD technique, such that it should offer minimum and ideally no crystal defects to facilitate improved mobility of 2-DEG carriers. It is an undoped layer, which defines classification of an HEMT. In case of Fig. 1.4, it is of GaN material and the HEMT thus achieved is called as GaN HEMT. A fundamental requirement in HEMT fabrication is the attainment of bandgap discontinuity and the layer under discussion is therefore, of lower bandgap compared to the upper AlGaN layer, as shown in Fig. 1.4. The combination of GaN and AlGaN generates requisite discontinuity, which causes trapping of carriers to generate 2-DEG. Moreover, to achieve improved channel quality, the layer defining the channel of an HEMT should be relatively thicker,  $\sim 20$  nm. Because, after confining the carriers at the interface, the rest of the layer should

serve as an insulator to minimizing trapping effects. Furthermore, it will help to avoid the possibility of drain current collapse under intense operating conditions.

#### 1.5.4 Spacer Layer

In the absence of piezoelectric effect, there is always a need to have a donor layer in HEMT's structure with the purpose that it will release carriers for 2-DEG. This layer will be an optional one for the materials, which exhibits a natural piezoelectric effect; resulting into the release of carriers for 2-DEG. In the presence of such a layer, a spacer layer, as shown in Fig. 1.4, is used to separate hetero-interface from the doped layer whose atoms will become ionized after the release of 2-DEG carriers. The spacer layer will be a thin shielding layer, such that it will behave as a transparent layer for the carriers to move through to reach to the hetero-interface to define 2-DEG, but on the other hand, it will be of sufficient thickness to create a shield between the ionized atoms and the 2-DEG; to minimize scattering that will lead to improved carriers mobility [27]. An optimized thickness of spacer layer is important and critical for HEMT's performance. A thicker layer minimizes ionized scattering caused by the dopant atoms however, channel carrier concentration decreases by increasing the spacer layer thickness. It is therefore a trade-off between the mobility and the carrier concentration. Its bias to either side will be determined by the device application. It is pertinent to mention here that GaN HEMTs can be fabricated without dopant and spacer layers due to piezoelectric effect, which is naturally found in GaN crystals. Due to this very effect, GaN HEMTs are preferred upon their counterparts for microwave power applications.

#### 1.5.5 Barrier layer

As shown in Fig. 1.4, the device Schottky barrier gate is sitting in a recess and the layer which provides Schottky barrier contact has been labeled in the figure as a barrier layer. This is the most important layer in HEMT's construction.

In Fig. 1.4, it is defined by a material having wider bandgap than the channel layer material. It controls the barrier height of the Schottky contact, thus a slight mismatch between Schottky barrier height and the thickness of the layer may generate an undesired parasitic FET; causing a parallel flow of current through the barrier layer. For a good design at  $V_{gs}=0$  V, this layer should be fully depleted, as explained before, and flow of the current should alone be from the 2-DEG. The thickness of the barrier layer is an application dependent decision. A trade-off between less saturated RF power (thinner layer) and small-signal RF gain (thicker layer) is made during the design process. Furthermore, the size and shape of the depletion layer, which is accommodated by the barrier layer is a key controlling variable both for the device AC and DC characteristics. Owing to this fact, barrier layer is referred to as the most important layer in the structure of the device.

Schottky barrier height,  $\phi_b$ , defined collectively by the barrier layer and work function of the Schottky metal will determine whether the device is a depletion mode (D-mode) or an enhancement mode (E-mode) device. This once again puts another constraint on the design of the barrier layer, in order to keep the device operation in the desired mode. Usually, AlGaIn/GaN HEMTs are D-mode transistors but, thinner barrier layer could transform the device as E-mode device. E-mode devices require positive gate potential to open up the channel for finite conduction whilst, D-mode devices, on the other hand, give finite conductance under built-in conditions and require negative gate bias to deplete the channel.

### 1.5.6 Cap or Contact layer

Observing Fig. 1.4 from the top, the first layer before the placement of metal or before the processing of the wafer, which one will encounter is called contact layer. It is a thin heavily doped ( $\sim 10^{18} \text{cm}^{-3}$ ) layer with the purpose to reduce the ohmic contact resistance of the device. There are two ohmic contacts as shown in Fig. 1.4, which facilitate the device communication with the exterior circuitry and their resistance should be as small as possible. To reduce the contacting barrier height so that with the application of exceptionally small potential ( $V_{ds} \sim 0$  V),



the carriers can climb over the barrier, and practically it should sound that there does not exist any barrier; such a condition for the flow of current would be a linear one and the contacts would be referred to as ohmic contacts. High doping in the contact layer improves the linearity of the  $I - V$  characteristics of the device however, because of the degenerate nature of the host semiconductor, there is an upper limit for the doping concentration of the contact layer and its typical value is  $5 \times 10^{18} \text{ cm}^{-3}$  [28–30].

## 1.6 Spontaneous and Piezoelectric Polarization in AlGaN/GaN HEMTs

A unit cell of a GaN crystal is noncentrosymmetric, which generates an unequal distribution of charged atoms. This makes the unit cell a polarized entity and the polarization exhibited by these cells is referred to as spontaneous polarization ( $P_{\text{SP}}$ ). The crystal so achieved is known as a polarized (ferroelectric) crystal, which is used in variety of applications in electronic industry. This natural polarization, which found intently in GaN crystal, can be increased or decreased with the application of internal or external stress. A change in  $P_{\text{SP}}$ , because of the applied stress is called as piezoelectric polarization,  $P_{\text{PE}}$ . If the stress occurs in the direction of  $P_{\text{SP}}$  it adds up and increases its value; whereas, if the direction of applied stress is opposite to that of  $P_{\text{SP}}$  direction, it decreases the magnitude of  $P_{\text{SP}}$  and so does the overall polarization of the crystal [31].

The atomic crystalline structure of GaN material is Wurtzite or hexagonal; where the bilayers contain two closely attached hexagonal films, one of them organized by Ga atoms (Ga face) and the 2<sup>nd</sup> one is formed by N atoms (N face) as shown in Fig. 1.7. These two faces will lead to the generation of covalent bonds between them which are fairly strong and polarized in nature due to non-symmetric distribution of charged atoms. Consequently, producing a strong  $P_{\text{SP}}$  vector as shown in Fig. 1.7. The vector  $P_{\text{SP}}$  is directing downward when observed from Ga-face while its direction is upward when observed from N-face.

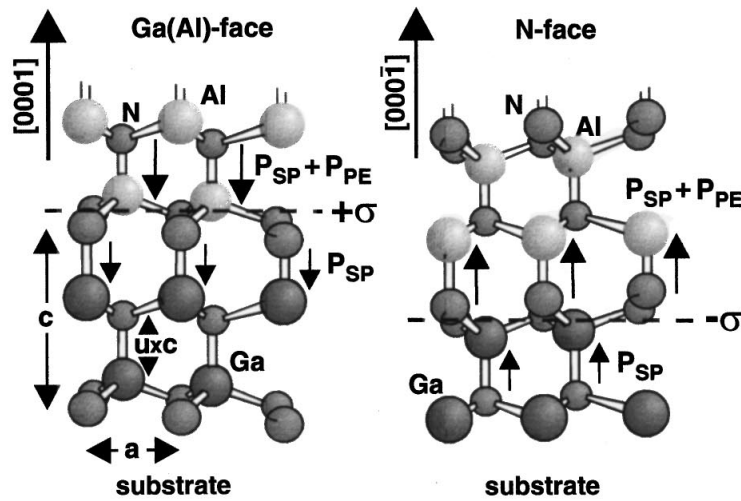


FIGURE 1.7: Atomic layout of Ga-face and N-face of GaN crystal, illustrating the direction and formation of spontaneous polarization, ( $P_{SP}$ ) vectors caused by non-symmetric nature of GaN crystal [32].

When a wide bandgap AlGaN epitaxial layer is grown on a GaN layer, due to both lattice and bandgap mismatch, it produces  $P_{PE}$  strain as discussed in the last paragraph. The direction of  $P_{PE}$  is in line with  $P_{SP}$  for Ga-face and it is opposite for N-face as shown in Fig. 1.8. This further increases non-ideality factor of the crystal lattice. Moreover, it is an established fact that both lattice and bandgap mismatches between AlGaN and GaN layers are dependent on Al mole fraction and, therefore, stress magnitude of an AlGaN/GaN heterostructure can be controlled accordingly. Finally,  $P_{SP}$  and  $P_{PE}$  collectively induces polarization charge density,  $\sigma$  ( $C/cm^2$ ) as given by Eq. (1.7) [31]

$$\sigma = P_{PE, Al_{(1-x)}GaN_{(x)}} + P_{SP, GaN} \quad (1.7)$$

GaN and its associated compounds like AlGaN have very high piezoelectric constants and charges accumulated under the influence of piezoelectric effect can generate field which could measure up to mega volt per centimeter.

Figure 1.9 shows conduction bands of AlGaN/GaN structure, at thermal equilibrium, relative to Fermi level. It clearly shows that at interface the system is at stress because of the mismatch between the energy levels of AlGaN and GaN. This causes accumulation of  $\sigma$  as defined by Eq. (1.7); resultantly electrons inside

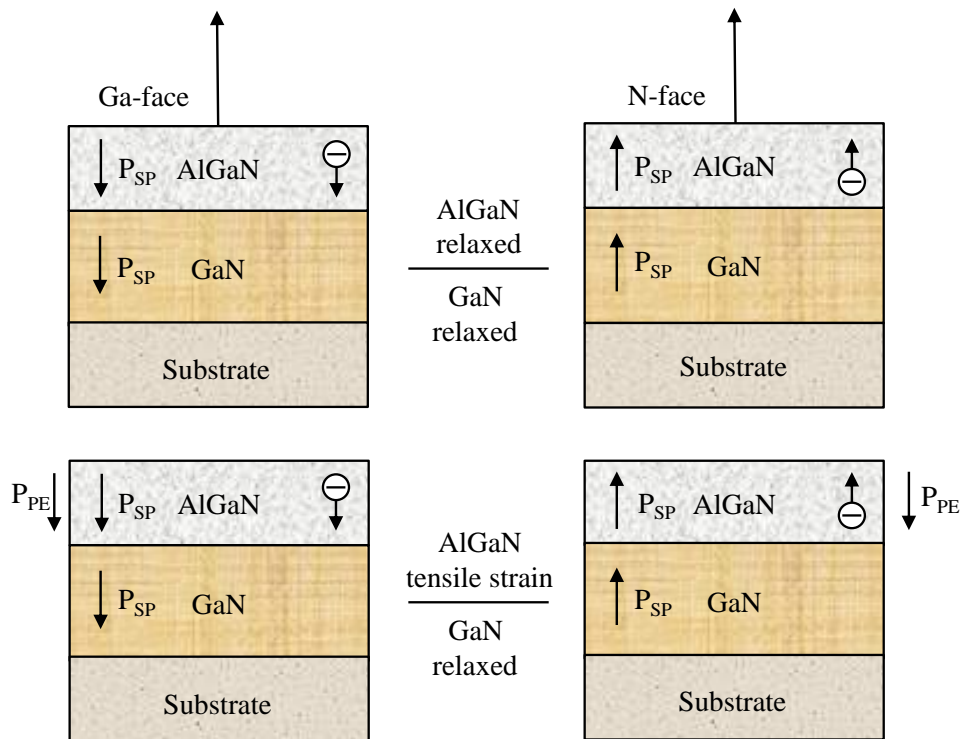


FIGURE 1.8: Pictorial illustration of spontaneous ( $P_{SP}$ ) and piezoelectric polarization ( $P_{PE}$ ) effects present in an AlGaN/GaN HEMT structure.

GaN layer are attracted at the interface as shown in Fig. 1.8 by the band bending towards the Fermi level. Since, there is a discontinuity at the interface defined by  $\Delta E_c$  which will constraint the electrons to stay permanently in that trap defining sheet carrier concentration, i.e. 2-DEG. This explains that contrary to the conventional HEMTs, one can have formation of 2-DEG in AlGaN/GaN HEMT without donor layer, the process therefore is preferred because the numerous benefit associated with it. This is one of the reasons, which made GaN HEMT an exciting candidate of modern power electronic systems.

The process of formation of 2-DEG in AlGaN/GaN HEMT, without donor layer, is also explained in Fig. 1.9. In this figure it is shown that under polarization effects there is accumulation of charges both in AlGaN and GaN layers. At the Interface AlGaN has positive charge accumulation, resultantly GaN layer generates negative charges to balance this effect. These negative charges are nothing but 2-DEG electrons which subsequently define current of the device under applied

external potential [26, 32].

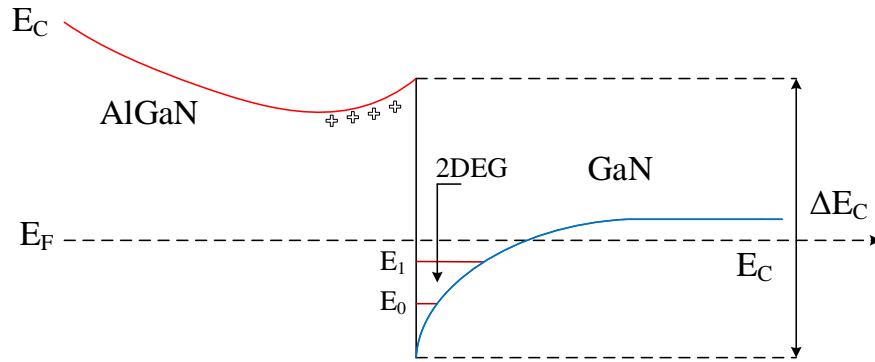


FIGURE 1.9: Difference of conduction band energy levels of AlGaN and GaN materials at thermal equilibrium, which caused formation of bandgap discontinuity,  $\Delta E_c$  when both the materials brought in contact with each other; resulting into generation of 2-DEG.

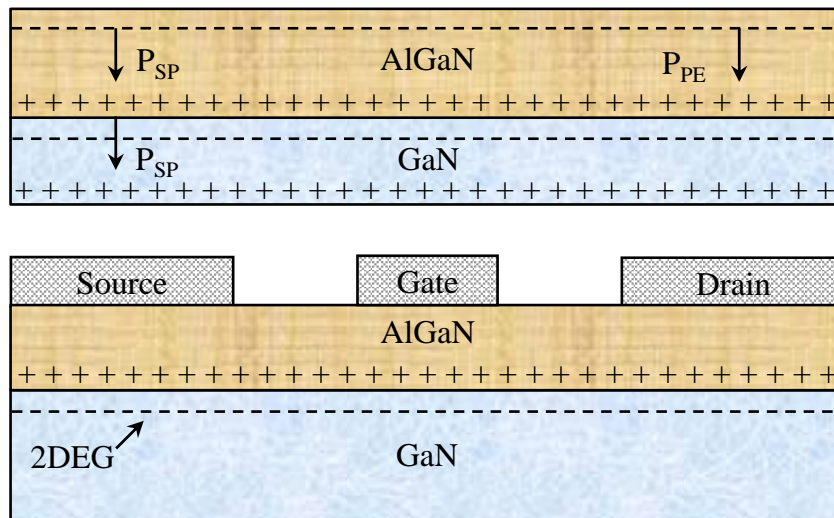


FIGURE 1.10: Epitaxially grown AlGaN/GaN layers showing polarized nature of films. At AlGaN/GaN interface accumulation of electrons in GaN layer get trapped into  $\Delta E_c$  generating 2-DEG.

## 1.7 Temperature Dependent Characteristics

AlGaN/GaN HEMTs are especially designed for hostile environment because of their ability to sustain their characteristics under intense operating conditions. Normally, semiconductor devices exhibit deterioration in their characteristics with

increasing ambient temperature, however, this deterioration is relatively slow in case of AlGa<sub>x</sub>N/GaN HEMTs, which could be associated with two main reasons: first and the foremost is the wide bandgap nature of the material involved in the device channel definition. The second reason is its relatively higher thermal conduction which allows the device to dissipate heat and to mitigate the changes occurring inside the channel under intense operating conditions. AlGa<sub>x</sub>N/GaN HEMTs parameters that could be affected by elevated temperature are enumerated below:

1. conduction band offset,  $\Delta E_c(T)$ ;
2. mobility of the electrons,  $\mu(T)$ ;
3. carriers velocity,  $v_s(T)$ ;
4. Schottky barrier height,  $\phi_b(T)$ ;
5. threshold voltage,  $V_{th}(T)$  and
6. effective width of 2-DEG,  $\Delta d(T)$ .

In aforementioned six variables,  $\Delta E_c$  is a very crucial parameter, which is dependent both on temperature,  $T$  and Al mole fraction,  $m$  in Al<sub>(1-x)</sub>Ga<sub>x</sub>N heterojunction as given below [33, 34]

$$\Delta E_c(T, m) = \gamma \left( E_g^A(T, m) - E_g^G(T, m) \right) \quad (1.8)$$

where  $E_g^A$  and  $E_g^G$  are the bandgaps of AlGa<sub>x</sub>N and GaN, respectively and  $\gamma$  is a constant. For a given  $m$ , if the device is subjected to changed ambient temperature, its characteristics will get affected because of the variation in  $\Delta E_c(T)$ .

Another important temperature dependent variable, which also has a significant role in determining the device characteristics, especially, in hostile environment is  $\mu(T)$ . Variation in the value of  $\mu(T)$  relative to the room temperature value, can be approximated as [35]

$$\mu_T = \mu_{(300K)} \left( \frac{T}{300} \right)^\lambda \quad (1.9)$$

where  $\lambda$  is a fitting variable.

Since  $\Delta E_c(T)$  has got dependence on  $T$ , likewise the variable  $\mu(T)$  also depends upon  $T$  as shown in Eqs. (1.8) and (1.9), respectively, in such a way that the first one has an impact on 2-DEG of the device; whereas, the second one is associated with the velocity of carriers as  $v(T) = \mu(T)E$ , where  $E$  is the applied electric field. This indicates that the device current, both in the linear as well as in the saturation region of operation will be affected at elevated temperature. Fig. 1.11 represents experimental  $I - V$  characteristics of a submicron AlGaIn/GaN HEMT measured at various temperatures. This figure clearly shows that by increasing ambient temperature, there is a change in the device physical parameters, which results into a reduction in the drain current both in the linear as well as in the saturation region of operation. Reasons associated with this change along with a plausible explanation of  $\Delta E_c(T)$  and  $\mu(T)$ , shall be discussed in later parts of this thesis.

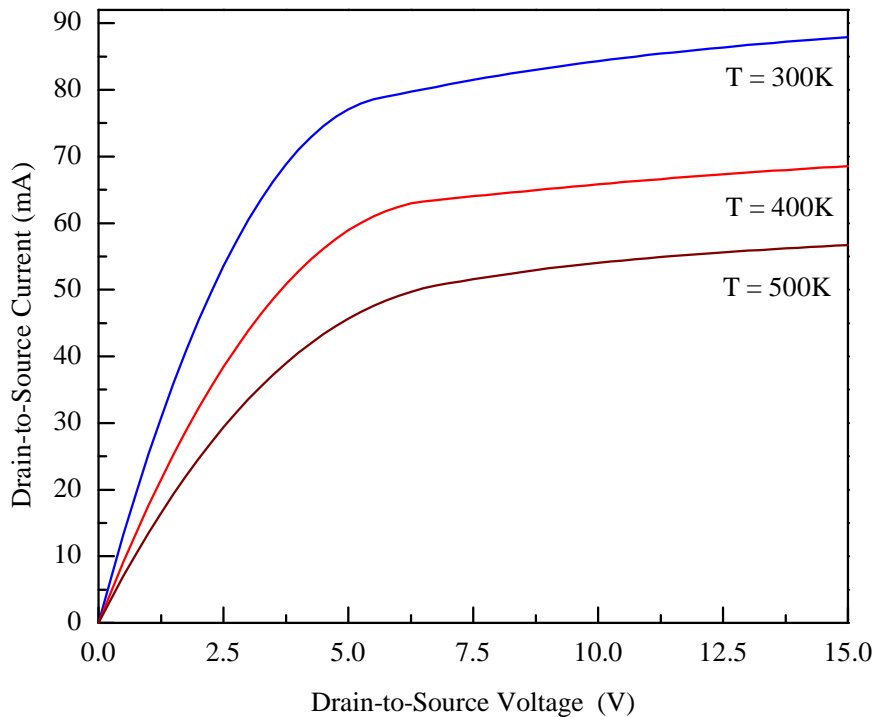


FIGURE 1.11: Experimental current-voltage characteristics at  $V_{gs} = 0V$  of a submicron AlGaIn/GaN HEMT at various temperatures.

High frequency performance of the device is controlled primarily by the Miller capacitors i.e. gate-to-source capacitor,  $C_{gs}$  and gate-to-drain capacitor,  $C_{gd}$ . Since

both of these capacitors are associated with the  $\phi_b(T)$ , therefore any variation in  $\phi_b(T)$  because of the ambient conditions will have a direct impact on the AC performance of the device. So, in general, it could be said that both AC and DC characteristics of the device are affected by the ambient conditions and a detailed study in this respect shall be a beneficial one in order to exploit the fullest potential of the device for high frequency and high power applications.

## 1.8 RF Performance of AlGaIn/GaN HEMTs

AlGaIn/GaN HEMT's architecture and material properties permit operation of the device at relatively high frequency and hostile operating conditions. When an RF signal is applied at Schottky barrier gate, it causes an alteration in the channel current; resulting into channel current modulation. Thus, translating the gate information into an amplified signal available through drain-source electrodes. RF signal reaching at the gate electrode is coupled with the channel via  $C_{gs}$  and  $C_{gd}$  capacitors therefore, both of these capacitors play a crucial role in determine the RF performance of an AlGaIn/GaN HEMT. A relatively high value of these capacitors would necessitate a longer charging-discharging process and such devices would naturally be slow in term of their RF response. A straight forward mechanism to improve the RF response of the device is the reduction in  $L_g$ . A reduced value of  $L_g$  will have lower crosssectional area, responsible to define  $C_{gs}$  and  $C_{gd}$ ; resulting into improved RF performance. Dependence of unity gain frequency,  $f_T$  of a GaN HEMT on the device physical parameters are given as [36]

$$f_T = \frac{g_m}{2\pi(C_{gs} + C_{gd})} = \frac{v_{(sat)}}{2\pi L_g} \quad (1.10)$$

where  $g_m$  is the transconductance of the device, which is basically a measure of Schottky barrier quality. In the absence of interface states, the quality of a Schottky barrier is high, which eventually is translated into a high  $g_m$ . As per Eq. (1.10) such devices will also have a relatively high magnitude of  $f_T$ .

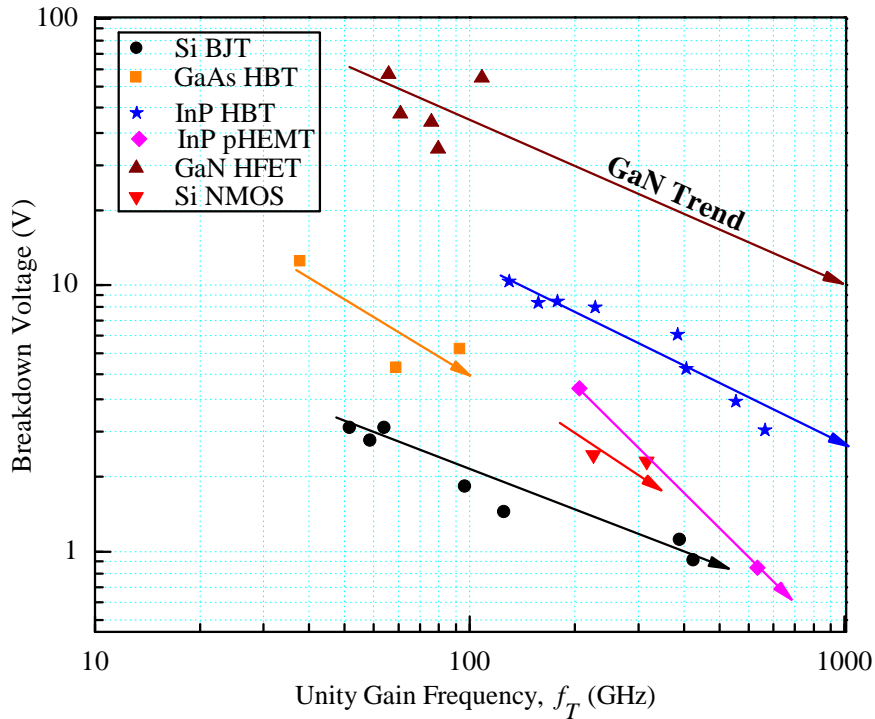


FIGURE 1.12: Breakdown voltage ( $V_{Br}$ ) vs unity gain frequency ( $f_T$ ) trend of various types of transistors commonly used in power electronics [37].

Reduction in  $L_g$ , on one hand, improves the RF performance of the device but, on the other hand, it increases the channel electric field underneath the Schottky barrier gate, which could cause an earlier breakdown of the HEMT [38]. It is therefore, a trade-off between  $f_T$  and  $V_{Br}$ . Figure 1.12 presents a projection of various transistors technologies, wherein  $V_{Br}$  is plotted as a function of  $f_T$ . It is obvious from the figure that keeping in view the possible growth in GaN HEMT technology, which is evident from the recent past, it is very likely that GaN HEMT will outperform other transistors, normally engaged in microwave power applications.

## 1.9 Summary and Thesis Outline

This chapter basically presents fundamentals of AlGaN/GaN HEMTs, its physical structure and electrical characteristics. It is discussed that AlGaN/GaN HEMT has strong potential as a microwave power device and it offers very promising characteristics both at high frequency and power. It is discussed that the device



can work with an acceptable performance in an hostile environment where usually other devices fail to retain their characteristics. A warm feeling about the future prospects of the device is created through the discussion of this chapter with the aim that better understanding about the device behavior, especially in an hostile environment will help in its growth. The remaining parts of this thesis are organized as follows:–

**Chapter two** discusses the 3<sup>rd</sup> generation wide bandgap semiconductors (SiC, GaN) and their potential use in microelectronic industry. For high power and harsh environment applications, characteristics offered by narrow bandgap semiconductors (Si, GaAs) are insufficient and one has to opt for wide bandgap semiconductors. GaN as a wide bandgap semiconductor offers excellent characteristics and can therefore be employed in device fabrication, especially in high-tech devices such as HEMTs. At high power and in harsh environment, deterioration in a semiconductor device characteristics is a natural phenomenon and the same has been dually emphasized in this chapter. However, it is also discussed that GaN HEMTs have higher resilience to these changes, because of high thermal conductivity and wide bandgap nature of the device material.

**Chapter three** presets an analytical model to predict the temperature dependent DC characteristics of AlGaN/GaN HEMTs. The proposed model incorporates the temperature-dependent variation in the Schottky barrier height, bandgap discontinuity, sheet carrier concentration of 2-DEG, saturation velocity and carrier mobility. The degradation in the  $I - V$  characteristics of AlGaN/GaN HEMTs at elevated temperature is accurately modeled for improved understanding. The proposed model is compared with other reported models intended for prediction of temperature-dependent  $I - V$  characteristics; the RMSE values indicate that the proposed model can simulate the temperature-dependent  $I - V$  characteristics with improved accuracy.

**Chapter four** gives a modified model for submicron AlGaN/GaN HEMTs to evaluate temperature dependent AC characteristics. Validity of the proposed technique is established using experimental data for the temperature ranging from 233

K to 423 K. Device intrinsic small signal parameters are evaluated and by employing assessed small signal parameters, S-parameters of the device are calculated and their comparison with the measured data is made to establish the validity of the proposed technique.

**Chapter five** presents a non-linear single expression model of AlGa<sub>N</sub>/Ga<sub>N</sub> HEMTs  $I - V$  for computer aided design (CAD) software. The model takes into account dependence of output conductance on the device drain and gate bias and simulates both positive and negative conductance to a good degree of accuracy. Appearance of peak transconductance to a relatively higher negative gate bias is a routinely observed phenomenon in Ga<sub>N</sub> HEMTs, and the proposed model has the ability to simulate such characteristics with improved accuracy. To check the validity of the proposed model, a comparative study is carried out by selected devices of varying lengths and widths. The accuracy of the model is also checked at elevated temperature i.e. up to 773 K and was found significantly better than its counterparts. As, the proposed model is based on a single expression, it is therefore easy to handle with and can comfortably be used in Computer Aided Design (CAD) software to assess the temperature dependent performance of Ga<sub>N</sub> HEMTs for their possible integration into power circuitries.

**Chapter six** describes conclusions drawn from this research and it also proposes an extension to this research work by identifying various aspects, which are out of the scope of this thesis and left for the future research.

# Chapter 2

## Literature Review

### 2.1 Introduction

Devices fabricated using wide bandgap semiconductors can sustain operation at elevated temperatures, high bias, and have the capability to handle high power density in fast switching processes. On the other hand, devices fabricated using Si, GaAs, Indium Phosphide (InP), etc. deteriorate their performance for such operations primarily due to their narrower bandgap materials.

GaN-based devices, precisely AlGaN/GaN HEMTs have bandgap  $\sim 3.4$  eV and thus, are favorable for operation at elevated temperatures reaching up to 500 °C [39]. In addition, high charge carrier concentration,  $n_s$  in 2-DEG combined with high mobility results in low on resistance,  $R_{on} < 100$  m $\Omega$  for a 20 A device [40]. As switching losses in semiconductor devices depend upon the product of  $R_{on}$  and the total charge accumulated underneath the Schottky barrier gate,  $Q_g$  thus, for AlGaN/GaN HEMTs,  $R_{on} \times Q_g < 1$  nC $\Omega$ ; resulting in minimum switching loss, which in turn translates into high power conversion in switching mode [41]. Furthermore, high breakdown field of GaN  $\approx 3.3$  MV/cm supports high bias operations; a basic need of a power transistor. The performance trend of GaN-based HEMTs is shown in Fig. 1.12. The data of the figure clearly show that GaN HEMTs have the potential to be used for microwave power applications.

GaN based devices are now being commercialized in various photonic areas, however, the semiconductor is still in its first phase of commercialization due to the absence of compatible GaN substrates. Currently, GaN epilayers are mostly fabricated on foreign substrates, such as SiC, sapphire and Si. GaN epitaxial layer grown on Si substrates offers a cost effective solution in cases where large dia substrates are grown (up to 200 mm). For high power and robust operations, SiC is used as a substrate instead of Si due to its relatively higher thermal conductivity [2].

## 2.2 Wide Bandgap Semiconductors

In the last few decades, a real break through in the field of power electronics and communication systems has been witnessed [42], primarily due to the discovery of wide bandgap semiconductors such as AlGaN, SiC, GaN, etc. A semiconductor material that has a bandgap of more than 2.2 eV is commonly categorized as a wide bandgap semiconductor, and is also called a 3<sup>rd</sup> generation semiconductor. Recently, a shift in the semiconductor device fabrication is observed wherein, a large number of devices are being fabricated using wide bandgap materials due to their superior material properties when compared with narrow bandgap semiconductors. Wide bandgap materials not only offer enhanced device performance in harsh environments but also have numerous other possibilities in electronic circuits that cannot be realized using narrow bandgap materials. Following paragraphs discuss in detail advantages associated with wide bandgap semiconductors, supported by the relevant literature and the summary of the same is presented in Table 2.1.

Tolbert et al. [43] studied the future technological capabilities of wide bandgap materials suited for high power applications and in harsh environments. Their aim was to investigate the applicabilities of wide bandgap devices for a broad spectrum of power applications. They reported that wide bandgap semiconductors can be utilized in unfavorable environmental conditions and the devices made from them

are capable to handle high power loads. For comparative analysis, they studied typical semiconductor materials such as Si, SiC, GaN and diamond. They observed that diamond is the most suitable material for harsh environments, but hard to process in the industry. GaN and SiC based devices can handle power with much higher efficiency than Si based devices. Moreover, while comparing GaN and SiC, they found that GaN outperformed SiC devices especially, in power related applications.

Millan et al. [44] reported the importance of wide bandgap semiconductor materials for the next generation power devices (high power converters) with contrast to the conventionally made narrow bandgap semiconductor devices. They observed that existing narrow bandgap semiconductor devices have relatively lower breakdown voltage compared to wide bandgap devices. As an example, conventional Si based IGBT break downs at 6.5 kV while wide bandgap based Insulated Gate Bipolar Transistor (IGBT) can hold up to 10 kV. Further, Si based devices fail under extreme temperatures and cannot maintain their performance over 200 °C. They further reported that these unavoidable physical limitations reduce the efficiency and performance of existing high power converters. To enhance the operation of such conventional devices beyond their maximum limit, a complicated and costly cooling system is required, which increases the overall size and cost of the system. In addition, they reported that by using wide bandgap semiconductors, the overall efficiency of electrical conversion systems can be enhanced. Hostetler et al. [45] expressed that wide bandgap materials play a critical role in electrical energy conversion. They reported that wide bandgap switches have improved the performance of motor drive systems up to 30% when compared with conventional Si-IGBT switches.

Iacopi et al. in 2015 [46] reported that use of wide bandgap semiconductors reduces the overall size of an electronic system. Besides that, it lowers the energy consumption of the systems compared to narrow bangap devices. Moreover, their study also revealed that a wide bandgap system offers faster switching speed, smaller size, efficient power conversion and has the ability to operate at considerably high temperature. Li et al. in 2016 [47] examined and compared the conduction and

TABLE 2.1: A brief overview of wide bandgap devices.

Year	Author	Description	Ref.
2003	Tolbert et al.	Power handling capability of wide bandgap devices	[43]
2012	Millan et al.	High power conversion of wide bandgap devices	[44]
2014	Hostetler et al.	Wide bandgap semiconductor motor switches	[45]
2015	Iacopi et al.	High power, voltage and temperature applications of wide bandgap devices	[46]
2016	Li et al.	Conduction and switching performance of wide bandgap based devices	[47]

switching losses of wide bandgap SiC and GaN semiconductor devices of the same power rating, both experimentally and theoretically. In their work, they observed that  $R_{on}$  of SiC reduces to half of its original value when the applied voltage is also half of the maximum blocking voltage. In this state, gate to drain charge,  $Q_{gd}$  increases but the same rated GaN base device showed five times decrease in  $Q_{gd}$ . They also observed that a GaN based transistor offers relatively lower  $R_{on}$  compared to a SiC transistor under identical bias conditions. Thus GaN, as a wide bandgap material, for the fabrication of power devices will have preference upon SiC.

## 2.3 GaN Based Technology

GaN-based technology started in the early 20<sup>th</sup> century. Johnson et al. [48] fabricated GaN, for the first time, by passing ammonia gas ( $\text{NH}_3$ ) on metallic gallium, Ga, at a very high temperature, i.e. 1000 °C. In 1938, Juza et al. [49] also fabricated GaN using similar procedure, i.e. passing  $\text{NH}_3$  over Ga at elevated temperatures, but they used liquid Ga instead of metallic. They also explored the crystalline structure and lattice constant of GaN. In 1969, Maruska et al. [50] grew GaN epitaxial layers on sapphire substrates. They prepared a single colorless crystalline structure of GaN by vapor-phase growth technique, and also determined direct energy bandgap of Ga and found it to be  $\sim 3.39$  eV.

After the discovery of GaN, the next milestone was achieved by Asif et al. in 1991 [51], when for the first time they demonstrated the existence of 2-DEG due to bandgap discontinuity at the heterojunction of AlGa<sub>N</sub>/Ga<sub>N</sub> semiconductor material. The heterostructure was formulated on a sapphire substrate by MOCVD. The rapid growth of GaN technology continued, and for the first time in 1993, MESFET was grown on a sapphire substrate also by MOCVD technique and in the following year, HEMT was grown through a similar procedure by Asif et al. [14, 52]. During the same time, Bykhovski et al. [53] discussed the presence of piezoelectric properties at the interface of Ga<sub>N</sub>/AlN/GaN. They stated that these properties will play a key role in defining the electrical characteristics of the material and their associated heterostructure devices.

Ozgun et al. in 1995 [54] fabricated a normally off GaN-based MODFET with a relatively high transconductance ( $g_m$ ). Asbeck et al. [55] studied the impact of piezoelectric effects on the design and performance of III-V group AlGa<sub>N</sub>/Ga<sub>N</sub> HEMTs. They grew the devices by MOCVD and MBE techniques on SiC and sapphire substrates, respectively. Ren et al. in 1998 [56] reported a new methodology, to reduce the gate leakage current and parasitic effects, to improve the device performance at elevated temperatures by depositing Ga<sub>2</sub>O<sub>3</sub>(Gd<sub>3</sub>O<sub>3</sub>) layer on Ga<sub>N</sub> surface.

Wu et al. [57] studied the importance of Al content on the barrier layer of AlGa<sub>N</sub>/Ga<sub>N</sub>. They reported that increase of Al mole composition will raise the overall performance of AlGa<sub>N</sub>/Ga<sub>N</sub> MODFET. They also reported many advantages of Al content in MODFET such as, an increase in carrier mobility due to increase in bandgap discontinuity at heterojunction interface. Additionally, they demonstrated that due to piezoelectric effects, both high electron velocity and high breakdown voltage are achieved by the MODFET. Ambacher et al. [31] investigated the effects of Al mole concentration on  $n_s$  of 2-DEG. They observed that an increase in Al mole composition increases  $n_s$  of the device. Further, effects of Al on saturation velocity and carrier mobility were also investigated by them.

In 1999, Yoshida et al. [58] fabricated GaN based MESFET and NPN Bipolar Junction Transistor (BJT) by using Gas Source Molecular Beam Epitaxy (GSMBE). They examined the performance of the fabricated devices at 300 °C and 400 °C continuously for 3 and 4 hours, respectively. They reported that no degradation was observed in the metal-semiconductor interface. Zhang et al. in 2000 [59] fabricated PNP transistors using AlGa<sub>N</sub>/Ga<sub>N</sub> and measured their DC characteristics in common base and collector modes up to 250 °C. They observed that in both modes, the current was almost identical to the emitter current under all circumstances. Semond et al. in 2001 [60] fabricated AlGa<sub>N</sub>/Ga<sub>N</sub> heterostructures on Si(111) substrate by employing MBE and demonstrated the potential use of Si as a substrate material for AlGa<sub>N</sub>/Ga<sub>N</sub> devices.

In 2006, Cai et al. [61] reported that AlGa<sub>N</sub>/Ga<sub>N</sub> devices are sensitive to fabrication techniques. They fabricated devices by employing fluoride based plasma treatment and found a shift in threshold voltage,  $V_{th}$  both in conventional depletion mode as well as in enhancement modes AlGa<sub>N</sub>/Ga<sub>N</sub> HEMTs. Uemoto et al. in 2007 [62] developed a novel device, which they called gate injection transistor. The device's basic principle operation was the injection of hole from *p*-AlGa<sub>N</sub> layer into the heterojunction interface of AlGa<sub>N</sub>/Ga<sub>N</sub> layer. The injection of holes increased the value of  $n_s$  in 2-DEG; resultantly increased the drain current of the channel.

Tripathy et al. in 2012 [63] reported epitaxial growth of crack free AlGa<sub>N</sub>/Ga<sub>N</sub> heterostructures on Si(111) substrates through MOCVD technique. They also characterized the fabricated devices and found enhanced electrical performance. In 2013, Zhang et al. [64] fabricated a dual-gate structure E-mode MOS-HEMT and demonstrated that the device can operate stably up to 250 °C and have  $V_{th}$  greater than 3 V. In general, one can say that there is a phenomenal growth both in Ga<sub>N</sub> based heterojunction materials as well as in AlGa<sub>N</sub>/Ga<sub>N</sub> heterostructure devices. Therefore, Ga<sub>N</sub> can rightly be treated as 3<sup>rd</sup> generation semiconductor. A summary indicating various stages of growth in Ga<sub>N</sub> technology is presented in Table 2.2.



TABLE 2.2: A brief overview of GaN based technology.

Year	Author	Description	Ref.
1932	Johanson et al.	GaN fabrication through metallic Ga	[48]
1938	Juza et al.	GaN fabrication through liquid Ga	[49]
1969	Maruska et al.	GaN epitaxial growth	[50]
1991	Asif et al.	Enhanced mobility observation	[51]
1993	Asif et al.	GaN based MESFET fabrication	[52]
1993	Bykhovski et al.	Existence of piezoelectric effect	[53]
1994	Asif et al.	GaN based HEMT fabrication	[14]
1995	Ozgur et al.	Fabrication of high $g_m$ MODFET	[54]
1997	Asbeck et al.	Influence of piezoelectric on the device performance	[55]
1998	Ren et al.	Reduction in gate leakage and parasitic effects	[56]
1998	Wu et al.	Al-content in barrier layer of AlGaIn/GaN	[57]
1999	Ambacher et al.	Concentration of $n_s$ in 2GEG	[31]
1999	Yoshida et al.	Fabrication of NPN BJT	[58]
2000	Zhang et al.	Fabrication of PNP BJT	[59]
2001	Semond et al.	AlGaIn/GaN on Si(111) substrate	[60]
2006	Cai et al.	Fluoride-based plasma treatment	[61]
2007	Uemoto et al.	Development of GIT novel device	[62]
2012	Tripathy et al.	Crack free heterostructures	[63]
2013	Zhang et al.	Dual-gate E-mode MOS-HEMTs	[64]

## 2.4 GaN HEMTs RF High Power Performance

GaN based HEMTs are routinely used in RF high power amplifiers. At high bias voltages, the degradation in the device saturation velocity and mobility is nominal; making the device suitable for high power RF applications.

In 2003, Boutros et al. [65] fabricated GaN-based HEMTs of gate width,  $W = 100 \mu\text{m}$  and gate length,  $L_g$  of  $0.18 \mu\text{m}$ . Their devices epitaxial layers structure consisted of AlGaIn/GaN grown on a semi insulating 4H-SiC substrate. Fabricated

TABLE 2.3: RF power performance of GaN-based HEMTs.

$L_g$ ( $\mu\text{m}$ )	$P_{out}$ (W/mm)	$f_T$ (GHz)	$f_{max}$ (GHz)	Ref.
0.18	3.40	84	130	[65]
1.30	4.50	13.7	–	[66]
0.35	10.08	20	34.2	[67]
0.16	10.50	>40	>40	[68]
0.10	2.10	95	110	[69]
0.25	3.79	11.8	27.5	[70]
0.10	–	81	138	[71]

devices exhibited maximum frequency,  $f_{max} = 130$  GHz and unity current gain,  $f_T = 84$  GHz. The devices could operate at a maximum power,  $P_{max}$  of 2.8 W/mm at  $V_{ds} = 30$  V. At operational frequency of 238 GHz and at same bias and ambient conditions,  $P_{max}$  showed a considerable increase in its magnitude, i.e.  $P_{max} = 3.4$  W/mm.

Mitsutoshi et al. [66] performed temperature dependent  $f_T$  measurements of AlGaIn/GaN HEMTs of  $L_g = 1.3 \mu\text{m}$ . They reported that  $f_T$  decreases monotonically with the increases of temperature. Furthermore, they showed that the device  $f_T$  reduced from 13.7 GHz to 8.7 GHz when temperature is changed from 23°C to 187 °C.

Nuttinck et al. in 2003 [67] studied the behavior of high power AlGaIn/GaN HEMTs having dimensions  $0.35 \times 250 \mu\text{m}^2$  as a function of frequency and temperature. They reported minimum noise figure,  $NF_{min} = 2.6$  dB and gain,  $G = 15$  dB at 3 GHz while maintaining temperature at 540 K. They also studied temperature dependent power performance of the device. With the increase in temperature, a decrease in the output power was reported. At  $f = 4$  GHz, by changing the temperature from 295 K to 540 K, the output power decreased from 33 dBm to 28 dBm, respectively.

Palacios et al. in 2005 [68] fabricated two different types of AlGaIn/GaN HEMTs for high frequency applications. Both the devices had similar dimensions, i.e.

$0.16 \times 2 \times 75 \mu\text{m}^2$  but had different fabrication technologies. The first device was grown by MOCVD process and the second device was fabricated using MBE process. They reported  $P_{out} = 10.5 \text{ W/mm}$  and power added efficiency, PAE = 33% at 40 GHz for MOCVD device and for the MBE device,  $P_{out} = 8.6 \text{ W/mm}$  and PAE = 29% at 40 GHz was observed. Micovic et al. [69] fabricated GaN-based HEMTs for continuous W-band wave length. They observed  $P_{out} = 2.1 \text{ W/m}$  with power gain of 17.5 dB at 80.5 GHz frequency.

Arulkumaran et al. [70] investigated the effects of temperature on the output power performance of AlGaIn/GaN HEMTs, fabricated on high resistivity Si substrate. They carried out experimentation at different frequencies, i.e. 3, 6 and 8 GHz. In their results, they observed a decrease in  $P_{out} = 3.79 \text{ mW/}^\circ\text{C mm}$ ,  $4.33 \text{ mW/}^\circ\text{C mm}$  and  $4.27 \text{ mW/}^\circ\text{C mm}$  at frequencies 3, 6 and 8 GHz, respectively; with the increase in temperature. Moreover, at  $T = 200 \text{ }^\circ\text{C}$ , they observed  $P_{out} = 1.16 \text{ W/mm}$ , PAE = 22.8% and associated  $G = 7.52 \text{ dB}$  at 3 GHz. Furthermore, due to lower thermal conductivity of Si compared to SiC, more  $P_{out}$  loss was observed when Si substrate was employed instead of SiC.

Chunlei et al. [71] fabricated GaN-based HEMTs having dimensions  $0.1 \times 80 \mu\text{m}^2$ . A special oxygen plasma treatment was used before the gate metal evaporation to minimize the gate leakage current. In the fabrication process, they also used SiN passivation layer and Si/Ti/Al/Ni/Au ohmic contacts to improve RF, DC characteristics and also to improve reliability of ohmic contacts. They reported  $f_T = 81 \text{ GHz}$  and  $f_{max} = 138 \text{ GHz}$  for their fabricated devices. The observed improved performance could naturally be associated with improved Schottky and ohmic characteristics.

Table 2.3 gives a comprehensive history of RF performance of GaN based HEMTs. In general, it could be said that by keeping other variables constant and reducing the  $L_g$  of the device, there is an increase in  $f_T$  and accordingly in  $f_{max}$ . It is also evident from the table that in current GaN HEMT technology,  $L_g$  is approaching one tenth of a micron thus, any further reduction might not increase  $f_T$  and  $f_{max}$  because of the reduction in  $g_m$ .

TABLE 2.4: Effects of self-heating on the performance of GaN-based HEMTs.

Year	Author	Self-heating effect on the device performance	Ref.
1998	Gaska et al.	Comparative analysis	[72]
2006	Ahmad et al.	Measured temperature dispersion profile	[73]
2006	Wu et al.	Self-heating effect on various DC parameters	[74]
2008	Chattopadhyay et al.	Channel temperature	[22]
2009	Hosch et al.	High power performance	[75]

## 2.5 Self-Heating Effects

Several methodologies have been considered to examine the consequences of self-heating effects on the device performance, which mainly happen due to the collisional energy loss from electrons. The energy loss consequently reduces the device power and it also effects the high frequency operation of the device due to Miller capacitors modification [23].

Gaska et al. [72] reported comparative analysis of self-heating phenomenon in AlGa<sub>N</sub>/Ga<sub>N</sub> HEMTs. They fabricated AlGa<sub>N</sub>/Ga<sub>N</sub> HEMTs on 6H-SiC and sapphire substrates and investigated experimentally the self-heating kinetics and heat-times characteristics. They reported that AlGa<sub>N</sub>/Ga<sub>N</sub> HEMTs on SiC substrate afford better electron transport mechanism and excellent thermal properties compared to sapphire substrate. Ahmad et al. [73] used UV-Raman spectroscopy to measure the temperature dispersion profile in AlGa<sub>N</sub>/Ga<sub>N</sub> HEMTs for different range of bias voltages. They performed measurements using micro-Raman scattering process, wherein they excited the device above and below its bandgap through ultraviolet and visible laser lights, respectively.

Wu et al. [74] observed the influence of self-heating on various parameters of HEMTs such as current, power and associated components. They also observed temperature profile of the device under pulsed and DC bias conditions. They reported that self-heating effects can not be ignored and they are important even

for short pulses, as hot phonons or non-equilibrium phonons might create current suppression. Chattopadhyay et al. [22] presented a physics based analytical model by developing a relationship between self-heating and the device physical parameters by involving 2-DEG channel current. Hosch et al. [75] examined negative effects of self-heating on the performance of AlGaIn/GaN HEMTs. They obtained the results through Micro-Raman thermography at various power and voltage levels. They investigated the influence of  $V_{ds}$  on temperature distribution of the device when the dissipated power was kept constant by applying a constant  $V_{gs}$ . They further investigated self-heating by employing numerical electro-thermal simulations of the device and showed device performance deterioration under the influence of self-heating. A summary of self-heating related investigation is presented in Table 2.4. The data of the table and the discussion presented explained the importance of self-heating phenomenon in determining the characteristics of AlGaIn/GaN HEMTs.

## 2.6 Temperature Dependent DC Performance

In 1999, Daumiller et.al. [76] studied the effects of temperature on the DC performance of AlGaIn/GaN HEMTs grown by Metal Organic Vapor Phase Epitaxy (MOVPE) on a sapphire substrate. They studied the stress caused by the increased temperature on the  $I - V$  characteristics of AlGaIn/GaN HEMTs. They raised the temperature up to 880 °C and observed that increasing ambient temperature above 600 °C irreversibly degrades the intrinsic heterostructure material. In 2002, Arulkumaran et al. [77] investigated HEMTs performance fabricated on sapphire and SiC substrates. DC characteristics of the fabricated devices were examined at temperatures ranging from 25 to 500 °C. A decrease in  $I_{ds}$  and  $g_m$  with the increase of ambient temperatures were observed. They also reported that both sapphire and SiC substrate HEMTs showed a similar decrease in the ratio of  $g_m$  and  $I_{ds}$  above 300 °C. Additionally, HEMTs on SiC substrate showed better DC characteristics after being subjected to thermal stress up to 500 °C compared to sapphire substrate HEMTs.

TABLE 2.5: Temperature dependent DC performance of GaN-based HEMTs.

Year	Author	Temperature Dependent DC Analysis	Ref.
1999	Daumiller et al.	Different substrates	[76]
2002	Arulkumaran et al.	Different substrates and $g_m$	[77]
2007	Cuerdo et al.	DC parameters with different $L_g$	[78]
2008	Donoval et al.	MOS-HEMT vs HEMT	[79]
2008	Florovic et al.	$g_d$ and $g_m$ characteristics	[80]
2012	Husna et al.	DC characteristics vs Temperature	[81]
2013	Martin et al.	Channel temperature of HEMTs	[82]
2016	Alim et al.	DC parameters of AlGaIn/GaN on SiC substrate	[23]
2017	Muhtadi et al.	DC parameters vs Temperature	[83]

Cuerdo et al. [78] measured temperature dependent DC parameters of AlGaIn/GaN HEMTs of various  $L_g$  fabricated on SiC and sapphire substrates. The study demonstrated that,  $I_{ds}$  and  $g_m$  of AlGaIn/GaN HEMTs on sapphire showed a 35% decrease in magnitude compared with HEMTs fabricated on SiC substrate. In 2008, Donoval et al. [79] analyzed the performance of  $\text{Al}_2\text{O}_3/\text{AlGaIn}/\text{GaN}$  and AlGaIn/GaN HEMTs under varying temperature conditions reaching to 425 °C. Devices DC characteristics including  $g_m$  and  $g_d$  were studied as a function of ambient temperature. Both types of HEMTs exhibited a decrease in the performance with the increase of temperature. All the parameters followed  $T^x$  model where  $x = -1.5$ . This model described that by increasing temperature, the device characteristics deteriorated and this deterioration can be modeled by the negative power of temperature.

Florovic et al. in 2008 [80] investigated  $g_d$  and  $g_m$  characteristics of AlGaIn/GaN HEMTs as a function of temperature ranging from 25 °C to 425 °C, and showed that the device performance continuously degrades with the increase of temperature. Furthermore, the analysis depicted that saturation  $I_{ds}$ , series resistance and maximum  $g_m$  at 425 °C reduces to 30% of its value measured at 25 °C. In 2012, Husna et al. [81] studied the effects of temperature on the DC characteristics of

AlGa<sub>N</sub>/Ga<sub>N</sub> HEMTs fabricated on Si substrate with a thin SiO<sub>2</sub> sheet as a gate dielectric layer. A 30% reduction in  $I_{ds}$  was observed at elevated temperatures. They also fabricated SiO<sub>2</sub>/AlGa<sub>N</sub>/Ga<sub>N</sub> HEMTs on SiC and sapphire substrates and reported, for the same temperature conditions, ~25% and ~38% degradation in  $I_{ds}$ , respectively.

Martin et al. in 2013 [82] proposed a technique to measure the channel temperature of FETs. Their reported technique could be used to study the effects of current and ambient temperature on the device internal channel temperature. In 2016, Alim et al. [23] reported the effects of ambient temperature on the DC parameters of AlGa<sub>N</sub>/Ga<sub>N</sub> HMETs fabricated on SiC substrate. They reported that with the increase of ambient temperature, the value of  $V_{th}$  rises while a degradation in both  $n_s$  and  $\phi_b$  was observed. In 2017, Muhtadi et al. [83] reported AlGa<sub>N</sub>/AlN channel fabricated on sapphire substrate and studied different temperature dependent DC parameters ranging from 25 to 200 °C. Furthermore, they described that  $I_{ds}$ ,  $V_{th}$  and  $g_m$  values remain within  $\pm 15\%$  of their respective average values. Thus, indicating that such devices can comfortably work up to 200 °C.

A summary of temperature dependent investigations carried out by different authors is presented in Table 2.5. It is evident from the review presented in this section that Ga<sub>N</sub> devices, especially Ga<sub>N</sub> HEMT has most robustness to function at elevated temperature. It tries to retain its characteristics at a temperature where other semiconductor devices fail drastically.

## 2.7 Temperature Dependent AC Performance

Islam et al. in 2002 [84] investigated AlGa<sub>N</sub>/Ga<sub>N</sub> HEMTs' small signal characteristics as a function of ambient temperature and observed a nonlinear degradation in the device response. They further observed that this degradation is considerably higher at increased ambient temperature. Additionally, they also reported that relatively long  $L_g$  devices had lower  $f_{max}$  value, which decreases at comparatively lower rate by increasing temperature. Ahmed et al. in 2003 [85] measured  $P_{out}$

and  $G$  of GaN HEMT amplifiers by assessing their small signal parameters. They reported that  $G$  decreases with the increase of frequency as well as temperature. Increasing frequency from 1 GHz to 2 GHz, there is a 1.4% reduction in the magnitude of  $G$  and this value is further reduced at elevated ambient temperature. Thus, the devices showed reduction in  $G$  both because of frequency as well as temperature.

Liu et al. In 2005 [86] investigated variation in small signal and noise parameters of AlGaIn/GaN HEMTs as a function of temperature. They reported that by increasing temperature from 300 K to 573 K,  $G$  reduces monotonically from 12.2 dB to 7.02 dB while  $NF_{min}$  enhances from 1.16 dB to 3.94 dB. In 2006, Palacios et al. [87] investigated access resistance on high frequency operation of AlGaIn/GaN HEMTs caused by increased temperature. They noted that by increasing temperature mobility of 2-DEG carriers reduces while sheet access resistance increases. They used temperature as a controlling parameter to observe the access resistance and noted its effect on the device intrinsic parameters. They also reported that with increasing temperature there is a decrease in  $I_{ds}$  and  $f_T$  along with an increase in the charging delay. In addition to that, they also reported that delay in electron velocity and intrinsic delay remained unaffected by the change of ambient temperature.

Thorsell et al. in 2008 [88] carried out temperature dependent measurements of noise parameters by changing temperature from 298-423 K for AlGaIn/GaN HEMTs. They also investigated the effect of temperature on extrinsic resistances of the device. They observed that the parasitic resistances are the main causes of reduced high frequency functioning of AlGaIn/GaN HEMTs as they have significant effect on the noise performance of the device at high ambient temperature. In 2009, Liu et al. [89] investigated temperature influence on microwave noise performance of AlGaIn/GaN HEMTs fabricated on SiC, sapphire and Si substrates. They calculated and compared the performance of these devices at a wide range of temperature, i.e. from -50 to 200 °C. They reported that GaN HEMTs on Si substrate have an excellent potential for low noise and high temperature applications.



TABLE 2.6: Temperature dependent AC performance of GaN-based HEMTs.

Year	Author	Temperature dependent AC parameters	Reference
2002	Islam et al.	Intrinsic parameters, frequency and power	[84]
2003	Ahmad et al.	Intrinsic parameters and gain	[85]
2005	Liu et al.	Noise figure and frequency	[86]
2006	Nidhi et al.	Time delay and frequency	[87]
2008	Thorsell et al.	Transconductance, noise figure and S-parameters	[88]
2009	Liu et al.	Noise figure, capacitance and gain	[89]
2011	Darwish et al.	Small signal parameters	[90]
2011	Crupi et al.	Parasitic resistance and S-parameters	[91]
2016	Alim et al.	Small signal parameters	[24]

In 2011, Darwish et al. [90] studied the effects of temperature on small signal parameters of GaN and GaAs HEMTs. They varied the ambient temperature from 0-150 °C. They observed that both GaAs and GaN-HEMTs, for the given temperature range, exhibited an increase in parasitic and feedback capacitance values and a reduction in gain when temperature increases. However, the degradation in GaN HEMTs was lower compared to GaAs HEMTs. Crupi et al. [91] investigated effects of ambient temperature on DC and AC performance of GaN-based HEMTs fabricated on SiC substrates. They reported that at high ambient temperature, the device performance degrades, which can be associated with channel heating of the device. In 2016, Alim et al. [24] reported the influence of temperature on small signal parameters of HEMTs. Their study concluded that GaN-based devices have greater potential for high frequency and temperature related applications compared to GaAs based devices.

Table 2.6 presents a summary of investigation carried out by various researchers in determining the temperature dependent AC parameters of GaN HEMTs. It can be said without any ambiguity that HEMT's performance degrades with increasing values of ambient temperature. However, this degradation is relatively lower compared to narrow bandgap HEMTs. Thus, wider bandgap HEMTs, such

as AlGaN/GaN HEMTs have better prospects to be used in microwave power circuitries.

## 2.8 AlGaN/GaN HEMTs Analytical Models

The basic step towards the development of an analytical model is to establish a set of closed form expressions based on the physics of the device capable to predict the device characteristics as a function of applied bias. If such a model would also take into account temperature as a variable, then this could be called as temperature dependent-analytical model. AlGaN/GaN HEMTs are relatively newer, compared to Si or GaAs-based FETs therefore, less efforts are seen in literature pertaining to AlGaN/GaN HEMTs analytical models. Moreover, in these models, very few models have the strength to cater power devices, particularly the temperature effects on the operation of the device.

Lee et al. [92] reported a temperature dependent large signal model for AlGaN/GaN HEMTs. They fabricated the devices using SiC as a substrate. Their model takes into account the dependence of RF scattering and capacitance elements on ambient temperature. In 2005, Chang et al. [93] reported a temperature dependent  $I - V$  model for AlGaN/GaN HEMTs. They incorporated successfully temperature dependent energy bandgap discontinuity and spontaneous piezoelectric polarization in their model. In 2005, Huq and Islam et al. [94, 95] presented temperature dependent charge control analytical model. In their work, although they presented the device temperature dependent characteristics however, they have not considered piezoelectric effect as a variable in their model. This puts constraints on their model and thus on the model's applicability. In 2006, Chattopadhyay et al. [96] reported a temperature and 2-DEG polarization dependent analytical model for gate capacitance-voltage characterization of partially relaxed and fully-strained AlGaN/GaN HEMTs. They studied temperature dependence bandgap discontinuity,  $V_{th}$ ,  $n_s$ , and gate capacitance. They reported that  $n_s$  and

TABLE 2.7: Temperature dependent models of GaN-based HEMTs.

Year	Author	Temperature Dependent Model	Ref.
2004	Lee et al.	Large signal model	[92]
2005	Change et al.	Numerical simulation for DC characteristics	[93]
2006	Huq et al.	Charge control model	[95]
2006	Chattopadhyay et al.	Gate capacitance model	[96]
2008	Chattopadhyay et al.	Channel temperature	[22]
2009	Huque et al.	Analytical model for DC characteristics	[17]
2013	Wang et al.	Analytical model for DC characteristics	[97]

$V_{th}$  showed none or minimum change with temperature while gate capacitance showed variation at higher  $V_{gs}$ .

In 2008, Manju et al. [22] developed a temperature dependent model, which also included self-heating effects to predict DC characteristics of AlGaIn/GaN HEMTs. In their model, a polynomial based relationship between  $n_s$  and Fermi level was considered. They also studied the temperature effects on various DC parameters such as saturation velocity, electron mobility, polarization and thermal conductivity. They successfully applied their model on GaN HEMTs and demonstrated its functionality in a limited manner.

In 2009, Huque et al. [17] developed an analytical model for temperature dependent  $I - V$  characteristics of AlGaIn/GaN HEMTs. Their model included the effect of ambient temperature on various DC parameters such as energy bandgap discontinuity, carrier mobility, saturation velocity,  $n_s$  and  $V_{th}$ . For the accuracy of their proposed analytical model, they compared the modeled and the experimental characteristics for a wide range of temperature, i.e. 300-500 K.

Wang et al. in 2013 [97] proposed a temperature dependent model for DC characterization of AlGaIn/GaN power HEMTs. They proposed temperature dependent closed form expressions to model the ambient temperature effects on the Schottky barrier height, conduction band discontinuity at heterojunction interface of

AlGaN/GaN and  $n_s$ . To ensure the validity of the model, they compared their modeled results with the experimental data and demonstrated a reasonable accuracy.

A summary of temperature dependent analytical models discussed hitherto is shown in Table 2.7, wherein a systematic progression in GaN HEMTs analytical models is presented. Although, number of models do exist to predict the temperature dependent characteristics of GaN HEMTs, but they are of limited use because, they are not comprehensive enough to cater all the scenarios. Thus, still there is a need to develop a comprehensive analytical model, which should accommodate all the variables that could possibly affect the device characteristics. The validity of the developed model can then be checked for the devices of varying dimensions to ensure its global applicability both for DC and AC characteristics.

## 2.9 AlGaN/GaN HEMTs Numerical Models

As mentioned before, GaN HEMT is introduced by Khan et al. in 1993 [52] and during earlier stages, GaN HEMTs were fabricated on Si/SiC substrates. However, with the availability of GaN substrate, the quality of the transistor has improved manifold, and now the device is engaged quite often in high-tech microwave power applications [2, 98, 99].

It is a known fact that the performance of a GaN HEMT deteriorates when its lattice gets heated because of intense electric field inside the channel. Temperature dependent effects contribute adversely towards the performance of the device and it is therefore, important that one should know the operating conditions in which the device is supposed to be functioning. Additionally, in power related applications, such devices are placed in an environment where the temperature is higher than the room temperature, which further aggravates the operating conditions for the device. In Ref. [100], it is shown that the ambient temperature further increases the channel temperature of the device and its ultimate operating capability gets affected with increasing ambient temperature. They also showed that the device

TABLE 2.8: Non-linear models of GaN-based HEMTs.

Year	Author	Non-Linear Model	Ref.
1985	Curtice et al.	100% empirical	[101]
1990	McCamant et al.	Semi-empirical	[102]
1999	Angelov et al.	100% empirical	[103]
2004	Dobes et al.	Semi-empirical	[104]
2004	Islam et al.	Semi-physical	[105]
2016	Riaz et al.	Semi-physical	[106]

channel temperature, which controls its characteristics, depends on the device physical parameters and its geometry.

Dependence of GaN HEMT performance on numerous parameters requires a compact model to simulate the device characteristics both at room as well as at elevated temperature. A compact device model would be the one, which can predict the device  $I_{ds}$  as a function of  $V_{ds}$  and  $V_{gs}$ . It should adequately address the influence of ambient temperature and self-heating on the device characteristics. Moreover, the model should also explain changes in  $I_{ds}$  with varying device physical parameters; such as  $L_g$ ,  $W$ ,  $V_{th}$  and  $n_s$ , etc. It should also have the flexibility to be employed in simulation software to extend the device knowledge into circuits involving GaN HEMTs [107, 108].

A review of GaN HEMTs models has been carried out by Santi et al. in 2015, wherein it was observed that very few models have been proposed to simulate GaN HEMT characteristics for power related applications [108]. Physics based models are too complicated [109–111] to be employed in a circuit simulation software and usually semi-physics or numerical techniques are used to predict fundamental characteristics of the device in computer aided design (CAD). According to our assessment, numerical models developed for GaAs MESFETs are being used to simulate  $I - V$  characteristic of GaN HEMTs; as an example in [112], Curtice model developed for MESFET has been employed to simulate GaN HEMT characteristics. GaAs MESFETs models [101–106] are bound to lose their accuracy

when the device characteristics exhibit noticeable self-heating effect.

Table 2.8 illustrates a list of numerical models, which have been developed so far to simulate FET devices and they are routinely used in simulation software. Curtice model does not involve the physical parameters of the device and it consists of a non-linear expression having numerous variables to be optimized to achieve the device output characteristics as a function of  $V_{ds}$  and  $V_{gs}$ . If a designer will use this expression he will not have an idea how the device characteristics will be affected by varying the device physical dimensions e.g.  $L_g$ ,  $W$ , etc. Thus, this techniques can only be employed on the finished devices and not on those devices which are ought to be fabricated. And the same is true for Angelov model therefore, both have been shown in the table as 100% empirical models. Remaining models listed in Table 2.8 or either semi-empirical or semi-physical based on the biasness of a model either more towards empirical or physical, respectively. It is pertinent to mention here that, none of the models takes into account temperature effects usually observed in GaN HEMTs. Thus, they cannot reflect with reasonable accuracy, the  $I - V$  characteristics of AlGaIn/GaN HEMTs. This necessity leads to the development of a numerical model, especially designed for GaN-based HEMTs meant, for power related applications.

## 2.10 Research Gaps

As explained in Chapter 1, AlGaIn/GaN based HEMTs are preferred devices for high frequency and high power applications, especially at elevated temperature and for harsh environment. Development of an accurate analytical model would be a fundamental requirement to have a better understanding about the functioning and operational capabilities of the device. This could possibly lead to the device optimization both from the material as well as from the device structure/geometry point of view.

A very few temperature dependent analytical models of AlGaIn/GaN HEMT exist in literature and none of the existing models have global applicability due to

severe constraints imposed simultaneously by the device geometry and material characteristics involved in the device fabrication. Hence, majority of the reported characteristics are of experimental nature. As discussed in Section 2.8, temperature dependent analytical models are reported but they are of limited use. Huq [95] developed a temperature dependent analytical model based on simplified physics of the device and therefore, it offers limited device operational understanding. In [95], authors reported temperature dependent modeled characteristics of HEMTs, but their proposed approach was by and large empirical; based on a nonlinear cubic Curcice expression. Furthermore, the accuracy of the reported technique was not verified at elevated temperature.

In [17], Huque et al. developed a temperature dependent analytical model for AlGaIn/GaN HEMT. They covered only temperature dependent DC characterization of AlGaIn/GaN HEMT. Moreover, the functioning of the model was not checked for temperature dependent small signal parameters of the device; whereas, in the proposed study, we intend to develop a comprehensive temperature dependent model, both for DC as well as for AC characterization of the device.

From the design point of view, it is always desired to have a model which can predict device characteristics without involving much details about the device physics and material characteristics. Such models are commonly referred to as numerical models. Wang et al. [97] proposed a temperature dependent empirical model for AlGaIn/GaN power HEMTs, but with limited scope. So, in addition to the analytical HEMT model as discussed in the preceding paragraphs, this work will also focus on the development of a numerical model for high power microwave HEMTs, for the design engineers, with an aim that the same could be employed in CAD software involving high power GaN HEMTs. The following would be carried out during the proposed research work:

1. Development of an analytical model for DC characterization of power HEMTs with special emphasis on high temperature applications.
2. Development of a physics based analytical model for AC parameters characterization at elevated temperature using DC characterization.

3. Development of a numerical model for microwave GaN based HEMTs to simulate DC characteristics both at room as well as at elevated temperature.

## 2.11 Methodology

Our work is primarily focused on modeling and simulation techniques of GaN HEMTs. Modeling will be carried out using physical parameters of the device having two aspects: a) wafer parameters and b) the device design parameters. Major wafer parameters include layer structure, 2-DEG characteristics, mobility and velocity of free carriers offered by the wafer; whereas, device parameters include: device width and length; depletion layer geometry; gate-drain and gate-source separation; device topology; carriers concentration; built-in potential and parasitic components, etc. By involving these parameters, one can evaluate field distribution inside the channel, which effectively control the flow of carriers and thus, the device characteristics. On the other hand, the capacitive and inductive nature of the device electrical parameters determine its AC response.

An expression which can logically link the device design parameters, influenced by the device wafer parameters, and can generate either DC or AC response, compatible to that of observed response (within 10% margin) would be referred to as device physical (analytically) model. An appropriately perceived polynomial or a non-linear expression, involving less physics but controlled by the device bias ( $V_{gs}$ ,  $V_{ds}$ ) voltages capable to generate device characteristics, through an optimization process, which matches with the experimental data to an acceptable margin would be called as a numerical model. In this research, both of these techniques would be engaged to model GaN based HEMTs, for room and elevated temperature applications, by employing following consideration:

1. Considering the device geometry, nature of the Schottky barrier and band discontinuity, field distribution inside the channel would be evaluated by solving Poisson equation with appropriate boundary conditions. This would



lead to the assessment of channel current. Temperature effects would then be added into the model which could possibly affect the device performance on three counts: a) Schottky barrier depletion modification; b) hot carriers generation and scattering into the buffer layer and their subsequent collection by the drain electrode and c) 2-DEG modification. The proposed model would comprehensively incorporate all these variables and its validity would be ensured by comparing it with the experimental  $I - V$  characteristics of the devices, especially made for microwave power applications.

2. Since the assessment of a FET AC parameters is a cumbersome task and it is, therefore, also proposed that by involving the technique discussed in (1) first the device  $I - V$  characteristics would be modeled and then based on the modeled characteristics, AC parameters would be extracted. The difference between the proposed and already reported work would be that the proposed work would be based on modeled  $I - V$  characteristics whose accuracy would first be established by comparing the modeled characteristics with the experimental data. Thus, one can assume a better accuracy, in the estimated AC parameters, which for validation purposes would also be compared with the experimental data.
3. Finally, an improved AlGaIn/GaN HEMT equivalent circuit will be developed by knowing the following:
  - i. Gate-to-source capacitance,  $C_{gs}$ ;
  - ii. Gate-to-drain capacitance,  $C_{gd}$ ;
  - iii. Transconductance,  $g_m$ ;
  - iv. Parasitic resistances,  $R_s, R_d, R_g$ ;
  - v. Drain-to-source capacitance,  $C_{ds}$ ;
  - vi. Unity gain frequency,  $f_T$ ;
  - vii. Channel resistance,  $R_i$ ;
  - viii. Output conductance.  $g_d$  and
  - ix. Transit time,  $\tau$ .

4. For a range of gate lengths and widths, a numerical model would also be developed wherein, it is aimed that modeled parameters would be optimized using swarm optimization technique. The proposed numerical model, as perceived, would have less physical aspects however, it would be strong enough to generate the device  $I-V$  and transfer characteristics by involving  $V_{ds}$ ,  $V_{gs}$ , and  $V_{th}$  along with variables pertaining to the device geometry, i.e.  $L_g$ ,  $W$ , etc. Starting point to achieve this target would be the FET's fundamental square law expression, which describes in a very primitive way, the device characteristics in the saturation region of operation. Linear region would be incorporated either by involving hyperbolic tangent function or any other suitable mathematical expression, to generate the desired non-linearity of the device output characteristics. Finite output conductance ( $g_d$ ), as usually observed, after the onset of velocity saturation, would be taken care of by defining an appropriate function which should be  $V_{ds}$  dependent but  $V_{gs}$  independent. Self heating effects, which are routinely observed in high power HEMTs would also be added into the model by adding an additional non-linearity in those terms responsible to control the characteristics in the saturation region of operation. The developed expression would be treated as a fundamental expression, which would then be extended to evaluate other parameters of the device, e.g.  $g_d$ ,  $g_m$ , etc.

## 2.12 Summary

This chapter discusses the 3<sup>rd</sup> generation wide bandgap semiconductors (SiC and GaN) and their potential use in microelectronic industry. It has been discussed that for high power and harsh environment applications, characteristics offered by narrow bandgap semiconductors (Si, GaAs) are insufficient and one has to opt for wide bandgap semiconductors. GaN as a wide bandgap semiconductor offers excellent characteristics and can therefore be employed in device fabrication especially in high-tech devices such as HEMTs. It is discussed that fabrication of HEMTs using GaN in conjunction with another wide bandgap material such as

AlGa<sub>N</sub>; to achieve bandgap discontinuity, can be attained without having a dopant layer, because of the piezoelectric effect found inherently in these layers. This provides an added advantage of increased velocity because of the absence of donor ions, which could possibly act as scattering centers for the drifting carriers. Owing to these facts, GaN based HEMTs are preferred for microwave power applications.

At high power and in harsh environment, deterioration in a semiconductor device characteristics is a natural phenomenon and the same has been dually emphasized in this chapter. However, it is also discussed that GaN HEMTs have higher resilience to these changes, because of high thermal conductivity and wide bandgap nature of the device material.

For the advancement of GaN HEMTs, it is imperative that the device operation and its dependence on external and internal variables should be better understood. In this connection, the importance of an analytical model is discussed in this chapter. The chapter also summaries numerous models presented and the limitations associated with them. It has been established that there is still room to have a comprehensive model, which could predict the device DC and AC characteristics, both at room as well as at elevated temperature, with a good degree of accuracy.

It is further discussed that the device's growth is greatly dependent on its applications in the power industry. This requires a technique that allows the device integration into power circuitry through a computer aided design (CAD). Contemplating the CAD specific needs, it is established that a numerical model based on semi-physical approach would be a useful one. Since there is no such model developed so far exclusively for GaN HEMTs therefore, the need to have such a model is emphasized in the chapter. The chapter finally gives methodology, which would be employed to achieve the stated research objectives.

# Chapter 3

## HEMT's Temperature Dependent Analytical DC Model

### 3.1 Introduction

Semiconductor devices are the main building blocks of modern electronic systems, being responsible for key advances. One of the key expectations from electronic devices in the modern era is to enable and control systems that operate in extreme environments. The effects of temperature on device operation have been of great interest throughout the history of semiconductor research [17, 22, 23, 70, 93, 97, 113, 114]. Wide-bandgap devices such as GaN HEMTs have proven to be superior to their counterparts due to their relatively: (a) high carrier mobility,  $\mu \sim 1500 \text{ cm}^2 \text{ V}^{-1} \text{ s}^{-1}$ , (b) high saturation velocity,  $v_{sat} \sim 2.5 \times 10^7 \text{ cm s}^{-1}$ , and (c) high breakdown voltage  $\sim 3.3 \text{ MV cm}^{-1}$  [2, 6], making them preferred candidates for use in high-temperature applications in the microwave regime. To achieve increased drain current, high sheet charge concentration ( $n_s$ ) is required. Use of a AlGaN/GaN heterojunction in HEMTs results in a relatively high value of  $n_s$  in the form of a 2-DEG, enabling the device to provide high drain current for given bias.

The intrinsic carrier concentration ( $n_i$ ) of a semiconductor material is a temperature-dependent parameter [115]. As temperature increases, so does the carrier generation rate. For GaN semiconductor, the dependence of  $n_i$  on temperature is five times weaker than for Si [116], making devices more robust for high-temperature operation. Therefore, the low  $n_i$  at high temperature coupled with the high breakdown field due to the wide bandgap make GaN-based devices highly suitable for use in elevated-temperature applications.

In addition to the superior and well-controlled material characteristics of AlGaIn/GaN HEMTs, the characteristics of such devices can be further improved by optimizing fabrication parameters, one of the most important of which is the quality of the device Schottky barrier junction ( $\phi_b$ ), which is also sensitive to temperature [117, 118]. Device performance can be significantly degraded by increased ambient temperature. By their very design, AlGaIn/GaN HEMTs are meant to be operated at relatively high bias, which can result in modification of the junction height [106, 119]. Such a modification will then directly impact on the device output current, rendering the characteristics of the device temperature dependent.

It is an established fact that  $\mu$  is sensitive to lattice temperature [120]. In general, at high bias, the strength of the electric field underneath the Schottky barrier causes the lattice temperature to rise. The lattice temperature will also rise when the device is operated in a harsh environment. At elevated temperature, the lattice vibrates with increased amplitude, thus offering a greater obstacle to flow of free carriers; the resulting increased reduces  $\mu$  [121, 122].

The characteristics of a HEMT device are primarily determined by  $n_s$ , which is mainly dependent on the bandgap discontinuity ( $\Delta E_c$ ), determined by the layer structure of the HEMT [31, 123]. The position of the Fermi level ( $E_F$ ), which is also a temperature-dependent parameter [124], determines the  $n_s$  available in the layer structure of the device, which can possibly tunnel to the quantum states at the interface of the layers defining the 2-DEG. Therefore, any variation in the temperature will cause a change in  $E_F$ , eventually translating into a change in  $n_s$  [125].

For improved device modeling, especially at elevated temperature and at high bias, it is important that all four variables discussed above be considered. To the best of the authors' knowledge, no such models comprehensively taking into account all four variables, namely the (a) Schottky barrier,  $\phi_b(T)$ , (b) mobility,  $\mu(T)$ , (c) bandgap discontinuity,  $\Delta E_c(T)$ , and (d) saturation velocity,  $v_{sat}(T)$ , as temperature dependent variables have been reported in literature.

In [114], Albrecht et al. used Monte Carlo simulation to determine temperature-dependent parameters such as  $\mu$  and  $v_{sat}$ . Chang et al. developed a temperature-dependent model for static characterization of AlGaIn/GaN HEMTs, using a numerical technique in which the Poisson and Schroedinger equations were solved [93].

In 2006, Huq et al. [95] developed an analytical model for the  $I - V$  characteristics of GaN HEMTs by taking into account  $\mu$ ,  $v_{sat}$ ,  $n_s$ , and the thickness of layers. They proposed that AlGaIn/GaN HEMTs can comfortably operate up to 600K at microwave frequencies. However, in their model,  $E_F$  was not taken as a temperature-dependent variable, making it prone to errors in the evaluation of  $n_s$ .

In 2008, [22] reported a modified thermal model for the  $I - V$  characteristics of AlGaIn/GaN-based HEMTs, representing an extension of the work of DasGupta et al. [126]. In that model,  $E_F$  was associated with  $n_s$  through a polynomial expression, thus requiring a numerical technique to determine the coefficients of the polynomial. The performance of the model was tested at room temperature by considering the self-heating effects caused by high bias, but its performance at elevated temperature was not assessed.

In 2009, Huque et al. [17] also reported an analytical model for the temperature-dependent  $I - V$  characteristics of AlGaIn/GaN HEMTs. In their model, they considered  $n_s$  as a temperature- and bias-dependent variable, while the dependence of  $E_F$  on  $n_s$  was represented using the same polynomial as in [22, 125]. Huque et al. incorporated a temperature-dependent  $\Delta E_c$  into their model to obtain the temperature-dependent  $I - V$  characteristics. However, in their modeling,  $\phi_b$  was

treated as a constant, thus their expression might not accurately model devices in which  $\phi_b$  is temperature sensitive.

In 2013, Wang et al. [97] developed a temperature-dependent model for AlGaIn/GaN HEMTs by evaluating the temperature-dependent  $\mu$  and  $n_s$ . Based on these two variables, they reported limited modeled characteristics for AlGaIn/GaN HEMTs; their reported data reveal poor performance of the proposed model, especially in the linear region of operation. Furthermore, they demonstrated the applicability of the model at relatively low ( $V_{ds} \sim 8$  V) bias, whereas such devices are intended for high-bias operation ( $V_{ds} \gtrsim 15$  V). Moreover, their model involved a number of empirical constants without any physical justification, making it difficult to claim that it represents an analytical model. Also, at high gate bias, the model may not follow experimental data, which were also not shown.

In the work presented herein, an effort was made to develop a comprehensive temperature-dependent model to predict device  $I - V$  characteristics at elevated temperature with a high degree of accuracy. The model was developed by evaluating the temperature-dependent  $\phi_b(T)$ ,  $\Delta E_c(T)$ ,  $v_{sat}(T)$ , and  $\mu(T)$ , followed by their use to evaluate the  $I - V$  characteristics. The developed technique was applied at different biases and temperatures to assess its accuracy, and the results compared with reported models. The remainder of this manuscript is organized as follows: Section 3.2 discusses model development, Section 3.3 presents a comparison between experimental and modeled data with an associated discussion, whereas Section 3.4 presents the conclusions that can be drawn from the results.

## 3.2 Model Development

Use of an analytical model is the most appropriate technique to determine the  $I - V$  characteristics of a HEMT for a particular application. With increase in the output power, the channel temperature increases, degrading device performance. To develop an analytical HEMT model, one starts from the fundamental concept of the heterojunction material, which is a key parameter for the generation of the

2-DEG [97]. Then, incorporation of the channel fields caused by the drain and gate bias provides an expression that can generate the  $I - V$  characteristics of the HEMT as a function of the drain to source ( $V_{ds}$ ) and gate to source ( $V_{gs}$ ) voltages.

The variable  $\mu$  plays a significant role in defining the  $I - V$  characteristics of a HEMT. The bias-dependent mobility,  $\mu(V)$ , of the 2-DEG carriers in a HEMT device can be expressed as [127]

$$\mu(V) = \frac{\mu_0}{1 + [\theta(V_{gs} - V_{th})]^\beta} \quad (3.1)$$

where  $\theta$  and  $\beta$  are fitting parameters,  $V_{th}$  is the threshold voltage, and  $\mu_0$  is the low field mobility of electrons given as [22, 128]

$$\mu_0 = \mu_{min} + \frac{\mu_{max} - \mu_{min}}{1 + (n_s/n_r)^\alpha} \quad (3.2)$$

where  $\mu_{min}$  and  $\mu_{max}$  are the minimum and the maximum mobility, respectively,  $n_r$  is the reference carrier concentration, and  $\alpha$  is a fitting parameter. It is proposed that temperature dependent  $\Delta E_c(T)$  between two layers of an AlGaIn/GaN HEMT can be defined as

$$\Delta E_c(T) = (E_g^A - E_g^G)\lambda_1 \times \text{Exp}[-\Delta T/T_f] \quad (3.3)$$

where  $E_g^A$  and  $E_g^G$  are the bandgaps of AlGaIn and GaN, respectively,  $\lambda_1$  is an adjustment parameter, and  $\Delta T$  is the temperature difference, given as

$$\Delta T = T_f - T_i \quad (3.4)$$

where  $T_f$  and  $T_i$  represent the final and initial temperatures, respectively.

Since the barrier height  $\phi_b$  of a GaN HEMT varies with temperature, it is proposed that

$$\phi_b(T) = \phi_{b0} (1 - \lambda_2 \times \text{Exp}[\Delta T/T_f]) \quad (3.5)$$

In Eq. (3.5), when  $\Delta T = 0$ , this leads to  $\lambda_2 = 0$ ; which gives  $\phi_b = \phi_{b0}$ . Equations (3.3) and (3.5) can be used to predict  $\Delta E_c(T)$  and  $\phi_b(T)$ , respectively, by setting



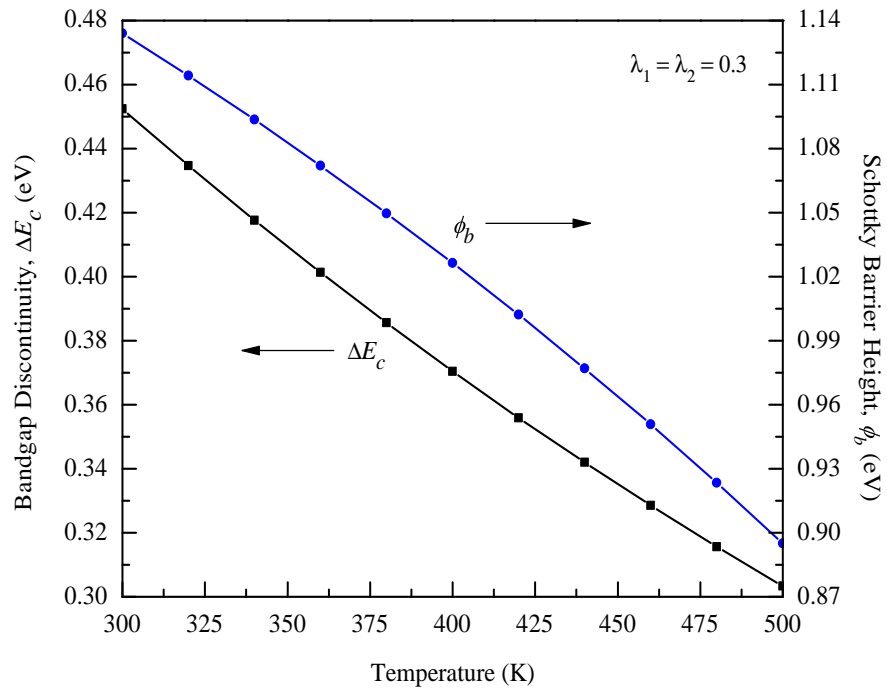


FIGURE 3.1: Variation in Schottky barrier,  $\phi_b$  and bandgap discontinuity,  $\Delta E_c$  as a function of temperature for an AlGaIn/GaN heterojunction HEMT.

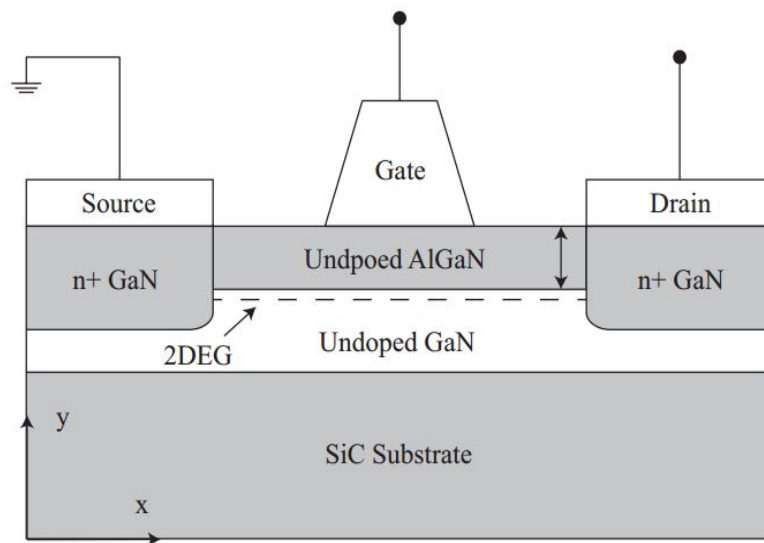


FIGURE 3.2: A cross-sectional view of an AlGaIn/GaN HEMT.

the appropriate fitting parameters, as shown in Fig. 3.1.

It is an established fact that the  $V_{th}$  of a HEMT varies as [126]

$$V_{th} = \phi_b(T) - \Delta E_c(T) - \frac{qN_d d^2}{2\varepsilon_s} \quad (3.6)$$

where  $\varepsilon_s$  is the permittivity of the semiconductor,  $d$  is the separation of the 2-DEG from the Schottky barrier gate,  $q$  is the electron charge, and  $N_d$  is the doping density.

As shown in Fig. 3.2, it is not always a mandatory requirement to have a doped layer underneath the Schottky barrier to release carriers for the 2-DEG. Carriers can also be generated under polarization effects, which requires a modified definition of  $V_{th}$ , given as [17, 18]

$$V_{th} = \phi_b(T) - \Delta E_c(T) - \frac{\sigma d}{\varepsilon_s} \quad (3.7)$$

where  $\sigma$  defines the polarization-controlled surface charge density.

In an AlGaIn/GaN heterojunction, the  $n_s$  of a 2-DEG is given by [17]

$$n_s = \frac{\varepsilon_s}{qd} [V_{gs} - V_{th} - E_F - V(x)] \quad (3.8)$$

where  $V(x)$  represents the potential drop inside the channel at location  $x$ . The variable  $n_s$  is of prime importance in defining the device characteristics. At elevated temperature,  $n_s$  will vary, thus affecting the position of  $E_F$ . In [125], DasGupta et al. proposed a relationship between  $E_F$  and  $n_s$  given as

$$E_F = \xi_1 + \xi_2 n_s^{1/2} + \xi_3 n_s \quad (3.9)$$

where  $\xi_{1,2,3}$  are temperature dependent constants. Combination of Eqs. (3.8) and (3.9) readily provides a quadratic expression in  $n_s$ , having a solution

$$n_s = \frac{\varepsilon_s}{qd} (V_g - V_{th} - \xi_1 - \xi_2 n_s^{1/2} - \xi_3 n_s) \quad (3.10)$$

$$n_s = \frac{\varepsilon_s}{qd} (V_g - V_{th} - \xi_1) - \frac{\varepsilon_s}{qd} (\xi_2 n_s^{1/2} - \xi_3 n_s) \quad (3.11)$$

$$n_s + \frac{\varepsilon_s}{qd}(\xi_2 n_s^{1/2} - \xi_3 n_s) - \frac{\varepsilon_s}{qd}(V_g - V_{th} - \xi_1) = 0 \quad (3.12)$$

$$n_s(1 + \frac{\varepsilon_s}{qd}\xi_2) + \frac{\varepsilon_s}{qd}\xi_2 n_s^{1/2} - \frac{\varepsilon_s}{qd}(V_g - V_{th} - \xi_1) = 0 \quad (3.13)$$

Let

$$C = \frac{\varepsilon_s}{qd} \quad (3.14)$$

$$n_s(1 + C\xi_2) + C\xi_2 n_s^{1/2} - C(V_g - V_{th} - \xi_1) = 0 \quad (3.15)$$

Let

$$A = (1 + C\xi_2) \quad \text{and} \quad B = C\xi_2 \quad (3.16)$$

$$An_s + Bn_s^{1/2} - C(V_g - V_{th} - \xi_1) = 0 \quad (3.17)$$

Eq. (3.17) gives a quadratic equation to represent the 2-DEG sheet charge carrier concentration at the AlGa<sub>N</sub>/Ga<sub>N</sub> heterointerface as

$$n_s^{1/2} = \frac{-B + \sqrt{B^2 + 4AC(V_g - V_{th} - \xi_1)}}{2A} \quad (3.18)$$

$$n_s^{1/2} = \frac{-C\xi_2 + \sqrt{C^2\xi_2^2 + 4(1 + C\xi_2)(V_g - V_{th} - \xi_1)}}{2(1 + C\xi_2)} \quad (3.19)$$

$$n_s^{1/2} = \frac{-\xi_2 + \sqrt{\xi_2^2 + 4(\frac{1}{C} + \xi_2)(V_g - V_{th} - \xi_1)}}{2(\frac{1}{C} + \xi_2)} \quad (3.20)$$

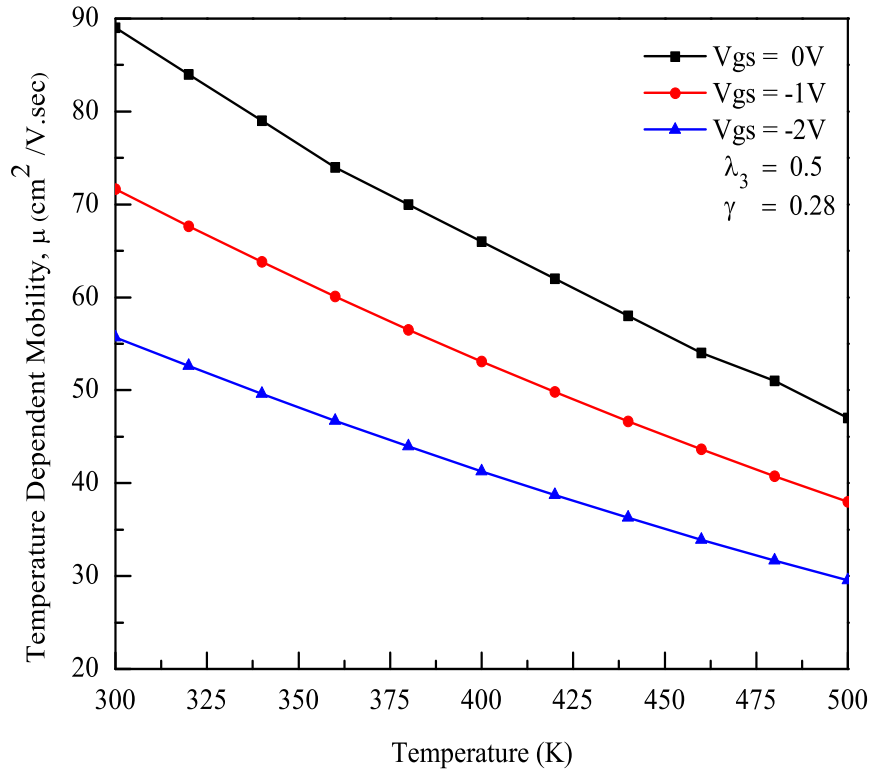


FIGURE 3.3: Variation in mobility,  $\mu$  of an AlGaIn/GaN 2-DEG carriers as a function of temperature and gate bias.

Substituting the value of  $C$  from Eq. (3.14)

$$n_s^{1/2} = \frac{-\xi_2 + \sqrt{\xi_2^2 + 4\left(\frac{qd}{\epsilon_s} + \xi_2\right)(V_g - V_{th} - \xi_1)}}{2\left(\frac{qd}{\epsilon_s} + \xi_2\right)} \quad (3.21)$$

$$n_s = \left[ \frac{-\xi_2 + \sqrt{\xi_2^2 + 4\xi_4(V_{gs} - V_{th} - V(x) - \xi_1)}}{2\xi_4} \right]^2 \quad (3.22)$$

where

$$\xi_4 = \xi_3 + \frac{qd}{\epsilon_s} \quad (3.23)$$

It is an established fact that the magnitude of  $\mu$  is a function of temperature [17, 22]. At elevated temperature, the amplitude of lattice vibration increases, causing increased scattering and thus, reducing  $\mu$ . An expression to simulate this effect is proposed as

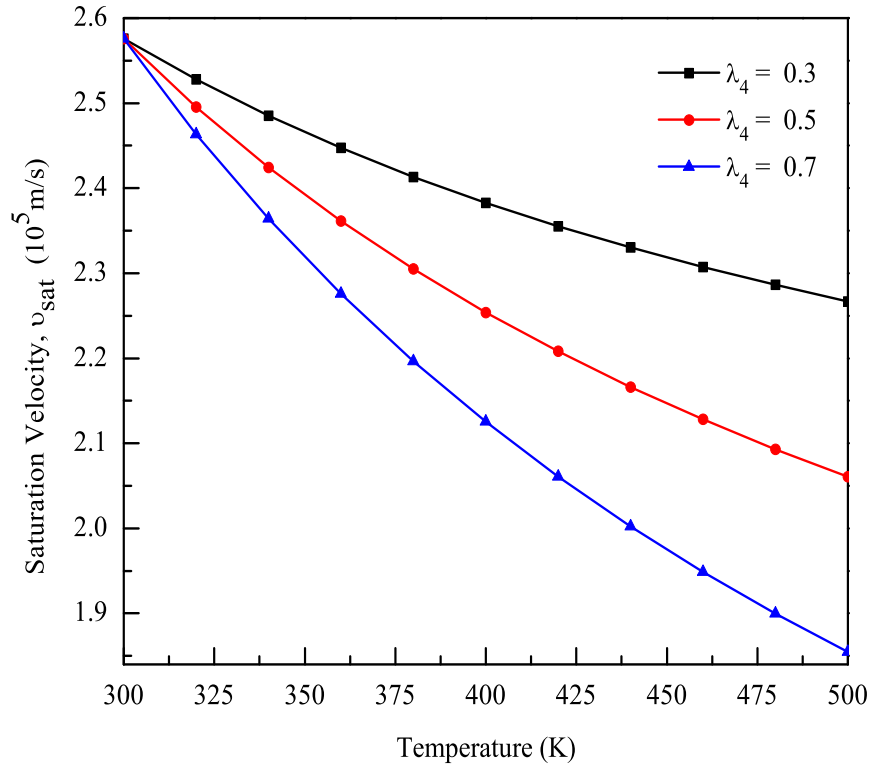


FIGURE 3.4: Variation in  $v_{sat}$  of an AlGaIn/GaN 2-DEG as a function of temperature.

$$\mu_T = \mu(V)[1 - \lambda_3(\Delta T/T_f)]^\gamma \quad (3.24)$$

where  $\gamma$  is a fitting parameter. Equation (3.24) models the variation in  $\mu$  with respect to temperature and  $V_{gs}$ , as shown in Fig. 3.3.

To evaluate the  $I - V$  characteristics, it is proposed that the temperature dependence of  $v_{sat} = E_{sat}\mu_T$  can be simulated as

$$v_{sat}(T) = v_0[1 - \lambda_4(\Delta T/T_f)] \quad (3.25)$$

where  $v_0$  is the velocity of 2-DEG carriers at  $T = 300$  K and  $\lambda_4$  is an adjustment factor. The variation in  $v_{sat}$  as a function of temperature for a given value of  $v_0$  is shown in Fig. 3.4

It is pertinent to mention here that the drift velocity of electrons,  $v_d(x)$ , at any point  $x$  in the channel is a function of the applied field  $E_x$ , and its value before

and after  $2E_{sat}$  is given by Eq. (3.26) [127]

$$v_d(x) = \begin{cases} \frac{\mu_0 E_x}{1 + E_x/2E_{sat}}, & \text{for } E_x = dV(x)/dx < 2E_{sat} \\ v_{sat}, & \text{for } E_x = dV(x)/dx > 2E_{sat} \end{cases} \quad (3.26)$$

For  $E_x > 2E_{sat}$ , the value of  $v_{sat}$  can thus be evaluated using Eq. (3.25).

### 3.2.1 $I - V$ Characteristics

The drain current ( $I_{ds}$ ) of a GaN HEMT is associated with  $n_s$  and  $v_d(x)$  and is given by

$$I_{ds} = qWn_s v_d(x) \quad (3.27)$$

where,  $W$  is the channel width of the device.

By changing  $V_{ds}$ ,  $I_{ds}$  changes, and this variation is linear for small  $V_{ds}$ , then saturates ( $I_{ds}$ ) at an applied  $V_{ds}$  referred to as  $V_{d(sat)}$ . In general, the  $I - V$  characteristics of a HEMT will have a linear region where carriers are drifting below  $v_{sat}$  and a saturation region, wherein carriers are drifting with  $v = v_{sat}$  [22].

#### 3.2.1.1 Linear Region Current ( $V_{ds} < V_{d(sat)}$ )

In the linear region, the current  $I_{dl}$  can be evaluated by combining Eqs. (3.26) and (3.27) then integrating it over the entire channel

$$I_{d(lin)} = \frac{2(qWv_{sat})}{\xi_4(2V_L + V_{ds})} \int_0^{V_{ds}} n_s dV \quad (3.28)$$

Substituting  $n_s$  from (3.22) and consider that  $V_{g1} = V_{gs} - V_{th} - \xi_1$

$$I_{d(lin)} = \frac{2\xi_4\Psi}{2V_L + V_D} \int_0^{V_{ds}} \left( \frac{\sqrt{\xi_2^2 + 4\xi_4(V_{g1} - V(x))} - \xi_2}{2\xi_4} \right)^2 dV \quad (3.29)$$

$$I_{d(lin)} = \frac{\Psi}{2\xi_4(2V_L + V_{ds})} \int_0^{V_{ds}} \left( \xi_2^2 + 4\xi_4(V_{g1} - V(x)) + \xi_2^2 - 2\xi_2^2 \sqrt{\xi_2^2 + 4\xi_4(V_{g1} - V(x))} \right) dV \quad (3.30)$$

$$I_{d(lin)} = \frac{\Psi}{2V_L + V_{ds}} \left( \left[ \frac{\xi_2^2}{\xi_4} V + 2V_{g1}V(x) - V(x)^2 \right] \Big|_0^{V_{ds}} - \int_0^{V_{ds}} \frac{\xi_2}{\xi_4} \sqrt{\xi_2^2 + 4\xi_4 V_{g1} - 4\xi_4 V(x)} dV \right) \quad (3.31)$$

$$\because \int \sqrt{ax + b} dx = \left( \frac{2b}{3a} + \frac{2x}{3} \right) (\sqrt{ax + b}) \quad (3.32)$$

$$I_{d(lin)} = \frac{\Psi}{2V_L + V_{ds}} \left( \frac{\xi_2^2}{\xi_4} V_{ds} + 2V_{g1}V_{ds} - V_{ds}^2 - \left[ \left( \frac{\xi_2^2 + 4\xi_4 V_{g1}}{-6\xi_4} + \frac{2V(x)}{3} \right) \left( \frac{\xi_2}{\xi_4} \right) \sqrt{\xi_2^2 + 4\xi_4 V_{g1} - 4\xi_4 V(x)} \right] \Big|_0^{V_{ds}} \right) \quad (3.33)$$

Using the approximation  $[4\xi_4 V(x) \ll \xi_2^2 + 4\xi_4 V_{g1}]$

$$I_{d(lin)} = \frac{\Psi}{2V_L + V_{ds}} \left( \frac{\xi_2^2}{\xi_4} V_{ds} + 2V_{g1}V_{ds} - V_{ds}^2 - \left[ \left( \frac{\xi_2^2 + 4\xi_4 V_{g1}}{-6\xi_4} + \frac{2V(x)}{3} \right) \left( \frac{\xi_2}{\xi_4} \right) \sqrt{1 + \frac{4\xi_4 V_{g1}}{\xi_2^2}} \right] \Big|_0^{V_{ds}} \right) \quad (3.34)$$

$$\begin{aligned}
I_{d(lin)} = & \frac{\Psi}{2V_L + V_{ds}} \left[ \frac{\xi_2^2}{\xi_4} V_{ds} + 2V_{g1} V_{ds} - V_{ds}^2 - \left( -\frac{\xi_2^2 + 4\xi_4 V_{g1}}{6\xi_4} \left( \frac{\xi_2^2}{\xi_4} \right) \sqrt{1 + \frac{4\xi_4 V_{g1}}{\xi_2^2}} \right. \right. \\
& \left. \left. + \frac{2V_{ds}}{3} \left( \frac{\xi_2^2}{\xi_4} \right) \sqrt{1 + \frac{4\xi_4 V_{g1}}{\xi_2^2}} + \frac{\xi_2^2 + 4\xi_4 V_{g1}}{6\xi_4} \left( \frac{\xi_2^2}{\xi_4} \right) \sqrt{1 + \frac{4\xi_4 V_{g1}}{\xi_2^2}} \right] \quad (3.35)
\end{aligned}$$

$$I_{d(lin)} = \frac{\Psi}{2V_L + V_{ds}} \left( \frac{\xi_2^2}{\xi_4} V_{ds} + 2V_{g1} V_{ds} + \frac{2V_{ds}}{3} \left( \frac{\xi_2^2}{\xi_4} \right) \sqrt{1 + \frac{4\xi_4 V_{g1}}{\xi_2^2}} - V_{ds}^2 \right) \quad (3.36)$$

$$I_{d(lin)} = \frac{\Psi}{2V_L + V_{ds}} \left( V_{ds} \left[ 2V_{g1} + \frac{\xi_2^2}{\xi_4} \left( 1 - \frac{2}{3} \sqrt{1 + \frac{4\xi_4 V_{g1}}{\xi_2^2}} \right) \right] - V_{ds}^2 \right) \quad (3.37)$$

Let

$$V_{g2} = 2V_{g1} + \frac{\xi_2^2}{\xi_4} \left( 1 - \frac{2}{3} \sqrt{1 + \frac{4\xi_4 V_{g1}}{\xi_2^2}} \right) \quad (3.38)$$

$$I_{d(lin)} = \frac{\Psi(2V_{ds}V_{g2} - V_{ds}^2)}{2V_L + V_{ds}} \quad (3.39)$$

In Eq. (3.39),  $\Psi$  is given as

$$\Psi = \frac{qWv_{sat}}{\xi_4} \quad (3.40)$$

Equation (3.39) generates a family of curves when changing  $V_{ds}$  and  $V_{g2}$ . Since its operation is limited to the linear region of operation, the obtained characteristics will therefore be nothing but the characteristics of a variable resistor.

### 3.2.1.2 Saturation Point ( $V_{ds} = V_{d(sat)}$ )

The saturation point for current and voltage can be found by putting  $V_{ds} = V_{d(sat)}$  in Eqs. (3.27) and (3.39), thus



$$I_{d(sat)} = qWv_{sat}n_s \Big|_{V_{ds}=V_{d(sat)}} \quad (3.41)$$

Substituting  $n_s$  from (3.22)

$$I_{d(sat)} = \frac{qzv_{sat}\xi_4}{\xi_4} \left( \frac{-\xi_2 + \sqrt{\xi_2^2 + 4\xi_4(V_{g1} - V_{ds})}}{2\xi_4} \right)^2 \quad (3.42)$$

Let

$$\Psi = \frac{v_{sat}qz}{\xi_4} \quad (3.43)$$

$$I_{d(sat)} = \frac{\Psi}{4\xi_4} \left[ 2\xi_2^2 + 4\xi_4V_{g1} - 4\xi_4V_{d(sat)} - 2\xi_2\sqrt{\xi_2^2 + 4\xi_4V_{g1} - 4\xi_4V_{ds}} \right] \quad (3.44)$$

By using approximation  $[4\xi_4V_{ds} \ll \xi_2^2 + 4\xi_4V_{g1}]$

$$I_{d(sat)} = \frac{\Psi}{4\xi_4} \left[ 2\xi_2^2 + 4\xi_4V_{g1} - 4\xi_4V_{d(sat)} - 2\xi_2\sqrt{\xi_2^2 + 4\xi_4V_{g1}} \right] \quad (3.45)$$

$$I_{d(sat)} = \Psi \left( V_{g1} + \frac{\xi_2^2}{2\xi_4} \left[ 1 - \sqrt{1 + \frac{4\xi_4V_{g1}}{\xi_2^2}} \right] - V_{d(sat)} \right) \quad (3.46)$$

Let

$$V_{g2} = V_{g1} + \frac{\xi_2^2}{2\xi_4} \left[ 1 - \sqrt{1 + \frac{4\xi_4V_{g1}}{\xi_2^2}} \right] \quad (3.47)$$

$$I_{d(sat)} = \Psi(V_{g2} - V_{d(sat)}) \quad (3.48)$$

For saturation voltage;

$$I_{d(sat)} = \frac{\Psi[V_{d(sat)}V_{g2} - V_{d(sat)}^2]}{2V_L + V_{d(sat)}} \quad (3.49)$$

By comparing Eqs. (3.48) and (3.49)

$$\Psi[V_{g2} - V_{d(sat)}] = \frac{\Psi[V_{d(sat)}V_{g2} - V_{d(sat)}^2]}{2V_L + V_{d(sat)}} \quad (3.50)$$

So, by simple algebraic manipulation

$$V_{d(sat)} = \frac{-2V_{g2}V_L}{(V_{g2} - 2V_L)} \quad (3.51)$$

Putting the above expression in  $I_{d(sat)} = \Psi(V_{g2} - V_{d(sat)})$ , we get

$$I_{d(sat)} = \frac{\Psi V_{g2}^2}{V_{g2} - 2V_L} \quad (3.52)$$

### 3.2.1.3 Saturation Current ( $V_{ds} > V_{d(sat)}$ )

Once the saturation point is attained in the channel,  $v_d$  shifts to  $v_{sat}$ , and any further increase in  $V_{ds}$  increases associated  $E_x$  underneath the Schottky barrier; when  $E_x \approx 2E_{sat}$ , the channel length starts to shrink because of the  $y$ -directed electric field. This shrinkage is known as channel length modulation and its value is represented by  $\Delta L_g$  [125]. Under such conditions  $I_{d(sat)}$  can be found by replacing  $2V_L$  by  $(2V_L - E_{sat}\Delta L_g)$  in Eq. (3.52), thus

$$I_{d(sat)} = \frac{\Psi V_{g2}^2}{V_{g2} + (2V_L - E_{sat}\Delta L_g)} \quad (3.53)$$

To evaluate the value of  $\Delta L_g$  consider Fig. 3.5, where  $L_1$  is a region in which the carriers are traveling below saturation velocity and their velocity get saturated while they are traveling in region labeled as  $L_2$ .  $L_3$  represents the extension in depletion towards the drain side of the device where there is no gate metal. To evaluate the potential  $V$  caused by the charges accumulated inside the Schottky barrier depletion and to identify the length  $\Delta L_g$  one can apply the Poisson equation as given below [129]

$$\frac{\partial^2 V(x, y)}{\partial x^2} + \frac{\partial^2 V(x, y)}{\partial y^2} = -\frac{qN_D}{\epsilon_s} \quad (3.54)$$

where  $N_D$  represents the charge density underneath the Schottky barrier depletion. Changing the co-ordinate system as  $x' = x - L_g$

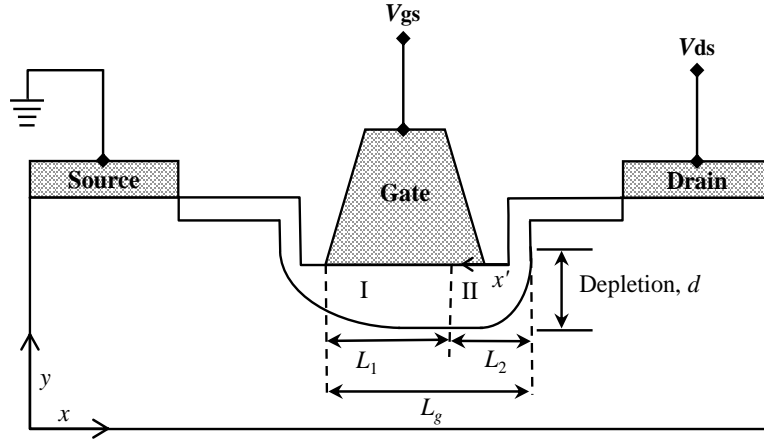


FIGURE 3.5: AlGaIn/GaN HEMT with two distinct depletion layers underneath Schottky barrier gate.

We can also define a new function as

$$S(x', y) = \chi(y) + V(x, y) \quad (3.55)$$

where

$$\frac{d^2\chi}{dy^2} = \frac{qN_D}{\epsilon_s} \quad (3.56)$$

and

$$\frac{\partial^2 S(x', y)}{\partial x'^2} + \frac{\partial^2 S(x', y)}{\partial y^2} = 0 \quad (3.57)$$

such that

$$S(x', y) = V(x, y) + \frac{qN_D}{\epsilon_s} y^2 \quad (3.58)$$

$$S(x', y) = (Ae^{kx'} + Be^{-kx'}) \times (C\cosky + D\sin ky) \quad (3.59)$$

where  $k = \sqrt{\lambda}$ .

$$S(x', y) = (Ae^{kx'} + Be^{-kx'}) (C\cosky + D\sin ky) + Ex'y + Fx' + Gy + H \quad (3.60)$$

where variables represented by the constants  $A, B, \dots, H$  can be determined by using the device boundary conditions. Assuming at  $y = 0$ , the magnitude of the

total potential shall be  $-(V_{gs} + V_{bi})$ , where  $V_{bi}$  is the built-in potential. This potential is not dependent on the variable  $x'$ , which yields  $C = 0$  and  $F = 0$ . This implies that  $H = -(V_{gs} + V_{bi})$  at  $L_1$ .

The potential at the terminating point of  $L_1$  can then be written as

$$V(L_1, y) = \frac{qN_D}{\varepsilon_s} \left[ y \left( d - \frac{y}{2} \right) \right] - (V_{gs} + V_{bi}) \quad (3.61)$$

where  $d$  is the height of depletion at length  $L_1$ .

Comparing expressions (3.60) and (3.61), we can have

$$(A + B) \times D \sin ky + Gy - (V_{gs} + V_{bi}) = \frac{qN_D y d}{\varepsilon_s} - \frac{qN_D y^2}{2\varepsilon_s} - (V_{gs} + V_{bi}) \quad (3.62)$$

this gives

$$G = \frac{qN_D d}{\varepsilon_s} \quad \text{and} \quad A = -B \quad (3.63)$$

Therefore,

$$S(x', y) = 2AD \sinh(kx') \sin ky + Ex'y + \frac{qN_D dy}{\varepsilon_s} - (V_{gs} + V_{bi}) \quad (3.64)$$

Differentiating (3.64) w.r.t  $y$

$$\left. \frac{\partial}{\partial y} S(x', y) \right|_{y=d} = 2AD \sin h(kx') k \cos kd + Ex' + \frac{qN_D d}{\varepsilon_s} \quad (3.65)$$

Considering one again (3.58) and differentiating it w.r.t  $y$ , one can write

$$\left. \frac{\partial}{\partial y} S(x', y) \right|_{y=d} = \left. \frac{\partial}{\partial y} V(x', y) \right|_{y=d} + \frac{qN_D d}{\varepsilon_s} \quad (3.66)$$

At  $y = d$

$$\frac{\partial V(x, y)}{\partial y} = 0. \quad (3.67)$$

From Eqs. (3.65) and (3.66)

$$2ADk \sinh(kx') \cos kd + Ex' + \frac{qN_D d}{\varepsilon_s} = \frac{qN_D d}{\varepsilon_s} \quad (3.68)$$

Equation (3.68) is a continuous function for  $x'$ , this requires therefore,  $E = 0$  and  $k = (\pi/2d)$ . Thus, (3.64) can be rewritten as

$$S(x', y) = 2AD \sinh\left(\frac{\pi x'}{2d}\right) \sin\left(\frac{\pi y}{2d}\right) + \frac{qN_D dy}{\varepsilon_s} - (V_{gs} + V_{bi}) \quad (3.69)$$

The field  $E$  reaches to  $E_s$  at  $x = L_g$  or  $x' = 0$ , therefore,

$$\frac{\partial}{\partial x'} S(x', y) = 2AD \cosh\left(\frac{\pi x'}{2d}\right) \times \frac{\pi}{2d} \times \sin\left(\frac{\pi y}{2d}\right) \quad (3.70)$$

$$\left. \frac{\partial S(x', y)}{\partial x'} \right|_{x'=0} = AD \frac{\pi}{d} \sin\left(\frac{\pi y}{2d}\right) \quad (3.71)$$

Equation (3.71) represents a field, which is  $E_s$ , therefore

$$E_s = -AD \frac{\pi}{d} \sin\left(\frac{\pi y}{2d}\right) \quad (3.72)$$

At  $y = d$ , the above expression is reduces to

$$AD = \frac{E_s d}{\pi} \quad (3.73)$$

Now from Eqs. (3.69), (3.73), (3.58) and at  $x' = L_1 - L_g$

$$V(x, y) = \frac{2E_s d}{\pi} \sinh\left[\frac{\pi(L_g - L_1)}{2d}\right] \sin\left(\frac{\pi y}{2d}\right) + \frac{qN_D dy}{\varepsilon_s} - \frac{qN_D y^2}{2\varepsilon_s} - (V_{gs} + V_{bi}) \quad (3.74)$$

At  $x = L_g$  and  $y = d$ , the potential variation can be written as

$$V(L_g, d) = \frac{2E_s d}{\pi} \sinh\left[\frac{\pi(L_g - L_1)}{2d}\right] + \frac{qN_D d^2}{2\varepsilon_s} - (V_{gs} + V_{bi}) \quad (3.75)$$

In Eq. (3.75), potential distribution before the saturation is represented by

$$V(L_1) = \frac{qN_D d^2}{2\varepsilon_s} - (V_{gs} + V_{bi}) \quad (3.76)$$

and

$$V(L_2) = \frac{2E_s d}{\pi} \sinh\left[\frac{\pi L_2}{2d}\right] \quad (3.77)$$

TABLE 3.1: Device dimensions and constants.

Parameter	Value
$\mu_{min}$	0.0050 m <sup>2</sup> /V.sec
$\mu_{max}$	0.2000 m <sup>2</sup> /V.sec
$n_r$	$8.2837 \times 10^{-17}$ m <sup>-2</sup>
$q$	$1.6 \times 10^{-19}$ C
$W$	100 $\mu$ m
$L_g$	0.2 $\mu$ m
$d$	0.2 $\mu$ m
$\varepsilon$	$8.86 \times 10^{-12}$ F/m
$\varepsilon_s$	9.325 $\varepsilon_0$
$\phi_{b0}$	1.6200 eV
$E_g^A$	5.0177 eV
$E_g^G$	3.5096 eV
$T_i$	300 K

Assuming  $L_2 = \Delta L_g$ ,  $V(L_2) = V_{ds} - V_{d(sat)}$  and  $E_s = E_{sat}$

$$\Delta L_g = \frac{2d}{\pi} \sinh^{-1} \left[ \frac{(V_{ds} - V_{d(sat)})\pi}{2dE_{sat}} \right] \quad (3.78)$$

### 3.3 Modeled Characteristics

To demonstrate the accuracy of the developed technique, a MATLAB code was developed using Eqs. (3.39), (3.52) and (3.53). Particle Swarm Optimization (PSO) was used to assess the simulation variables involved to predict the performance of the device. Table 3.1 presents the values of different variables, along with the physical parameters of the device used to simulate its  $I - V$  characteristics [17].

Following are the steps used to implement PSO algorithm and its details are given in [130]:

- (i) Initialize swarm dimension, velocity and position;

- (ii) Define an objective function for control;
- (iii) Update the velocity and position of each particle;
- (iv) Find the personal best position of the particle (minimum error in objective function);
- (v) Find global best position;
- (vi) Update the velocity and position with respect to personal and global best;
- (vii) Terminate if iterations are complete or if minimum error,  $E_{r(min)}$  is met, otherwise go to the step (iii).

By using Eqs. (3.39) and (3.53), the device current,  $I_{d(sim)}$ , can be calculated. This current was then compared with the experimental data,  $I_{d(exp)}$ , using an objective function given by

$$RMSE = \sqrt{\sum_{Q=1}^N \left\{ \sum_{P=1}^M \left( I_{d(exp)}^{P,Q} - I_{d(sim)}^{P,Q} \right)^2 / \sum_{P=1}^M I_{d(exp)}^{P,Q} \right\}} \leq E_{r(min)} \quad (3.79)$$

where  $P$  represents  $V_{ds}$  having its maximum value  $M$ , and  $Q$  represents  $V_{gs}$  with  $N$  as its maximum value. This function calculates the Root Mean Square Error (RMSE) of the modeled data; considering the current best location, i.e., the location with the minimum RMSE, the parameters  $\xi_{1,2,3}$  are then updated. This process continues until the obtained results are in reasonable agreement with experimental data.

In our modeling, the experimental data were fed along with the variables defined in Table 3.1 into the developed PSO code. A swarm of 100 particles with a constraint of 1000 iterations with random initial values was used. A 95% convergence rate was observed with average convergence time for the swarm of 34s. For evaluation of the temperature dependent  $n_s$ , the values of  $\xi_{1,2,3}$  and other variables optimized using PSO are presented in Table 3.2.

TABLE 3.2: Optimized model parameters at various temperatures for an Al-GaN/GaN HEMT output characteristics.

Parameter	$T = 300\text{K}$	$T = 400\text{K}$	$T = 500\text{K}$
$\xi_1$ (V)	-0.0791	-0.0768	-0.0143
$\xi_2 \times 10^{-12}$ (Vm)	0.0791	3.3808	5.2152
$\xi_3 \times 10^{-20}$ (Vm <sup>2</sup> )	0.5831	-0.5223	-0.4218
$v_{sat} \times 10^5$ (m/sec)	2.5760	2.4920	0.6683
$\phi_b(T)$ (eV)	1.6200	0.9943	0.6303
$\Delta E_c(T)$ (eV)	0.4753	0.3039	0.2250
$\theta$ (V <sup>-1</sup> )	0.0082	0.0017	0.0145
$\sigma$ (C/m <sup>2</sup> )	0.0385	0.0323	0.0337
$\lambda_1$	0.3152	0.2244	1.0585
$\lambda_2$	0.0000	1.1256	0.9113
$\lambda_3$	0.7240	0.0882	0.9085
$\lambda_4$	0.0000	0.1304	1.8514
$\beta$	0.9650	1.4596	1.6012
$\alpha$	10.096	10.471	4.4600
$\gamma$	0.0134	0.4147	2.4894

The results in Table 3.2 clearly shows that  $v_{sat}$ , which is a crucial variable for determining the characteristics of a HEMT, reduced with the increasing temperature. Considering Eq. (3.41), this clearly reminds that the saturation current of the device will reduce with increasing ambient temperature.

It is further seen from Table 3.2 that  $\phi_b(T)$ , which represents the barrier height, also reduces with increasing device operating temperature, in agreement with the expression proposed in Eq. (3.5). A reduction in the magnitude of  $\phi_b(T)$  indicates that the device may exhibit more leakage current through the Schottky barrier gate, which can potentially reduce the device transconductance [131]. Strong reduction in  $\phi_b(T)$  could completely jeopardize the device characteristics by forming a parasitic field-effect transistor (FET) through the AlGaN layer of the device.



TABLE 3.3: Gate to source voltage ( $V_{gs}$ ) dependent simulation parameters at various temperatures for an AlGaIn/GaN submicron HEMT.

Temp.	Parameter	$V_{gs} = 0V$	$V_{gs} = -1V$	$V_{gs} = -2V$	$V_{gs} = -3V$
$T = 300$ K	$n_s$ ( $10^{17} \text{ m}^{-2}$ )	1.5582	1.3137	1.0693	0.8248
	$E_F$ (V)	-0.0800	-0.0798	-0.0797	-0.0795
	$\mu_0$ ( $\text{cm}^2/\text{V}\cdot\text{sec}$ )	392	491	622	798
	$\mu_T$ ( $\text{cm}^2/\text{V}\cdot\text{sec}$ )	21.0	23.0	24.0	24.0
$T = 500$ K	$n_s$ ( $10^{17} \text{ m}^{-2}$ )	2.2528	1.9946	1.7365	–
	$E_F$ (V)	-0.0128	-0.0129	-0.0129	–
	$\mu_0$ ( $\text{cm}^2/\text{V}\cdot\text{sec}$ )	717	795	884	–
	$\mu_T$ ( $\text{cm}^2/\text{V}\cdot\text{sec}$ )	8.19	7.52	6.74	–

Table 3.2 also shows that the magnitude of  $\Delta E_c(T)$  decreases with increasing temperature, as proposed in Eq. (3.3). A reduction in  $\Delta E_c(T)$  means a corresponding reduction in  $n_s$ , thus  $\phi_b(T)$  and  $\Delta E_c(T)$  produce opposite effects on the device characteristics. Reduction in  $\phi_b(T)$  means an increase in  $I_{d(sat)}$ , because there will be more cross-sectional area available for flow of current, while on the other hand, the reduction in the magnitude of  $\Delta E_c(T)$  with increasing temperature reduces  $n_s$ , which also reduces  $I_{d(sat)}$ . Thus, these two variables are produce opposite effects, with the dominant one determining the device characteristics.

Table 3.3 shows that, at  $T = 300$  K, the value of  $n_s$  decreases as a function of  $V_{gs}$ , and the same behavior is true at  $T = 500$  K. This is in accordance with Eq. (3.22), from which it is obvious that  $n_s$  depends on  $V_{gs}$ . On the other hand, for given temperature, there is almost no change in the value of  $E_F$  when changing  $V_{gs}$ . Furthermore, a nominal change in the magnitude of  $\mu_T$  is observed on varying  $V_{gs}$ .

Examination of Table 3.3 also reveals that, when changing the temperature from  $T = 300$  K to  $T = 500$  K, there is a notable change in all four variables listed in the table, i.e.,  $n_s$ ,  $E_F$ ,  $\mu_0$ , and  $\mu_T$ . A relative increase in the magnitude of  $n_s$  at  $T = 500$  K should result in a corresponding change in  $I_{ds}$  as per Eq. (3.41), but this is not the case, as evident from Fig. 3.6. In Fig. 3.6(a), at  $V_{gs} = 0$  V and

$V_{ds} = 10$  V, the corresponding  $I_{ds}$  is 85 mA at  $T = 300$  K, and 55 mA for the same bias at  $T = 500$  K. A decrease in  $I_{ds}$  at elevated temperatures, as is seen in Fig. 3.6(b), can be associated with the decreasing values of  $\mu_T$  listed in Table 3.3. Furthermore, in Fig. 3.6(b), at  $V_{gs} = -1$  V and  $V_{gs} = -2$  V after  $V_{ds} = 12.5$  V, there is a discrepancy between the modeled and experimental characteristics. This discrepancy could be associated with the start of the impact ionization process, which is not included in the proposed model.

At elevated temperature and biasing, the carriers become energetic and they have sufficient energy to knock out other carriers from their parent positions to make them free carriers. This process of carrier multiplication continues and when a sufficient number of carriers are generated, an increase in channel current is observed as seen from Fig. 3.6(b).

The reduction in the magnitude of  $E_F$  on changing the temperature from  $T = 300$  K to  $T = 500$  K once again supports more carriers being available for conduction at  $T = 500$  K, because a location of the  $E_F$  energy level closer to the conduction band corresponds to the availability of relatively more carriers in the conduction band for subsequently release into the 2-DEG [115].

The data in Table 3.3 also show that, on changing the temperature from  $T = 300$  K to  $T = 500$  K, there is an increase in the value of  $\mu_0$  for all the chosen values of  $V_{gs}$ . This increase is a direct consequence of Eq. (3.2), wherein  $n_s$  is in the denominator and a decrease in  $n_s$  will increase  $\mu_0$ . However, if we consider the linear regions of Fig. 3.6, at both  $T = 300$  K and  $T = 500$  K, and at  $V_{gs} = 0$  V, the slope of the curves is approximately 90 and 40, respectively. This shows that, on increasing the temperature,  $\mu_T$  dominates in determining the device characteristics, as explained by Fig. 3.3. The combined effect of reduced  $\mu_T$  (Fig. 3.3) and reduced  $v_{sat}$  (Fig. 3.4) causes an increase in the resistance in the linear region of operation and thus decreases  $I_{d(sat)}$ , as is evident from Fig. 3.6. Thus, one can conclude that, at elevated temperatures the device performance is deteriorated because of degradation in the carrier mobility in the 2-DEG.

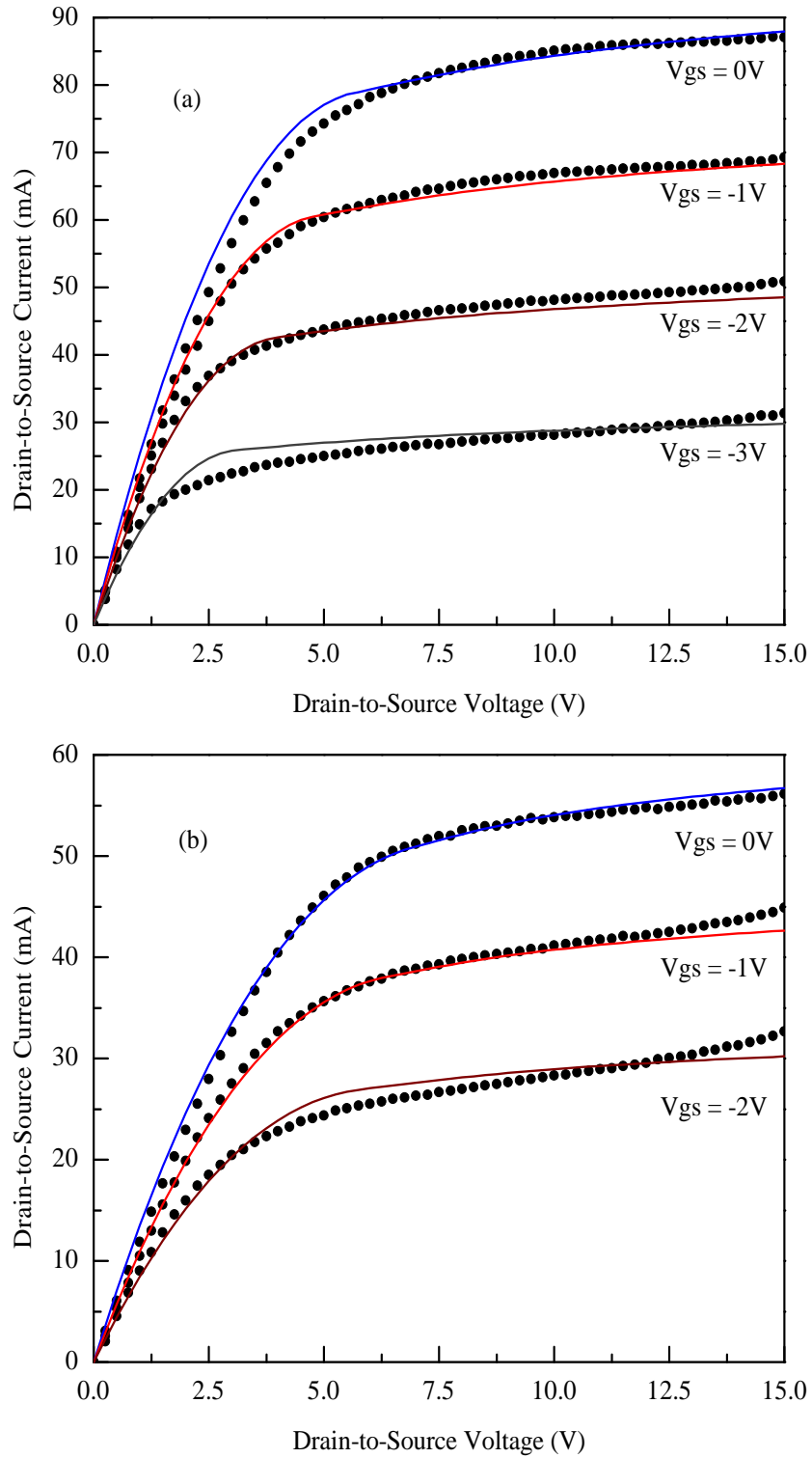


FIGURE 3.6:  $I_{ds} - V_{ds}$  characteristics of an AlGaN/GaN HEMT. Experimental data from [17] represented by ( $\bullet$ ), whereas ( $-$ ) represents characteristics by the proposed model: a) at  $T = 300$  K and b) at  $T = 500$  K.

TABLE 3.4: Comparison of various analytical models used to predict temperature dependent  $I - V$  characteristics of HEMTs.

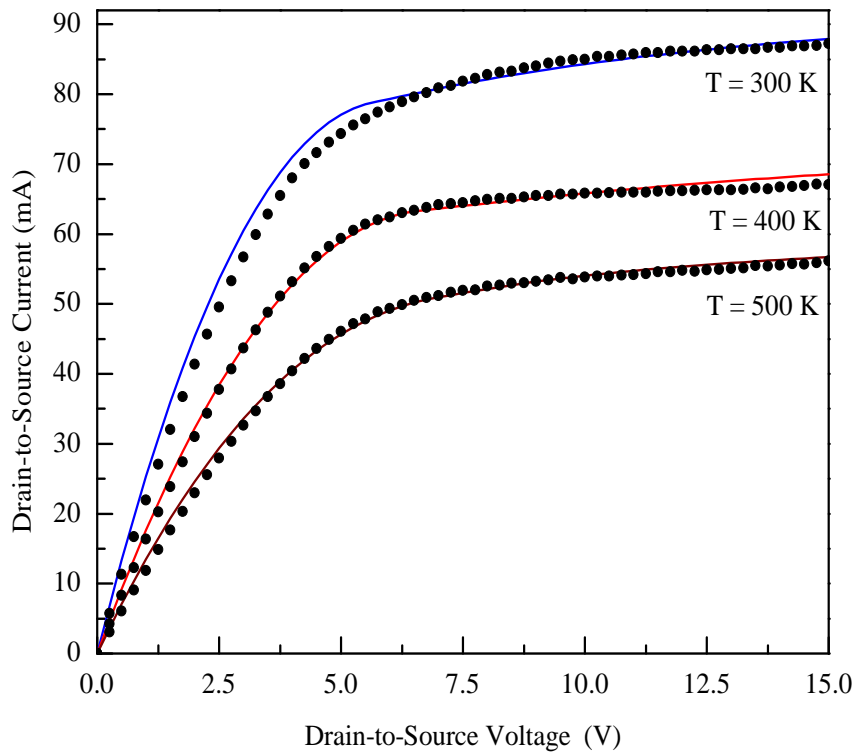
Temp.	Model	$V_{gs} = 0V$	$-1V$	$-2V$	$-3V$	Avg. RMSE
$T = 300$ K	Huque [17]	<b>0.0056</b>	<b>0.0039</b>	0.0091	0.0190	0.0222
	Wang [97]	0.0093	0.0125	0.0235	0.0575	0.0640
	Manju [22]	0.0103	0.0081	0.0132	0.0418	0.0453
	<b>Proposed</b>	0.0066	0.0040	<b>0.0060</b>	<b>0.0092</b>	<b>0.0134</b>
$T = 500$ K	Huque [17]	0.0173	0.0253	0.03061	–	0.0433
	Wang [97]	0.1062	0.0932	0.0729	–	0.1590
	Manju [22]	0.1021	0.0878	0.0645	–	0.1492
	<b>Proposed</b>	<b>0.0029</b>	<b>0.0039</b>	<b>0.0068</b>	–	<b>0.0084</b>

To compare the performance of the proposed model, in which all the four temperature dependent variables are taken into account comprehensively, with other reported models, the RMSE values at  $T = 300$  K and  $T = 500$  K were evaluated and are summarized in Table 3.4, with the lowest RSME values at given  $V_{gs}$  shown in bold. Examining the data in Table 3.4, one can clearly see that the performance of the proposed model is considerably better than that of the other reported models, at both room and elevated temperature. At  $T = 300$  K, the average RMSE attained from the Huque model [17], which is the second best model in Table 3.4, is 0.0222, whereas at  $T = 500$  K, the average RMSE of the same model is 0.0433. Comparing the performance of the proposed model with the Huque model, the observed improvement is 39.6% at  $T = 300$  K and 80% at  $T = 500$  K. These data clearly demonstrate that the performance of the proposed model is significantly better than that of other models reported in literature for prediction of the high-temperature  $I - V$  characteristics of HEMTs.

Table 3.5 presents the performance of different models at varying temperatures but at  $V_{gs} = 0$  V. Considering the average RMSE values, it is once again seen that the performance of the proposed model is better than that of other models, whereas the Huque model, as observed above, is the second best model in terms

TABLE 3.5: Comparison of RMSE of various analytical models reported in the literature for temperature dependent  $I - V$  characteristics of HEMTs.

Model	$T = 300\text{K}$	$T = 400\text{K}$	$T = 500\text{K}$	Avg. RMSE
Huque [17]	<b>0.0056</b>	0.0083	0.0173	0.0200
Wang [97]	0.0199	0.0133	0.0318	0.0398
Manju [22]	0.0186	0.0137	0.0382	0.0365
<b>Proposed</b>	0.0066	<b>0.0029</b>	<b>0.0029</b>	<b>0.0077</b>

FIGURE 3.7: Temperature dependent  $I_{ds} - V_{ds}$  characteristics of an AlGaN/GaN HEMT for  $V_{gs} = 0\text{ V}$ . Experimental data from [17] represented by ( $\bullet$ ), whereas ( $-$ ) represents characteristics by the proposed model.

of predicting the temperature-dependent  $I - V$  characteristics of AlGaN/GaN HEMTs. Comparing the error values of the proposed and Huque models, it is observed that the proposed model is 61.5% better than the Huque model. The  $I - V$  characteristics obtained for the data of Table 3.5 are shown in Fig. 3.7. This plot reveals that at,  $T = 400\text{ K}$  and  $T = 500\text{ K}$ , the curves obtained using the proposed model fit nearly perfectly, which explains why the RMSE at  $T = 400\text{ K}$  and  $T = 500\text{ K}$  of the proposed model is exceptionally low, as shown in Table 3.5.

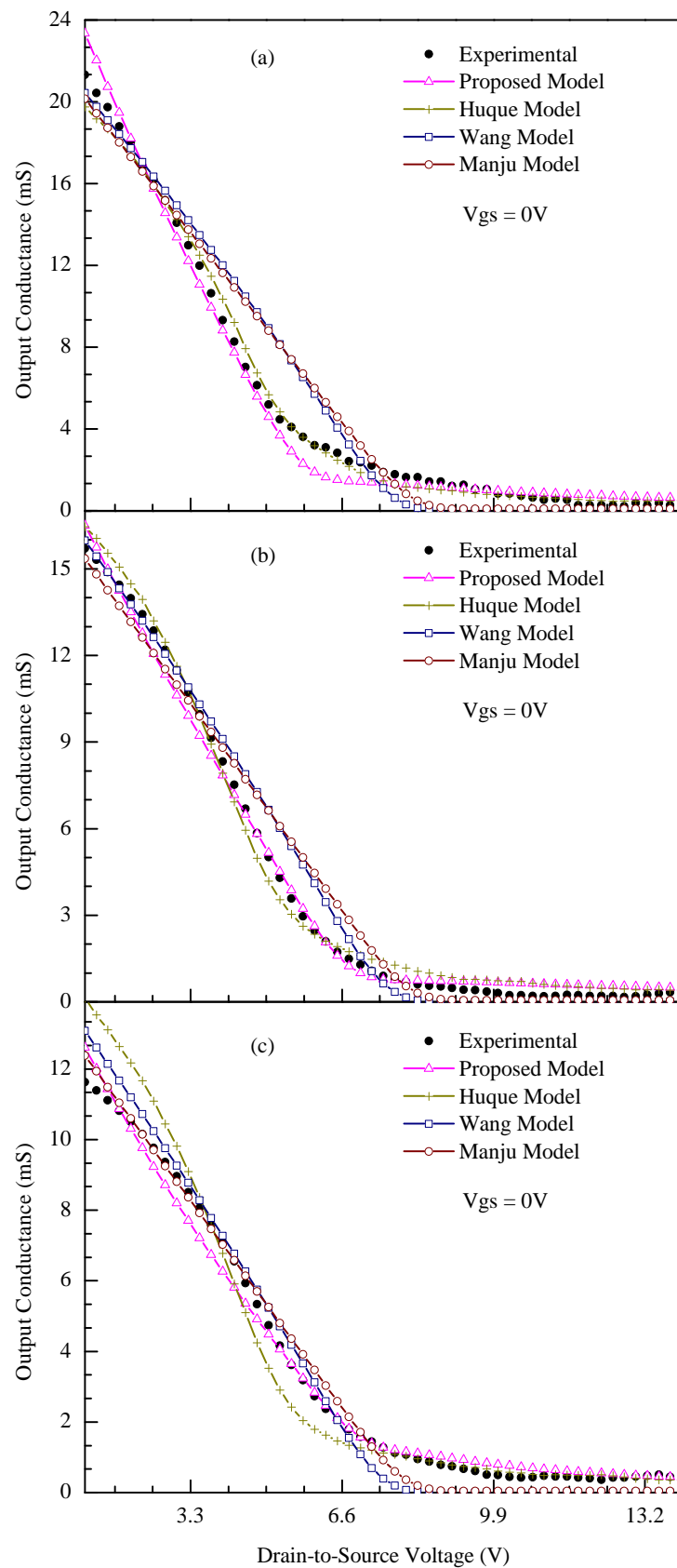


FIGURE 3.8: Output conductance of a submicron AlGaIn/GaN HEMT at: a)  $T = 300 K$ ; b)  $T = 400 K$  and c)  $T = 500 K$ . (●) represents experimental data from [17] and other symbols represent modeled output conductance.

Figure 3.8 shows the experimental and modeled output conductance ( $g_d$ ) for all four models discussed above. Figure 3.8(a) shows a plot of  $g_d$  at  $T = 300$  K, and Fig. 3.8(b) at  $T = 400$  K, whereas Fig. 3.8(c) presents the  $g_d$  of a submicron AlGaIn/GaN HEMT at  $T = 500$  K. The profile of  $g_d$  in all three cases is identical; i.e., it shows a sharp decline in the linear region of operation then saturates to almost negligible value for  $V_{ds} \geq V_{d(sat)}$ . By examining Fig. 3.8, one can observe that the maximum value of  $g_d$  occurs at  $V_{ds} = 1$  V, and it decreases with increasing temperature. This once again supports the argument that, with increasing temperature, as seen in Fig. 3.8(b,c), although  $n_s$  increases,  $g_d$  declines, suggesting that  $\mu_T$  decreases. This translates into a low value of  $g_d$  at elevated temperature. Careful examination of Fig. 3.8 also reveals that the  $g_d$  saturation point also drifts to higher  $V_{ds}$  with increasing temperature, occurring at  $V_{d(sat)} \approx 6$  V for  $T = 300$  K and  $V_{d(sat)} \approx 7$  V for  $T = 400$  K, but reaching  $V_{d(sat)} \approx 8$  V for  $T = 500$  K. Such attainment of  $v_{sat}$  at relatively higher  $V_{ds}$  values with increasing temperature indicates that a relatively high  $V_{ds}$  potential is required to achieve  $v_{sat}$ , or in other words, that at high ambient temperature the channel behaves more resistively, because of low  $\mu_T$ . Although all four models show reasonable agreement with experimental data, the proposed model, in general, offers better accuracy in all three plots in Fig. 3.8.

### 3.4 Summary

An improved model is proposed to predict the temperature dependent  $I - V$  characteristics of AlGaIn/GaN HEMTs. The proposed model incorporates the temperature-dependent variation in the Schottky barrier height,  $\phi_b(T)$ , bandgap discontinuity,  $\Delta E_c(T)$ , sheet carrier concentration of 2-DEG,  $n_s(T)$ , saturation velocity,  $v_{sat}(T)$ , and carrier mobility,  $\mu(T)$ . The swarm optimization technique was employed to determine the optimized parameter values for the model. It is demonstrated that, with increasing ambient temperature, there is a decrease in  $\phi_b$ , an increase in  $n_s$ , a decrease in the  $v_{sat}$  of 2-DEG carriers, and a decrease in  $\mu_T$ . The degradation in the  $I - V$  characteristics of AlGaIn/GaN HEMTs at elevated

temperature is accurately modeled for improved understanding, demonstrating that the deterioration in device performance is primarily associated with reduced  $\mu_T$  and  $v_{sat}$ . The proposed model was compared with other reported models intended for prediction of temperature-dependent  $I-V$  characteristics; the RMSE values indicate that the proposed model can simulate the temperature-dependent  $I-V$  characteristics with at least 39% improved accuracy. The proposed model can therefore be employed to assess the temperature-dependent reliability of HEMTs and their potential for use in harsh environments.



# Chapter 4

## HEMT Analytical Model to Assess AC Parameters

### 4.1 Introduction

GaN-based HEMT is a promising competitor for high frequency and power operations due to its relatively high saturation velocity ( $v_{sat} \sim 2.5 \times 10^7$  cm/sec) and high breakdown voltage ( $V_{Br} \sim 3.3$  MV/cm). It is also a preferred device to be employed in harsh environments because it offers a relatively wide bandgap ( $E_g \sim 3.2$  eV) [2]. Moreover, the piezoelectric and spontaneous polarization effects present in GaN HEMTs result in a high density 2-DEG at the AlGaIn/GaN hetero-interface [31]. Therefore, an AlGaIn/GaN HEMT can maintain much higher current density than other III–V group HEMTs. It is an established fact that change in temperature causes a change in the performance of the device so, an accurate knowledge of temperature dependent performance of the device is essential for its optimal use, especially in harsh environments. Different models have been developed so far to predict the temperature based performance of the device but, either they are too complex to handle or their accuracy deteriorates with increasing values of

temperature. Thus, there is a need to have a compact model capable of predicting temperature dependent performance of the device which can be employed to estimate the device performance before its fabrication.

2-DEG, which defines the sheet carrier concentration,  $n_s$  of a HEMT is affected directly by the change of ambient temperature. As the temperature increases, the generation of  $n_s$  also increases [116], which effectively controls the channel current and thus, the device performance. So, an accurate charge control model to assess  $n_s$  is needed, which incorporates all the temperature dependent physical parameters of the device, such as; Schottky barrier height of the gate, relative position of Fermi level and discontinuity of conduction band at the interface of AlGa<sub>N</sub> and GaN layers.

The change in ambient temperature along with high bias affects the device channel conditions and as a result, there is a considerable rise in the channel temperature which modifies the device characteristics [132]. These effects are frequently observed in submicron devices where the field underneath Schottky barrier reaches  $\sim 10^6 \text{cm}^{-1}$  [133]. Thus, channel heating effects are more pronounced for the devices having smaller dimensions but with relatively high drain current to meet specific power requirements. This necessitates a model of closed form expressions to assess channel temperature with reasonable accuracy by using the ambient and bias conditions of the device.

Chattopadhyay et al. in 2008 proposed a model for temperature dependent DC characteristics of AlGa<sub>N</sub>/GaN HEMT [22]. In their model, they incorporated self heating effect on the device output characteristics. They successfully modeled the negative resistance of the device characteristics after the onset of saturation; however, they did not demonstrate the validity of their model above room temperature. Thus, the effect of ambient temperature on the modeled characteristics needs to be validated. Moreover, in their model, they assumed Schottky barrier height of the device as temperature independent; thus, there could be a possibility that the model might not predict the device characteristics with an acceptable accuracy at elevated temperatures.

Wang et al. in 2013 also proposed a temperature dependent model for AlGa<sub>N</sub>/Ga<sub>N</sub> HEMT devices [97]. In their model, they identified temperature dependent parameters, which influence the device characteristics. They observed that Schottky barrier height, threshold voltage, bandgap discontinuity, mobility and  $n_s$ , have a strong impact in defining the device temperature dependent characteristics. They developed an analytical model to predict  $I - V$  characteristics as a function of temperature. However, their  $I - V$  model does not incorporate the negative conductance in the saturation region of operation. As a result, their model's accuracy deteriorates after the onset of saturation. Moreover, Wang model does not speak at all about the AC performance of the device as a function of temperature. Therefore, a model which can predict DC/AC temperature dependent performance of the device would be a useful tool for the design engineers.

M. Alim et al. in 2016 reported temperature dependent characterization of Ga<sub>N</sub> HEMTs of submicron dimensions and showed varying response of the device DC and AC characteristics as a function of ambient temperature [23]. They showed that power handling capability of the device declines with increasing magnitude of ambient temperature. They also demonstrated that AC performance of the device is sensitive to the ambient temperature. Their modeled temperature dependent intrinsic AC parameters, in general, followed the experimental data but with poor accuracy.

In this work, we have developed a technique, which can predict temperature dependent AC parameters of submicron Ga<sub>N</sub> HEMTs using DC characteristics. In the proposed technique, once a good degree of accuracy is achieved between the modeled and the observed DC characteristics, the technique is then extended to predict the device AC small signal parameters. To establish the validity of the proposed technique temperature dependent small signal AC parameters of submicron Ga<sub>N</sub> HEMT are assessed and compared with the device experimental data. It has been shown that the proposed technique offers relatively better accuracy than Alim model. The remaining composition of the chapter is as follows: Section 4.2 describes the evaluation of HEMT fundamental parameters to be used in temperature dependent modeling. Followed by DC model expressions involving both

for the linear and the saturation region of operation. This section also presents evaluation of AC small signal parameters using the device DC characteristics. In Section 4.3, results obtained from the model and their comparison with experimental data are discussed. In the end, conclusions drawn from this research are presented.

## 4.2 Model Development

Analytical models are preferred because they are useful in providing good insight about the device characteristics. They can be successfully deployed to predict the behavior of the device under varying conditions. This includes the device design and fabrication parameters as well as the ambient conditions in which the device is ought to be operated. Ambient temperature coupled with self-heating caused by the device bias voltages, collectively raise the channel temperature thus, affecting the overall performance of the device. The device operating temperature is therefore considered a crucial parameter in determining the overall performance of the device. Temperature based device testing is not always possible, so a temperature dependent model allows the flexibility of having an alternative. It is therefore, important that such a model, on one hand, should be a reliable one and on the other hand, easy to handle with.

Contrary to the conventional HEMTs where a doped layer is required to release the carriers for 2-DEG; in AlGa<sub>N</sub>/Ga<sub>N</sub> HEMTs, 2-DEG can be achieved under piezoelectric effect when a discontinuity is generated by AlGa<sub>N</sub>/Ga<sub>N</sub> heterojunction, as shown in Fig. 1.4. Threshold voltage,  $V_{th}$  of such a system can be expressed as [125]

$$V_{th} = \phi_b(T) - \Delta E_c(T) - \frac{\sigma d}{\epsilon_s} \quad (4.1)$$

where  $\phi_b(T)$  and  $\Delta E_c(T)$  are the temperature dependent Schottky barrier height and bandgap discontinuity, respectively [134],  $d$  is the height of undoped AlGa<sub>N</sub> layer shown in Fig. 1.4,  $\sigma$  represents piezoelectric polarization at heterojunction

interface and  $\varepsilon_s$  is the semiconductor's permittivity. Voltage  $V_{th}$  plays an important role in defining  $n_s$ , which can be expressed as [17, 135]

$$n_s = \frac{\varepsilon_s}{qd} [V_{gs} - V_{th} - E_F - V(x)] \quad (4.2)$$

where  $q$  is the charge on a single electron,  $V_{gs}$  is gate to source voltage and  $V(x)$  represents channel potential at any location  $x$ . Fermi energy,  $E_F$  of Eq. (4.2) has a dependence on  $n_s$  and is defined as  $E_F = k_1 + k_2 n_s^{1/2} + k_3 n_s$ , where  $k_s$  are constants which are to be evaluated and they depend on heterojunction interface [17, 36]. For an AlGaIn/GaN heterojunction, the following definition of  $E_F$  has been proposed

$$E_F = \xi n_s^{1/2} \quad (4.3)$$

where,  $\xi$  is a temperature dependent constant with units Vm. This proposed modification will simplify all subsequent expressions involving  $n_s$ . Equations (4.2) and (4.3) can be combined to get a quadratic expression for  $n_s$

$$n_s = \frac{\varepsilon_s}{qd} (V_{gs} - V_{th} - V_x - \xi n_s^{1/2}) \quad (4.4)$$

$$n_s = \frac{\varepsilon_s}{qd} (V_{gs} - V_{th} - V_x) - \frac{\varepsilon_s \xi n_s^{1/2}}{qd} \quad (4.5)$$

$$n_s + \frac{\varepsilon_s \xi n_s^{1/2}}{qd} - \frac{\varepsilon_s}{qd} (V_{gs} - V_{th} - V_x) = 0 \quad (4.6)$$

$$n_s + p \xi n_s^{1/2} - p (V_{gs} - V_{th} - V_x) = 0 \quad (4.7)$$

where

$$p = \frac{\varepsilon_s}{qd} \quad (4.8)$$

Suppose  $V_{g1} = V_{gs} - V_{th}$ . Therefore,

$$n_s^{\frac{1}{2}} = \left[ \frac{\sqrt{p^2\xi^2 + 4p(V_{g1} - V_x)} - p\xi}{2} \right] \quad (4.9)$$

$$n_s = \left[ \frac{\sqrt{p^2\xi^2 + 4p[V_{g1} - V(x)]} - p\xi}{2} \right]^2 \quad (4.10)$$

### 4.2.1 DC Characteristics

The first and the initial response while evaluating the electrical quality of an HEMT is determined through its DC characteristics. HEMT output characteristics have two distinct regions: a) linear region and b) saturation region of operation. In the linear region 2-DEG carriers travel with the velocity,  $v_d(x)$ , which is less than saturation velocity,  $v_{sat}$ , and the linear region current,  $I_{d(lin)}$  for the applied drain to source potential,  $V_{ds}$  can be written as [134]

$$I_{d(lin)} = \frac{2\xi\Psi}{2V_L + V_{ds}} \int_0^{V_{ds}} n_s dV \quad (4.11)$$

Making the substitution for  $n_s$  from Eq. (4.10) and by using the approximation  $4pV(x) \ll p^2\xi^2 + 4pV_{g1}$  we obtained

$$I_{d(lin)} = \frac{\Psi(2V_{ds}V_{g2} - V_{ds}^2)}{2V_L + V_{ds}} \quad (4.12)$$

where  $\Psi = pqWv_{sat}$  and  $V_L = L_gE_{sat}$ . Variable  $W$  defines the width,  $L_g$  is the gate length of the device and  $E_{sat}$  represents the field where carriers velocity saturates. Moreover, voltage  $V_{g2}$  is defined as

$$V_{g2} = V_{g1} + \frac{p\xi^2}{2} \left( 1 - \sqrt{1 + \frac{4V_{g1}}{p\xi^2}} \right) \quad (4.13)$$

The applied drain voltage point, after which the current saturates, defines the beginning of the saturation region; beyond that, minimal or no change in the output current is observed. At this point,  $V_{ds}$  attains  $V_{d(sat)}$  and  $v_d(x) = v_{sat}$ . So

by substituting these conditions we get [134]

$$V_{d(sat)} = \frac{2V_{g2}V_L}{V_{g2} + 2V_L} \quad (4.14)$$

and

$$I_{d(sat)} = \frac{\Psi V_{g2}^2}{V_{g2} + 2V_L} \quad (4.15)$$

Once the saturation has occurred,  $V_L$  reduces due to the reduction of the channel length, referred to as channel length modulation,  $\Delta L_g$  and under such conditions Eq. (4.15) becomes

$$I_{d(sat)} = \frac{\Psi V_{g2}^2}{V_{g2} + (2V_L - E_{sat}\Delta L_g)} \quad (4.16)$$

By applying two-dimensional Poisson's equation on Schottky barrier depletion of a HEMT, and solving it with appropriate boundary conditions [136], we get the value of  $\Delta L_g$  as given in Eq. (3.78)

$$\Delta L_g = \frac{2d_{sat}}{\pi} \times \sinh^{-1} \left( \frac{(V_{ds} - V_{d(sat)})\pi}{4dE_{sat}} \right) \quad (4.17)$$

where  $d_{sat}$  defines the height of depletion after the onset of current saturation. It can be found by using the same technique as given in [22]. Considering Eq. (4.10) once again and open its square

$$n_s = \frac{4p(V_{g1} - V(x)) + 2p^2\xi^2 - 2p\xi\sqrt{p^2\xi^2 + 4p(V_{g1} - V(x))}}{4} \quad (4.18)$$

$$n_s = \frac{4p(V_{g1} - V(x)) + 2p^2\xi^2 \left( 1 - \sqrt{1 + \frac{4}{p\xi^2}(V_{g1} - V(x))} \right)}{4} \quad (4.19)$$

$$n_s = \frac{4p(V_{g1} - V(x)) + 2p^2\xi^2 \left(1 - \sqrt{1 + \frac{4}{p\xi^2}(V_{g1} - V(x))}\right)}{4} \quad (4.20)$$

$$\times \frac{\left(1 + \sqrt{1 + \frac{4}{p\xi^2}(V_{g1} - V(x))}\right)}{\left(1 + \sqrt{1 + \frac{4}{p\xi^2}(V_{g1} - V(x))}\right)}$$

After simplification, we get

$$n_s = \frac{4p(V_{g1} - V(x)) \left(1 + \sqrt{1 + \frac{4}{p\xi^2}(V_{g1} - V(x))}\right) - 8p(V_{g1} - V(x))}{4 \left(1 + \sqrt{1 + \frac{4}{p\xi^2}(V_{g1} - V(x))}\right)} \quad (4.21)$$

$$n_s = \frac{4p(V_{g1} - V(x)) \left(1 + \sqrt{1 + \frac{4}{p\xi^2}(V_{g1} - V(x))} - 2\right)}{4 \left(1 + \sqrt{1 + \frac{4}{p\xi^2}(V_{g1} - V(x))}\right)} \quad (4.22)$$

$$n_s = \frac{p(V_{g1} - V(x)) \left(-1 + \sqrt{1 + \frac{4}{p\xi^2}(V_{g1} - V(x))}\right)}{\left(1 + \sqrt{1 + \frac{4}{p\xi^2}(V_{g1} - V(x))}\right)} \quad (4.23)$$

$$n_s = \frac{p(V_{g1} - V(x))}{\left(1 + \sqrt{1 + \frac{4}{p\xi^2}(V_{g1} - V(x))}\right)} \left[ \frac{1}{\left(-1 + \sqrt{1 + \frac{4}{p\xi^2}(V_{g1} - V(x))}\right)^{-1}} \right] \quad (4.24)$$

$$n_s = \frac{p(V_{g1} - V(x))}{\left(1 + \sqrt{1 + \frac{4}{p\xi^2}(V_{g1} - V(x))}\right)} \left( \frac{p\xi}{-p\xi + \sqrt{p^2\xi^2 + 4p(V_{g1} - V(x))}} \right) \quad (4.25)$$



$$n_s = \frac{p(V_{g1} - V(x))}{\left(1 + \sqrt{1 + \frac{4}{p\xi^2}(V_{g1} - V(x))}\right) \left(\frac{p\xi}{-p\xi + \sqrt{p^2\xi^2 + 4p(V_{g1} - V(x))}}\right)} \quad (4.26)$$

$$\times \frac{1}{\left(\frac{p\xi + \sqrt{p^2\xi^2 + 4p(V_{g1} - V(x))}}{p\xi + \sqrt{p^2\xi^2 + 4p(V_{g1} - V(x))}}\right)}$$

$$n_s = \frac{p(V_{g1} - V(x))}{\left(1 + \sqrt{1 + \frac{4}{p\xi^2}(V_{g1} - V(x))}\right) \left(\frac{p\xi (p\xi + \sqrt{p^2\xi^2 + 4p(V_{g1} - V(x))})}{-p^2\xi^2 + p^2\xi^2 + 4p(V_{g1} - V(x))}\right)} \quad (4.27)$$

$$n_s = \frac{p(V_{g1} - V(x))}{\left(1 + \sqrt{1 + \frac{4}{p\xi^2}(V_{g1} - V(x))}\right) \left[\frac{p^2\xi^2 \left(1 + \sqrt{1 + \frac{4}{p\xi^2}(V_{g1} - V(x))}\right)}{4p(V_{g1} - V(x))}\right]} \quad (4.28)$$

$$n_s = \frac{p(V_{g1} - V(x))}{\frac{p^2\xi^2}{4p(V_{g1} - V(x))} \left[1 + 1 + \frac{4}{p\xi^2}(V_{g1} - V(x)) + 2 \left(1 + \sqrt{1 + \frac{4}{p\xi^2}(V_{g1} - V(x))}\right)\right]} \quad (4.29)$$

$$n_s = \frac{p(V_{g1} - V(x))}{\frac{p^2\xi^2}{2p(V_{g1} - V(x))} \left[1 + \frac{2}{p\xi^2}(V_{g1} - V(x)) + \left(1 + \sqrt{1 + \frac{4}{p\xi^2}(V_{g1} - V(x))}\right)\right]} \quad (4.30)$$

$$n_s = \frac{p(V_{g1} - V(x))}{\frac{p^2\xi^2}{2(V_{g1} - V(x))} + 1 + \frac{p^2\xi^2}{2(V_{g1} - V(x))} \left(1 + \sqrt{1 + \frac{4}{p\xi^2}(V_{g1} - V(x))}\right)} \quad (4.31)$$

$$n_s = \frac{p(V_{g1} - V(x))}{1 + \left[ \frac{p^2\xi^2}{2(V_{g1} - V(x))} \left(1 + \sqrt{1 + \frac{4}{p\xi^2}(V_{g1} - V(x))}\right) \right]} \quad (4.32)$$

By putting  $p = \varepsilon/qd$  in above equation, we get

$$n_s = \frac{\varepsilon(V_{g1} - V(x))}{qd \left\{ 1 + \left[ \frac{p^2\xi^2}{2(V_{g1} - V(x))} \left(1 + \sqrt{1 + \frac{4}{p\xi^2}(V_{g1} - V(x))}\right) \right] \right\}} \quad (4.33)$$

The 2-DEG charge at saturation point is a product of capacitance and voltage across it, then we have

$$qn_s = \frac{\varepsilon}{d_{sat}}(V_{g1} - V(x)) \quad (4.34)$$

By comparing Eqs. (4.33) and (4.34), and substituting  $V(x) = V_{d(sat)}$  we get

$$d_{sat} = d \left\{ 1 + \left[ \frac{p^2\xi^2}{2(V_{g1} - V_{d(sat)})} \left(1 + \sqrt{1 + \frac{4}{p\xi^2}(V_{g1} - V_{d(sat)})}\right) \right] \right\} \quad (4.35)$$

As current in the channel increases, the temperature of the channel also rises. The total dissipated power,  $P_{dis}$  of the device depends upon the applied voltage and the current delivered by the device. This can be written in the form of current voltage product as  $P_{dis} = I_d V_{ds}$ .

The temperature of the substrate,  $T_{sub}$  depends upon the reference temperature,  $T_r$  and  $P_{dis}$  and it can be expressed as [22]

$$T_{sub} = T_r + \lambda_c P_{dis} \quad (4.36)$$

where  $\lambda_c$  represents the heat conduction coefficient of the package of an AlGaIn/GaN HEMT. The resistance of the channel can be written as [137]

$$R_{th} = \frac{1}{\pi\kappa} \ln \left[ \frac{8T_{sub}}{\pi L_g} \right] \quad (4.37)$$

where,  $\kappa$  is the thermal conductivity. The rise in the channel temperature,  $T_{ch}$  is given by

$$T_{ch} = R_{th}P_{dis} + T_{sub} \quad (4.38)$$

For the submicron channel, it has been assumed that the temperature has a nonlinear effect on the resistance of the channel which can be simulated by an exponential expression as

$$R_{ch} = R_{th} \left[ 1 + \lambda_2 \text{Exp} \left( 1 - \frac{T_r}{2T_{ch}} \right) \right] \quad (4.39)$$

where,  $\lambda_2$  is a fitting parameter. So, the temperature dependent drain to source current,  $I_{dT}$  can be expressed as

$$I_{dT} = I_d - I_d \left( 1 - \frac{R_{th}}{R_{ch}} \right) \quad (4.40)$$

It can be seen from Eq. (4.40), that an increase in temperature increases  $R_{ch}$  and as a consequence,  $I_{dT}$  decreases. Now the dissipated power can be rewritten as

$$P_{dis} = I_{dT}V_{ds} \quad (4.41)$$

## 4.2.2 AC Characteristics

The equivalent model of an AlGaIn/GaN HEMT can be expressed as Fig. 4.1.  $L_g$ ,  $L_d$  and  $L_s$  represent gate, drain and source inductances, respectively,  $C_{pg}$  and  $C_{pd}$  are gate and drain pad capacitors whereas,  $R_g$ ,  $R_d$  and  $R_s$  are gate, drain and source resistors, respectively. These components collectively define the extrinsic part of the circuit and are dependent upon the technology used for the device fabrication.

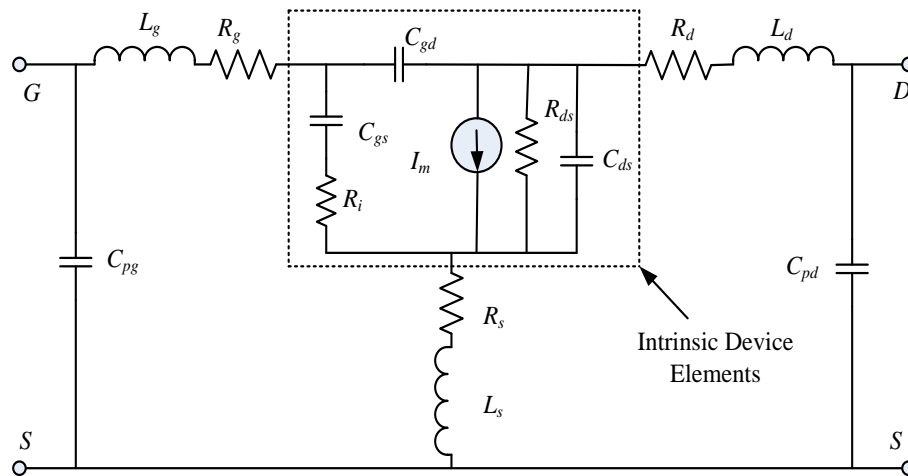


FIGURE 4.1: AC equivalent model of an AlGaIn/GaN HEMT.

On the other hand, the components shown inside the dotted line of Fig. 4.1 represent the device intrinsic parameters which play a crucial role in determining the device AC response. Gate to drain capacitor,  $C_{gd}$ , gate to source capacitor,  $C_{gs}$  and drain to source capacitor  $C_{ds}$  represent Miller capacitors of the device. The current flow in 2-DEG can be represented by a current dependent source,  $I_m$  and resistor  $R_{ds}$  can be written as the inverse of output conductance,  $g_d$  having definition [20, 21]

$$g_d = \frac{d}{dV_{ds}} [I_d] \quad (4.42)$$

Using the value of  $I_d$  in Eq. (4.42) as defined by Eqs. (4.12) and (4.15), one can evaluate the magnitude of  $g_d$  as a function of  $V_{ds}$  keeping  $V_{gs}$  constant. Transconductance,  $g_m$  of a HEMT depends upon the input swing of  $V_{gs}$  at a given  $V_{ds}$  and can simply be written as

$$g_m = \frac{d}{dV_{gs}} [I_d] \quad (4.43)$$

Once again,  $g_m$  for the linear or the saturation region of operation can be known by using the respective equation of  $I_d$  in Eq. (4.43). Intrinsic transconductance,  $g_{m0}$  as a function of  $g_m$  and  $R_s$  can be expressed as [23]

$$g_{m0} = \frac{g_m}{1 - g_m R_s} \quad (4.44)$$

The input channel resistance for AC current,  $R_i$  can be approximated as [133]

$$R_i \approx \frac{v_{sat}L_g}{\mu_T I_d} \quad (4.45)$$

where  $\mu_T$  is temperature dependent mobility given by [134]

$$\mu_T = \mu(V)[1 - \lambda_3(\Delta T/T_f)]^\gamma \quad (4.46)$$

In above expression  $\mu(V)$  represents voltage dependent mobility,  $\Delta T = T_f - T_i$  is the difference between final and initial temperatures,  $\lambda_3$  and  $\gamma$  are optimization variables, respectively. By assuming circular depletion underneath Schottky barrier gate, because of submicron gate length,  $C_{ds}$  can be approximated as

$$C_{ds} \approx \frac{4\pi\epsilon_s W d_{sat}}{(L_g + \Delta L_g)/4} \quad (4.47)$$

To calculate  $C_{gd}$ , the charge responsible in defining  $C_{gd}$  is required to be calculated. And if we assume that the voltage drop across the channel is symmetrical and 1/2 of the  $V_{ds}$  causes depletion definition towards the drain side of the gate then we can write

$$Q_{T(gd)} \approx qdW \int_0^{V_{ds}/2} n_s dV \quad (4.48)$$

Substituting the value of  $n_s$  from Eq. (4.10) and integrating the expression we get

$$Q_{T(gd)} \approx qdW \left[ \frac{\xi(\xi^2 p^2 - 4p(V_{ds}/2 - V_{g1})^{3/2})}{12} - \frac{p(V_{ds}/2 - V_{g1})^2}{2} + \frac{V_{ds}\xi^2 p^2}{4} - \frac{\xi(\xi^2 p^2 + 4pV_{g1}^{3/2})}{12} - \frac{pV_{g1}^2}{2} \right] \quad (4.49)$$

From Eq. (4.49), it is obvious that  $C_{gd}$  should be sensitive to both the voltages, i.e.  $V_{ds}$  and  $V_{gs}$  and the effects of both can be seen independently by differentiating Eq. (4.49) with respect to both the applied potentials, therefore,

$$C_{gd} = \frac{d}{dV_{ds}} [Q_{T(gd)}] \quad \text{also} \quad C_{gd} = \frac{d}{dV_{gs}} [Q_{T(gd)}] \quad (4.50)$$

According to the basic definition of capacitance per unit area, one can write  $C_{gd1} =$

$\epsilon_s/d_{sat}$ , and by assuming that the depletion height variation because of  $V_{ds}$  towards the source-side of the gate relative to the drain-side is such that  $d_1 \approx d_{sat}/2$  thus,

$$C_{gs} \approx \frac{Q_{T(gd)}}{2V} \quad (4.51)$$

This leads to the accumulation of charge towards the source side of depletion of an HEMT as a function of applied potential as

$$Q_{T(gs)} \approx qdW \int_0^{2V_{ds}} n_s dV \quad (4.52)$$

So, by substituting the value of  $n_s$  from Eq. (4.10) and by integrating the above expression we get

$$Q_{T(gs)} \approx qdW \left[ \frac{\xi(\xi^2 p^2 - 4p(2V_{ds} - V_{g1})^{3/2})}{12} - \frac{p(2V_{ds} - V_{g1})^2}{2} + V_{ds}\xi^2 p^2 - \frac{\xi(\xi^2 p^2 + 4pV_{g1}^{3/2})}{12} - \frac{pV_{g1}^2}{2} \right] \quad (4.53)$$

Again from Eq. (4.53), it is obvious that  $C_{gs}$  should be sensitive to both voltages, i.e.  $V_{ds}$  and  $V_{gs}$ , thus

$$C_{gs} = \frac{d}{dV_{ds}} [Q_{T(gs)}] \quad \text{also} \quad C_{gs} = \frac{d}{dV_{gs}} [Q_{T(gs)}] \quad (4.54)$$

Figure 4.2(a) shows variation in  $C_{gs}$  and  $C_{gd}$  as a function of  $V_{ds}$  while Fig. 4.2(b) represents changing profile of  $C_{gs}$  and  $C_{gd}$  with respect to  $V_{gs}$ . It is obvious that increasing  $V_{ds}$  would cause more and more tapering of the gate depletion, resulting into the reduction in  $C_{gs}$  and  $C_{gd}$  as evident from Fig. 4.2(a). Since the tapering in the gate depletion would be maximum at the drain side of the gate therefore, the magnitude of  $C_{gs}$  would be considerably higher than  $C_{gd}$ . Both the plots of Fig. 4.2 show that  $C_{gs} \approx 12 \times C_{gd}$ . From Fig. 4.2(a), it is obvious that by increasing  $V_{ds}$  the magnitudes of Miller capacitors are decreasing while from Fig. 4.2(b) it can be seen that by increasing  $V_{gs}$ , for a given value of  $V_{ds}$ , the magnitudes of Miller capacitors are increasing. In the preceding case the decrease in Miller capacitors can be associated with the increased magnitude of gate depletion as a function of

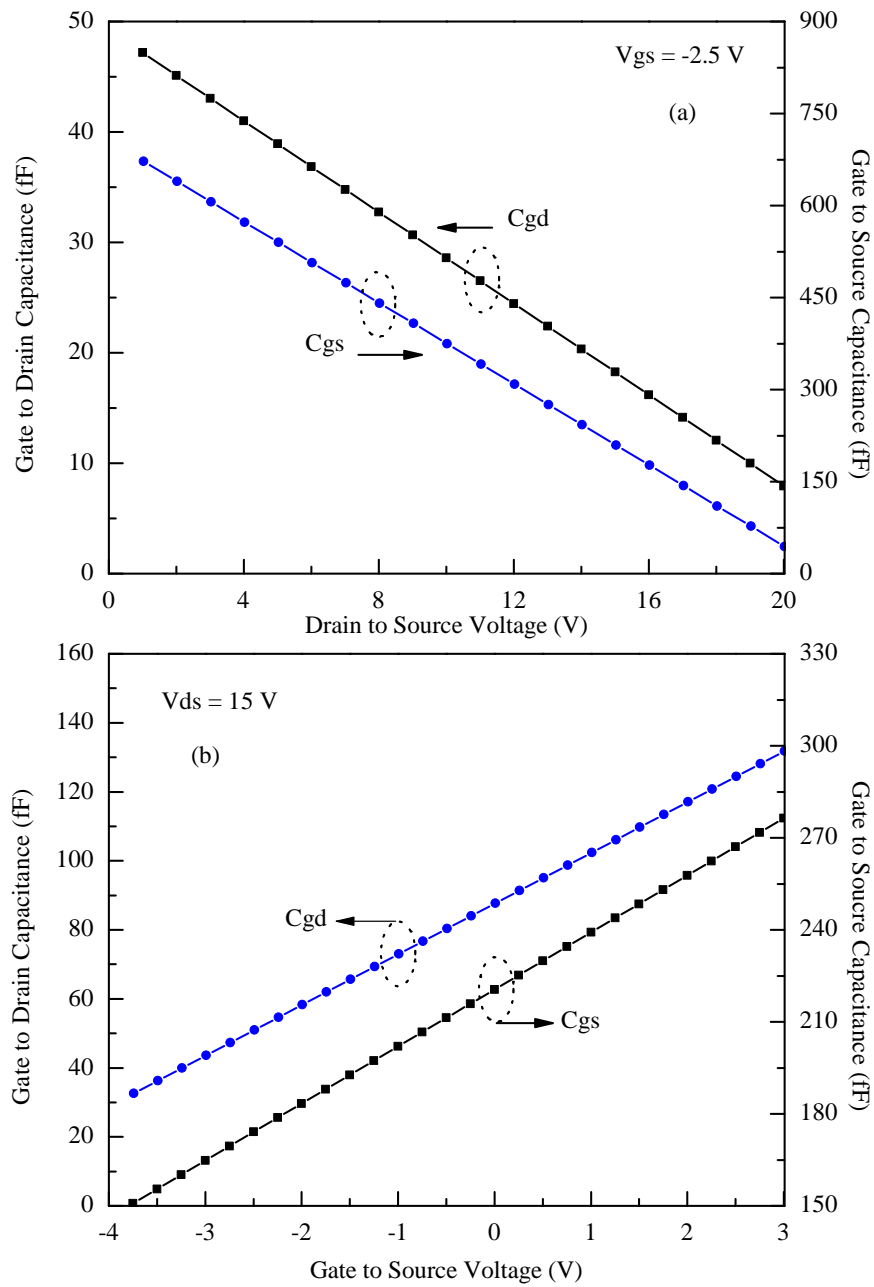


FIGURE 4.2: Modeled variation in gate to source and gate to drain capacitances as a function of (a)  $V_{ds}$  and (b)  $V_{gs}$  for an AlGaIn/GaN HEMT.

applied  $V_{ds}$  while in the latter case, it is the reduction in the gate depletion as a function of  $V_{gs}$ , which causes an increase in the magnitude of Miller capacitors of the device.

The transient time,  $\tau$  depends upon the charging and discharging of  $C_{gs}$  and  $C_{gd}$ , and can be written as [136]

$$\tau \approx \frac{(C_{gs} + C_{gd})}{g_m} \quad (4.55)$$

Equation (4.55) leads to the definition of unity gain frequency,  $f_T$  as

$$f_T = \frac{g_m}{2\pi(C_{gs} + C_{gd})} \quad (4.56)$$

Using the intrinsic small signal parameters calculated hitherto, Y-parameters can be estimated by employing a simple two port network as shown below [138]

$$Y = \begin{bmatrix} \frac{j\omega C_{gs}}{1 + j\omega R_i C_{gs}} + j\omega C_{gd} & -j\omega C_{gd} \\ \frac{g_m e^{-j\omega t}}{1 + j\omega R_i C_{gs} - j\omega C_{gd}} & g_{ds} - j\omega(C_{ds} + C_{gd}) \end{bmatrix} \quad (4.57)$$

where,  $\omega$  is the frequency in radians. Y-parameters are converted into S-parameters using [139]

$$S_{11} = \frac{(1 - Z_0 Y_{11})(1 + Z_0 Y_{22}) + Z_0^2 Y_{12} Y_{21}}{\Delta Y} \quad (4.58)$$

$$S_{12} = \frac{-2Z_0 Y_{12}}{\Delta Y} \quad (4.59)$$

$$S_{21} = \frac{-2Z_0 Y_{21}}{\Delta Y} \quad (4.60)$$

$$S_{22} = \frac{(1 + Z_0 Y_{11})(1 - Z_0 Y_{22}) + Z_0^2 Y_{12} Y_{21}}{\Delta Y} \quad (4.61)$$



where  $Z_0$  is the characteristic impedance and

$$\Delta Y = (1 + Z_0 Y_{11})(1 + Z_0 Y_{22}) - Z_0^2 Y_{12} Y_{21} \quad (4.62)$$

In summary, DC temperature dependent model discussed in Section 4.1 will be first employed to model  $I - V$  characteristics of a GaN HEMT. Once a good agreement is achieved then AC intrinsic small signal parameters will be calculated as discussed in Section 4.2 which will then lead to the prediction of S-parameters of the device. Thus, by knowing the DC temperature dependent characteristics the technique will enable to assess AC small signal parameters of GaN based HEMTs.

### 4.3 Result and Discussion

In this research, self-heating and the ambient temperature effects on the characteristics of AlGaIn/GaN HEMTs have been modeled, followed by the temperature dependent DC and AC response of the device. A MATLAB simulator has been developed involving Eqs. (4.12), (4.14) and (4.16) to calculate the DC characteristics of the device. Optimized values of fitting parameters are achieved by employing Particle Swarm Optimization (PSO) technique wherein, 1000 iterations are used with the swarm size of 50, and a convergence rate of over 90% is observed [106]. For convergence purposes, the algorithm used a cost function defined in Eq. (4.63)

$$\text{RMSE} = \sqrt{\sum_{Q=1}^N \left\{ \sum_{P=1}^M \left( I_{d(\text{exp})}^{P,Q} - I_{d(\text{sim})}^{P,Q} \right)^2 / \sum_{P=1}^M I_{d(\text{exp})}^{P,Q} \right\}} \leq E_{r(\text{min})} \quad (4.63)$$

In Eq. (4.63),  $E_{r(\text{min})}$  represents minimum error tolerance,  $I_{d(\text{exp})}$  and  $I_{d(\text{sim})}$  are the experimental and the simulated currents, respectively. Variables  $P$  and  $Q$  are the applied  $V_{gs}$  and  $V_{ds}$  having maximum value  $M$  and  $N$ , respectively.

In Fig. 4.3, a family of  $I - V$  curves is plotted for a  $0.15 \mu\text{m} \times 200 \mu\text{m}$  device [23] at different ambient temperatures ranging from 233 K to 423 K. In the figure, symbols represent the experimental data whilst the modeled characteristics are

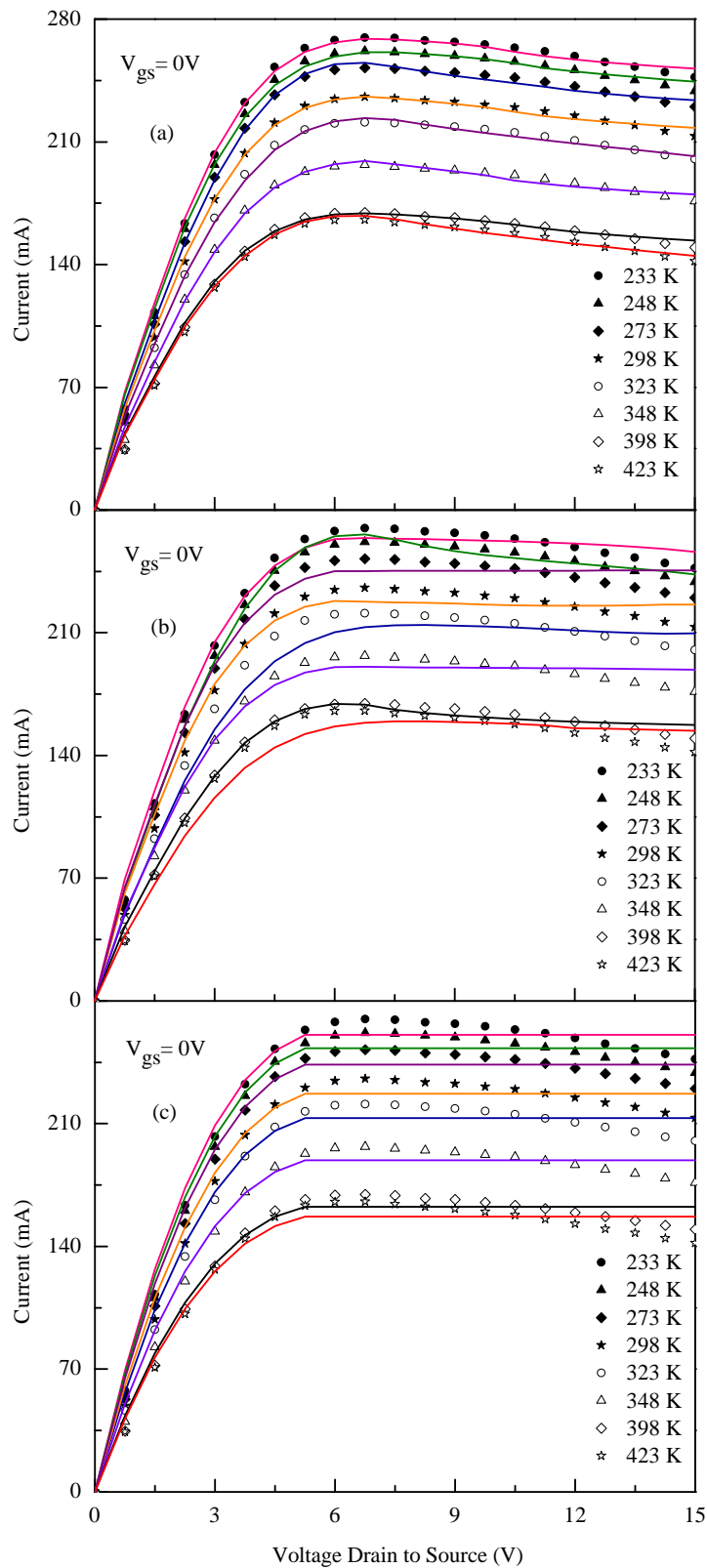


FIGURE 4.3: Temperature dependent observed (symbols) and modeled (solid line)  $I - V$  characteristics of an AlGaN/GaN HEMT having  $0.15 \mu\text{m}$  gate length where; (a) represents this work, (b) represents Wang model and (c) represents Chattopadhyay model.

TABLE 4.1: RMS error comparison of various models for  $I - V$  characteristics of a submicron AlGaIn/GaN HEMT at  $V_{gs} = 0V$ .

Temperature	Wang [97]	Chattopadhyay [22]	Proposed	Improvement
<b>233 K</b>	0.0328	0.0227	0.0128	43.6%
<b>248 K</b>	0.0323	0.0133	0.0132	0.75%
<b>273 K</b>	0.0329	0.0241	0.0130	46.0%
<b>300 K</b>	0.0333	0.0307	0.0175	42.9%
<b>323 K</b>	0.0327	0.0320	0.0183	42.8%
<b>348 K</b>	0.0327	0.0307	0.0149	51.4%
<b>398 K</b>	0.0337	0.0176	0.0163	7.38%
<b>423 K</b>	0.0402	0.0229	0.0172	24.8%

shown by the solid lines. A good accuracy is found between the experimental and the modeled characteristics for the proposed model as shown in Fig. 4.3(a). It is obvious from the figure that the device is operated from  $V_{ds} = 0$  V to 15 V while keeping  $V_{gs} = 0$  V. A decline in  $I_d$  after the onset of current saturation, as evident from Fig. 4.3(a), is associated with the self-heating effect of the device [23, 140]. Owing to that, for  $V_{ds} > V_{ds(sat)}$ ,  $I_d$  continuously reduces its magnitude because a relative increase in channel temperature would increase scattering, causing a reduction in  $v_{sat}$ , which has a direct relationship with  $I_d$ . Fig. 4.3(b) and 4.3(c) show modeled characteristics using Wang [97] and Chattopadhyay [22] models, respectively. Plots of Fig. 4.3 clearly exhibit that the proposed model's performance is considerably better than Wang and Chattopadhyay models especially, in the saturation region of operation. RMS errors for Fig. 4.3 curves have been summarized in Table 4.1 and the data reflect that the improvement in RMS errors offered by the proposed model with respect to the 2<sup>nd</sup> best model is there for all listed temperatures and vary from 0.75 % to 50 %. Therefore, it reflects that the proposed model offers improve performance in predicting temperature dependent characteristics of submicron GaN HEMTs.

Increase in ambient temperature also increases channel temperature, which degrades the power handling capability of the device as shown in Fig. 4.4. This figure is plotted by employing Eq. 4.38 and using the modeled data of Fig. 4.3(a).

Examining the plot of Fig. 4.4, it is obvious that the power handling capability of the device reduces with increasing values of ambient temperature and this decrease follows almost a linear profile. The reduction in power handling capacity of the device with increasing ambient temperature can easily be quantified by considering the maximum power for both 233 K and 423 K plots, when observed at  $V_{ds} = 15$  V. At 233 K, approximately 3.6 W maximum power is observed; whereas, at 423 K the maximum power is approximately 2.2 W.

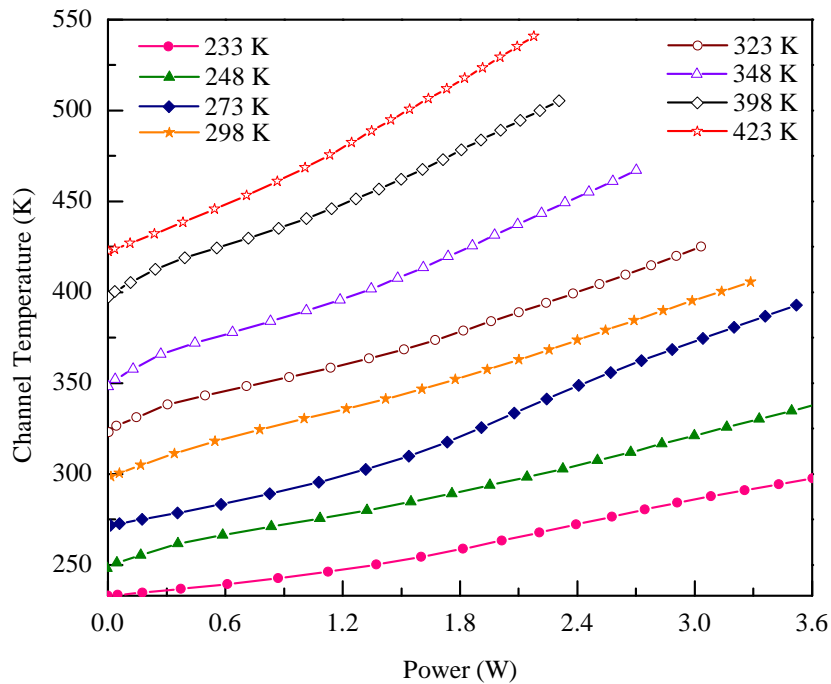
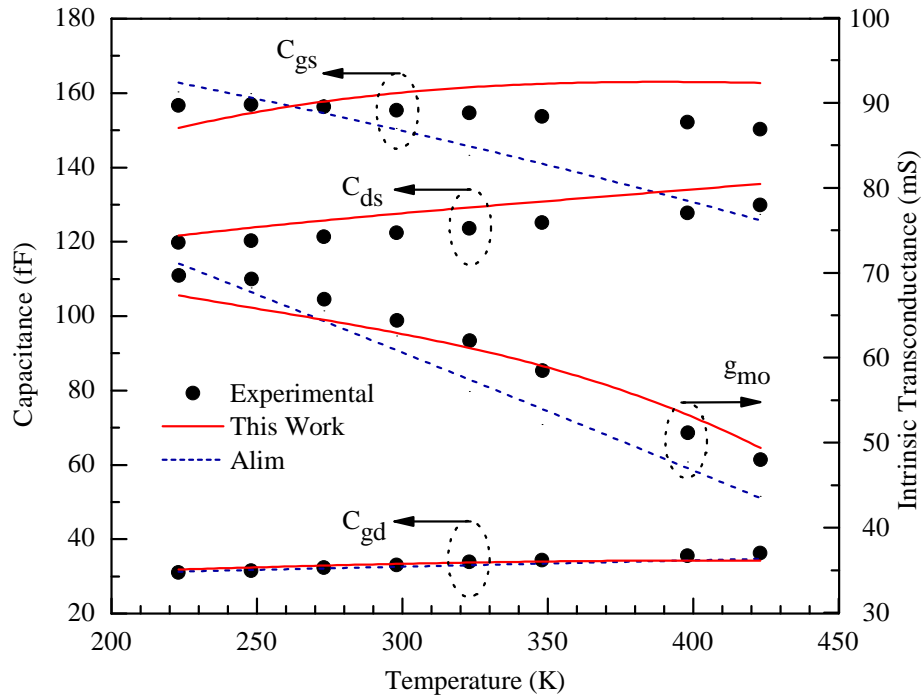


FIGURE 4.4: Channel temperature vs power handling at  $V_{ds} = 0$  V to 15 V of a  $0.15 \mu\text{m} \times 200 \mu\text{m}$  AlGaIn/GaN HEMT.

As it is evident from Eq. (4.1) that by increasing temperature  $V_{th}$  decreases which in turn increases  $n_s$ . For the data of Fig. 4.3(a), the values of  $n_s$  have been calculated using Eq. (4.10) and the same are shown in Table 4.2. It is obvious from the data of Table 4.2, as the ambient temperature increases, more and more electrons are inducted into the channel, as a result  $n_s$  of the device increases. Prima facie, increase in  $n_s$  should increase  $I_d$  [134] but, the fact of the matter is that a reduction in  $I_d$  is observed as demonstrated by the plot of Fig. 4.3. A plausible explanation of such a behavior could be that at increased temperatures, the channel carriers observed increased scattering due to high amplitude phonon, causing

TABLE 4.2: Charge density and temperature coefficient values of an AlGaIn/GaN HEMT at different ambient temperature.

$T(\text{K})$	$n_s \times 10^{17}(\text{m}^{-2})$	$\xi \times 10^{-14}(\text{Vm})$
233	1.44	2.96
248	1.55	6.57
273	1.67	13.16
298	1.78	13.70
323	1.96	16.57
348	1.99	18.37
398	2.06	19.52
423	2.42	28.91

FIGURE 4.5: Effect of temperature on the capacitances and the transconductance of an AlGaIn/GaN HEMT having gate length  $0.15 \mu\text{m}$  at  $V_{ds} = 15 \text{ V}$  and  $V_{gs} = -4.8 \text{ V}$ .

the temperature dependent mobility,  $\mu_T$  (Eq. 4.46) to reduce. The reduction in  $\mu_T$  leads to the reduction of  $v_{sat}$  and hence  $I_d$  of the device.

Figure 4.5 shows experimental and modeled intrinsic parameters of a  $0.15 \mu\text{m}$  gate length AlGaIn/GaN HEMT [23]. The plots of the figure exhibit variation in

capacitances along with  $g_{m0}$  of the device as a function of ambient temperature. It is obvious, by examining the data of the figure, that the variation in capacitance values by changing the ambient temperature is nominal while a significant variation in the magnitude of  $g_{m0}$  is noticed, which could primarily be associated with the reduction of current as a function of ambient temperature as is seen in Fig. 4.3. Dotted lines of Fig. 4.5 exhibit Alim model [23] whereas, solid lines represent variation in the device parameters using the proposed technique. It can be seen from the figure that both the models exhibit discrepancies in predicting the device temperature dependent parameters; however, the deviation offered by Alim model is much higher compared to the proposed technique. Thus, the proposed technique could be called as a relatively better technique to predict temperature dependent intrinsic small signal parameters of GaN based HEMTs.

Figure 4.6 shows variation in the device intrinsic resistances as a function of ambient temperature, wherein both  $R_i$  and  $R_{ds}$  resistors of the device equivalent circuit, shown in Fig. 4.1, exhibit an increasing trend as a function of ambient temperature. The resistor  $R_i$  is calculated using Eq. (4.45); whereas, the value of  $R_{ds}$  is evaluated using the reciprocal of Eq. (4.42). Increase in resistance as a function of temperature, as evident from Fig. 4.6, could be associated with increased hindrance to the flow of carriers due to a relatively high amplitude lattice vibration of the device caused by the ambient temperature. Since, the defining variables of both the equations (4.42, 4.45) are temperature sensitive therefore, a good agreement between the experimental and observed characteristics of the Fig. 4.6 plots are observed. These plots once again demonstrate that the developed technique has the potential to predict temperature dependent intrinsic small signal parameters using the device DC characteristics.

Figure 4.7 shows behavior of  $f_T$  and  $\tau$  as a function of ambient temperature. Solid lines of the plot represented the proposed model and are attained using Eqs. (4.55) and (4.56). It can be seen from the plots of Fig. 4.7 that the proposed model is better in predicting the values of  $f_T$  as a function of temperature whilst Alim model has better accuracy in predicting  $\tau$  at relatively lower temperatures but at higher temperature, the model starts deteriorating where the proposed model

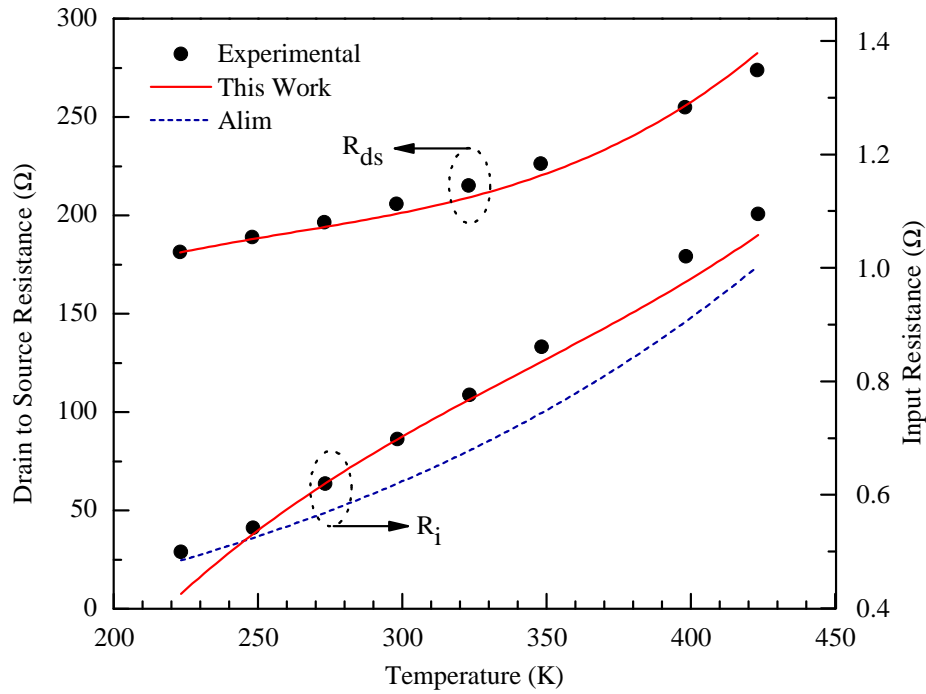


FIGURE 4.6: Effect of temperature on the resistances of an AlGaN/GaN HEMT having gate length  $0.15 \mu\text{m}$  at  $V_{ds} = 15 \text{ V}$  and  $V_{gs} = -4.8 \text{ V}$ .

showed improvement. In general, the proposed model performance for predicting  $\tau$  and  $f_T$  remained consistent and stayed within acceptable (10%) margins for the entire range of temperature under consideration.

A simultaneous observation of modeled characteristics of Figs. 4.5 to 4.7 exhibits that the proposed model is relatively better compared to Alim model. For the given range of temperature the average discrepancies between the observed and the modeled data have been evaluated by assessing RMS errors and the same are summarized in Table 4.3. Assessment of  $C_{gd}$  by both the model is almost identical and the same is obvious from Fig. 4.5. Data of Table 4.3 once again demonstrate that the proposed technique, in general, is better in predicting temperature dependent small signal parameters for submicrom GaN HEMTs.

An overall improvement observed in the prediction of small signal parameters of a GaN HEMT by the proposed model could primarily be associated with the temperature dependent assessment of  $n_s$ . According to Alim model there is a nominal change in the magnitude of  $n_s$  while changing the temperature from 233

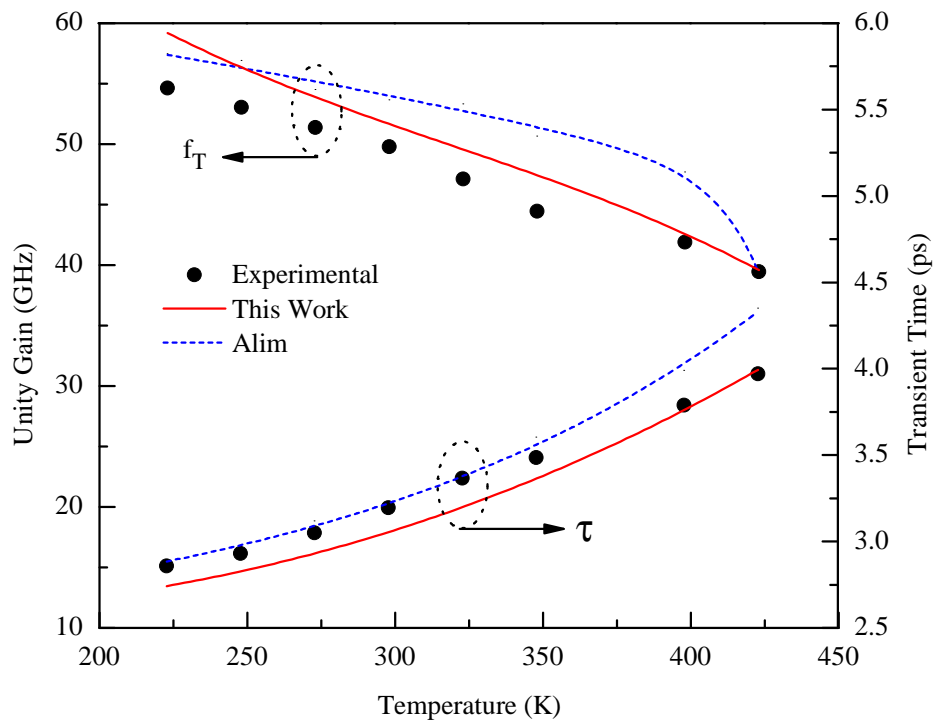


FIGURE 4.7: Effect of temperature on transient time and unity gain frequency of an AlGaIn/GaN HEMT having gate length  $0.15 \mu\text{m}$  at  $V_{ds} = 15 \text{ V}$  and  $V_{gs} = -4.8 \text{ V}$ .

TABLE 4.3: Comparison between average RMS errors for the proposed and Alim model in assessing intrinsic small signal parameters of a GaN HEMT for temperature range 233 K to 423 K.

RMSE	$C_{gs}$	$C_{ds}$	$C_{gd}$	$g_{m0}$	$f_T$	$\tau$	$R_{ds}$	$R_i$
Alim	1.097	—	<b>0.024</b>	0.212	0.408	<b>0.055</b>	—	0.095
Proposed	<b>0.425</b>	<b>0.246</b>	0.033	<b>0.075</b>	<b>0.194</b>	0.089	<b>0.143</b>	<b>0.018</b>

K to 423 K and that too with negative slope as shown in Fig. 4.8. However, according to the proposed model there is a noticeable change in the concentration of  $n_s$  with increasing values of temperature and the slope of  $n_s$  vs temperature profile is positive as evident from Fig. 4.8. Alim model explains the presence of negative conductance in the saturation region of operation, as seen in Fig. 4.3, by assuming reduction in  $n_s$  but, in this work, by attaining a reasonable fit between the experimental and the modeled characteristics of Fig. 4.3(a), it is observed that  $n_s$  increases with increasing values of temperature as given by Eq. (4.10).



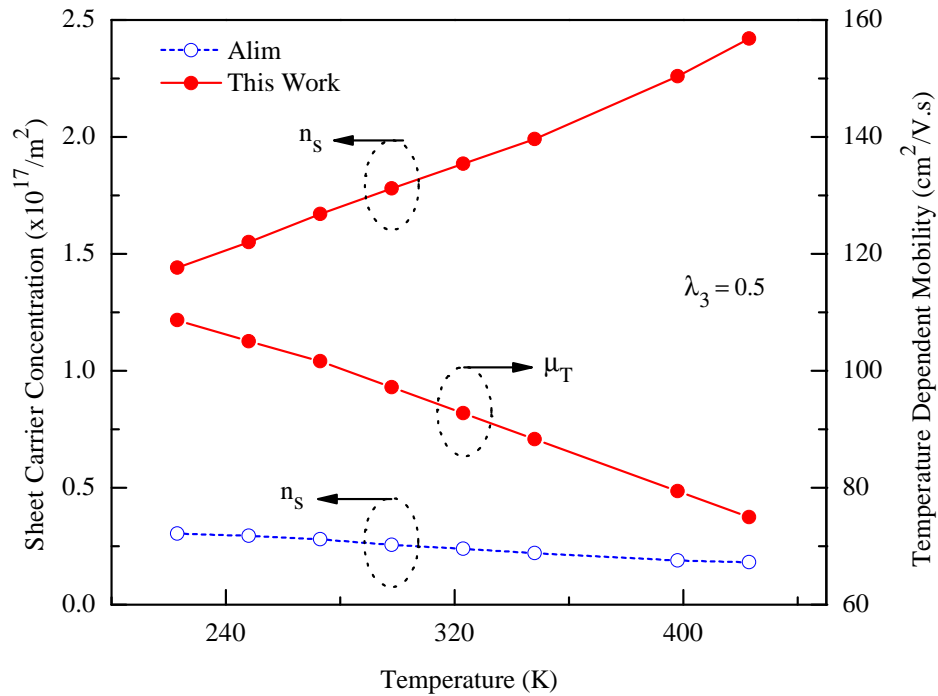


FIGURE 4.8: Effect of temperature on the sheet carrier concentration and mobility of an AlGaIn/GaN HEMT having gate length  $0.15 \mu\text{m}$  at  $V_{ds} = 15 \text{ V}$  and  $V_{gs} = -4.8 \text{ V}$ .

TABLE 4.4: Calculated intrinsic parameters by the proposed technique at  $T = 398 \text{ K}$  for a  $0.15 \mu\text{m}$  AlGaIn/GaN HEMT at  $V_{gs} = -4.8 \text{ V}$  and  $V_{ds} = 15 \text{ V}$ .

$C_{gs}$ (fF)	$C_{ds}$ (fF)	$C_{gd}$ (fF)	$g_{m0}$ (mS)	$\tau$ (ps)	$R_{ds}$ ( $\Omega$ )	$R_i$ ( $\Omega$ )
163.0	132.9	34.1	52.3	3.88	260.6	1.01

On the other hand, observed reduction in  $I_d$  in the saturation region of operation is assumed to be associated with temperature dependent  $\mu_T$  as explained before.

Using analytically assessed intrinsic small signal parameters as given in Table 4.4 for the device under discussion, Y-parameters have been calculated as defined by Eq. (4.57), which lead to the assessment of S-parameters using Eqs. (4.58) to (4.61). Experimental [23, 141] along with modeled S-parameters of a  $0.15 \mu\text{m}$  device are shown in Fig. 4.9. Plots of Fig. 4.9 show that all the four modeled S-parameters are in a reasonable agreement with the experimental data. It is

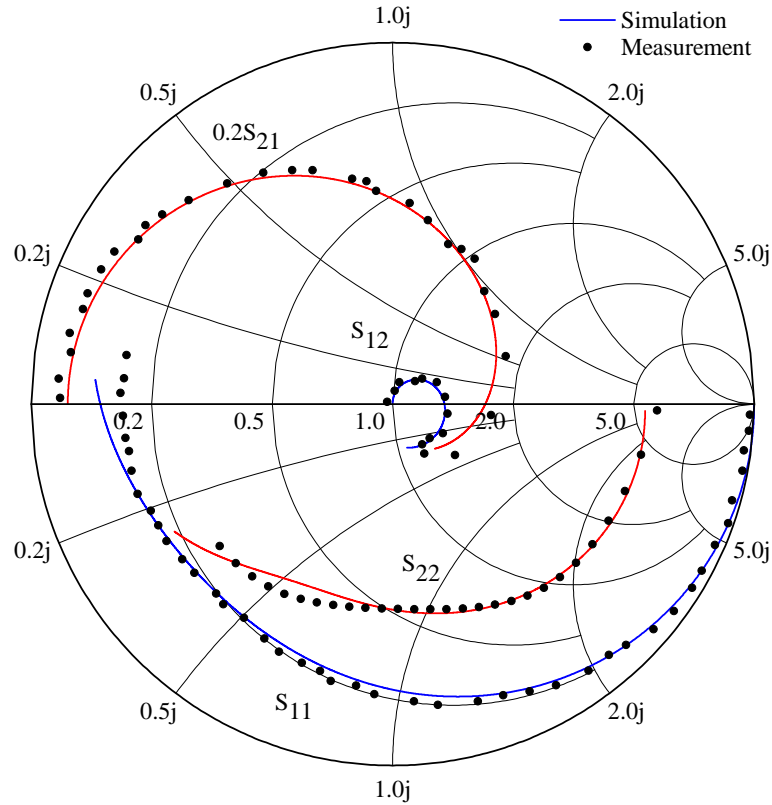


FIGURE 4.9: Measured [23, 141] and modeled S-parameters of  $0.15 \mu\text{m}$  AlGaIn/GaN HEMT at  $T = 398 \text{ K}$  for  $V_{gs} = -4.8 \text{ V}$  and  $V_{ds} = 15 \text{ V}$ .

worth mentioning that the modeled characteristics of Fig. 4.9 are attained using the device  $I - V$  characteristics by involving the proposed technique. Since, modeled S-parameters exhibit a reasonable match with the experimental data of the device thus, one can claim that temperature dependent AC performance of an AlGaIn/GaN HEMT can be predicted by evaluating its temperature dependent DC characteristics by using the proposed technique. Since, AC evaluation relative to DC measurements is considered as a cumbersome job therefore, the developed technique provides an alternative to design engineers to have a feel of the device operation as a function of temperature and frequency by evaluating its DC characteristics.

## 4.4 Summary

In this chapter, a modified model for submicron AlGa<sub>N</sub>/Ga<sub>N</sub> HEMTs has been presented to evaluate temperature dependent characteristics. In the proposed technique, temperature dependent sheet charge density,  $n_s$  in 2-DEG of a HEMT has been evaluated by a relatively simplified approach. Ambient and self-heating effects have been incorporated in the proposed technique to predict  $I - V$  characteristics of submicron AlGa<sub>N</sub>/Ga<sub>N</sub> HEMTs as a function of temperature. Validity of the proposed technique has been established using experimental data of  $0.15\mu\text{m}$  gate length AlGa<sub>N</sub>/Ga<sub>N</sub> HEMT for the temperature ranging from 233 K to 423 K. Engaging the modeled DC data, device intrinsic small signal parameters have been evaluated. Moreover, by employing assessed small signal parameters, S-parameters of the device have also been calculated and their comparison with the measured data demonstrated the validity of the proposed technique. The proposed technique could be used as a tool to assess temperature dependent intrinsic AC parameters of Ga<sub>N</sub> based HEMTs.

# Chapter 5

## Simulation and Comparative Analysis of Submicron GaN HEMTs DC Characteristics

### 5.1 Introduction

Devices fabricated using wide bandgap materials like SiC and GaN offer superior high temperature characteristics compared to Si or GaAs based devices [142]. Si devices can operate up to a maximum of  $\sim 200$  °C ambient temperature and any system where the operating temperature is higher than that, an efficient cooling mechanism will be required to keep the operating temperature of the device within safe limits; to avoid the avalanche breakdown [2, 143]. On the other hand, the performance of GaAs devices also deteriorates at elevated temperature primarily due to increased Schottky barrier leakage [144]. To overcome these limitations and to fabricate devices capable of functioning at elevated temperature ( $\sim 250$  °C or higher), wide bandgap materials are preferred, which compared to Si or GaAs, offer much higher breakdown voltages and thermal stability; allowing the devices to operate at relatively higher ambient temperature and in harsh environment [99, 145, 146].

GaN HEMT was introduced by Khan et al. in 1993 [52] and its basic structure is shown in Fig. 1.4. During earlier stages, the device were fabricated on Si/SiC, but with the availability of GaN substrate, the quality of the transistor has improved many fold, and now the device is engaged quite often in high-tech microwave power applications [2, 98, 99]. For such applications GaN HEMT is considered a promising candidate because, it has better figure of merit than its SiC counterparts. Another attractive feature of GaN HEMT is that it does not require a donor layer for the generation of 2-DEG, because of the polar nature of GaN [9]. Carriers are generated and trapped in bandgap discontinuity,  $\Delta E_c$  under the influence of a piezoelectric force; as a result the device gives high carrier mobility ( $1200\text{-}2000\text{ cm}^2\text{V}^{-1}$ ) due to nominal ionic scattering [2]. Furthermore, sheet carrier concentration,  $n_s$  of 2-DEG can be controlled by controlling the layers structure of the device. Since, there is a wider bandgap offered by the defining layers of the device, resultantly  $\Delta E_c$  can be better maneuvered and hence the  $n_s$ . Owing to these inherent features, GaN HEMTs offer improved  $n_s$ , along with improved switching speed ( $\sim 160\text{ GHz}$ ) and also a considerably higher power density ( $\sim 12\text{ W/mm}$ ); making the device a preferred choice for microwave power applications [112, 147–150].

The performance of a GaN HEMT deteriorates when its lattice gets heated because of intense electric field inside the channel referred to as self heating effects. These effects include reduction in: (a) the Schottky barrier height,  $\phi_b(T)$ ; (b) the mobility,  $\mu(T)$ , of 2-DEG carriers; (c) the saturation velocity,  $v_s$  and also (d) the  $\Delta E_c$  of the heterostructure. Collectively, all these factors contribute negatively towards the performance of the device and it is therefore, important that one should know the operating conditions in which the device is supposed to be functioning. Additionally, in power related applications; such devices are placed in an environment where the temperature is higher than the room temperature which further aggravates the operating conditions for the device. In [100], it is shown that ambient temperature further increases the channel temperature of the device and its ultimate operating capability reduces with increasing ambient temperature. They further showed that the device channel temperature, which controls

its characteristics, depends on the device physical parameters and its geometry.

There does not exist any global mechanism, which can be employed to assess the channel temperature due to self heating because, it is device geometry dependent and therefore, it will vary from device to device. In 2015, Nazari et al. studied self heating profile of GaN HEMTs and predicted that the channel temperature for  $2.6 \text{ Wmm}^{-1}$  and  $8 \text{ Wmm}^{-1}$  operating conditions could be as high as  $\sim 125 \text{ }^\circ\text{C}$  and  $\sim 350 \text{ }^\circ\text{C}$  above the ambient temperature, respectively [151]. Alim et al. investigated the impact of ambient temperature on DC and AC characteristics of submicron GaN HEMTs and reported that there would be a reduction in the device output current with increasing ambient temperature. Furthermore, their experimental data revealed that AC performance also deteriorates both with increasing ambient temperature and self heating [141].

Dependence of GaN HEMT performance on numerous parameters as discussed above requires a compact model to simulate the device characteristics both at room as well as at elevated temperatures. A compact device model would be the one which can predict the device drain-to-source current,  $I_{ds}$  as a function of applied drain-to-source,  $V_{ds}$ , and gate-to-source,  $V_{gs}$  bias. It should adequately address the influence of ambient temperature and self heating on the device characteristics. Moreover, the model should also explain changes in  $I_{ds}$  with varying device physical parameters; such as gate length,  $L_g$ , gate width  $W$ , threshold voltage,  $V_{th}$  and  $n_s$  etc. It should also have the flexibility to be employed in simulation software, to extend the device knowledge into circuits involving GaN HEMTs [107, 108].

A review of GaN HEMTs models has been carried out by Santi et al. in 2015, wherein it was observed that very few models have been proposed to simulate GaN HEMT characteristics for power related applications [108]. Physics based models are too complicated [110] to be employed in a circuit simulation software and usually semi-physics or numerical techniques are used to predict fundamental characteristics of the device in computer aided design (CAD). According to our assessment, numerical models developed for GaAs MESFETs are being used to simulate  $I - V$  characteristic of GaN HEMTs; as an example in [112] Curtice

model developed for MESFET has been employed to simulate GaN HEMT characteristics. GaAs MESFETs models [101–106] are bound to lose their accuracy when the device characteristics exhibit noticeable self heating effect. It is therefore, pertinent to have a model for GaN HEMTs which can simulate their  $I - V$  characteristics as a function of  $V_{ds}$  and  $V_{gs}$ , with a good degree of accuracy, and the model should be compact enough to be employed in CAD.

In this chapter, an attempt has been made to develop a compact model for submicron GaN HEMTs and to assess its accuracy comparative to other such models reported in literature. The remaining composition of the chapter is that Section 5.2 deals with the development of model. This section also describes particle swarm optimization technique, which is engaged in the process to attain best values for simulation parameters. Section 5.3 describes a comparative performance of the developed technique and finally, Section 5.4 gives conclusions of the proposed research.

## 5.2 Model Development

In the saturation region of operation,  $I_{ds}$  of an FET can be approximated as

$$I_{ds} = I_{dss} \left( 1 - \frac{V_{gs}}{\Delta V_{th} + \gamma V_{ds}} \right)^\delta, \quad (5.1)$$

where  $\Delta$  shows an adjustment in  $V_{th} = \phi_b(T) - \Delta E_c(T) - \sigma d / \varepsilon_s$ , because of the submicron geometry of the device. Here  $\sigma$  and  $\varepsilon_s$  represent conductivity and permittivity of the semiconductor involved and variable  $d$  is shown in Fig. 1.4. In Eq. (5.1),  $\gamma$  is a fitting parameter, which simulates dependence of  $V_{th}$  on  $V_{ds}$ ,  $I_{dss}$  represents saturation current at  $V_{gs} = 0$  V and is expressed as  $I_{dss} = qWn_s v_s$  where,  $q$  represents a unit electron charge and  $v_s$  is the saturation velocity of electrons. Variable  $n_s = [\varepsilon_s / (qd)][V_{gs} - V_{th} - E_F - V_{ds}]$  is controlled by the mole fraction of  $\text{Al}_{(1-x)}\text{Ga}_x\text{N}/\text{GaN}$  heterojunction through its Fermi energy,  $E_F$ , and at a given temperature and bias, its value remains constant [96].

Under ideal conditions,  $\delta = 2$ ; which reduces Eq. (5.1) to standard square law expression of a FET commonly known as Shockley expression [19]. But, for GaN HEMTs, the value of  $\delta$  will vary depending upon the quality of Schottky barrier gate and self heating effects. To have a complete sweep from  $0 < V_{ds} < V_{ds(\text{Breakdown})}$  tanh function can be employed as shown below

$$I_{ds} = I_{dss} \left( 1 - \frac{V_{gs}}{\Delta V_{th} + \gamma V_{ds}} \right)^\delta \tanh(\alpha V_{ds}), \quad (5.2)$$

where  $\alpha$  is a fitting variable which adjusts the slope of linear region as per the resistance offered by the device. It is an established fact that after the onset of saturation, there is a finite conductance, which depends both on  $V_{gs}$  and  $V_{ds}$ . To accommodate this aspect, the above expression is modified as

$$I_{ds} = I_{dss} \left( 1 - \frac{V_{gs}}{\Delta V_{th} + \gamma V_{ds}} \right)^\delta \tanh(\alpha V_{ds})(1 + \lambda_1 V_{ds} + \lambda_2 V_{gs}), \quad (5.3)$$

where,  $\lambda_1$  and  $\lambda_2$  are fitting variables controlling the dependence of  $I_{ds}$  on  $V_{ds}$  and  $V_{gs}$ , respectively, after the onset of current saturation. In GaN HEMTs, contrary to MESFETs, there exists significant self-heating effects which at low  $V_{gs}$  generates negative output conductance in the saturation region. To accommodate this effect, the temperature dependent current,  $I_{dsT}$  is defined as

$$I_{dsT} = I_{ds} - I_{ds}(\lambda_3 V_{ds0}), \quad (5.4)$$

where  $\lambda_3 = (\xi + T/300)$  is a simulation variable, which controls the effect of temperature,  $T$  on the device characteristics and  $\xi$  adjust its effect as per the channel conditions. Variable  $V_{ds0}$  of the above mentioned expression is defined as

$$V_{ds0} = \frac{V_{ds}}{\left[ 1 - \left( \frac{V_{gs}}{V_{th}} \right)^\eta \right]^{1/\eta}},$$

here  $\eta$  is an adjustment factor.

Plotting of Eq. (5.4) as a function of  $V_{ds}$  and  $V_{gs}$ , will generate a family of curves



representing output characteristics of the device. Differentiating Eq. (5.4) with respect to  $V_{ds}$  and  $V_{gs}$ , output conductance,  $g_d$ , and transconductance,  $g_m$ , are attained, respectively.

$$\begin{aligned}
 g_d = & I_{dss}\lambda_1 \tanh(\alpha V_{ds})S_4 - \alpha I_{dss}S_1S_2S_4 + \frac{I_{dss}\lambda_3 \tanh(\alpha V_{ds})S_1S_4}{\eta S_3} \\
 & + \frac{\gamma \delta I_{dss}V_{gs} \tanh(\alpha V_{ds})S_1S_5}{S_6^2} + \frac{\lambda_1 \lambda_3 I_{dss}V_{ds} \tanh(\alpha V_{ds})S_4}{\eta S_3} \\
 & - \frac{\alpha \lambda_3 I_{dss}V_{ds}S_1S_2S_4}{\eta S_3} + \frac{\gamma \delta \lambda_3 I_{dss}V_{gs}V_{ds} \tanh(\alpha V_{ds})S_1S_5}{\eta S_3 S_6^2},
 \end{aligned} \tag{5.5}$$

and

$$\begin{aligned}
 g_m = & \lambda_2 I_{dss} \tanh(\alpha V_{ds})S_4 - \frac{\delta I_{dss} \tanh(\alpha V_{ds})S_1S_5}{S_6} + \frac{\lambda_2 \lambda_3 I_{dss}V_{ds} \tanh(\alpha V_{ds})S_4}{\eta S_3} \\
 & - \frac{\lambda_3 I_{dss}V_{ds} \tanh(\alpha V_{ds})S_1S_4S_7}{V_{th}S_3^2} - \frac{\delta \lambda_3 I_{dss}V_{ds} \tanh(\alpha V_{ds})S_1S_5}{\eta S_3 S_6},
 \end{aligned} \tag{5.6}$$

where

$$S_1 = \lambda_1 V_{ds} + \lambda_2 V_{gs} + 1,$$

$$S_2 = \tanh^2(\alpha V_{ds}) - 1,$$

$$S_3 = \left( \frac{V_{gs}}{V_{th}} \right)^\eta - 1,$$

$$S_4 = \left( 1 - \frac{V_{gs}}{S_6} \right)^\delta,$$

$$S_5 = \left( 1 - \frac{V_{gs}}{S_6} \right)^{\delta-1},$$

$$S_6 = \Delta V_{th} + \gamma V_{ds},$$

$$S_7 = \left( \frac{V_{gs}}{V_{th}} \right)^{\eta-1}.$$

Equation (5.4) represents the proposed model to simulate output characteristics of a GaN HEMT provided that, the simulation parameters are known. To evaluate simulation parameters of the proposed model, for a given device, particle swarm optimization algorithm is developed in MATLAB and the detail of which is given in the following section.

### 5.2.1 Particle Swarm Optimization

PSO is a powerful tool to generate optimum values, with a highest level of repeatability, for variables used in a modeling expression [152]. In PSO, the position of each particle at any time,  $X_{ij}(t)$ , is defined as

$$X_{ij}(t) = \begin{bmatrix} X_{11} & X_{12} & \cdots & X_{1k} & \cdots & X_{1j} \\ X_{21} & X_{22} & \cdots & X_{2k} & \cdots & X_{2j} \\ \vdots & \vdots & \ddots & \vdots & \ddots & \vdots \\ X_{l1} & X_{l2} & \cdots & X_{lk} & \cdots & X_{lj} \\ \vdots & \vdots & \ddots & \vdots & \ddots & \vdots \\ X_{i1} & X_{i2} & \cdots & X_{ik} & \cdots & X_{ij} \end{bmatrix}, \quad (5.7)$$

where  $i$  is the number of batches of particles  $j$ , and  $k$  and  $l$  are intermediary variables. The velocity of each batch of particles is defined by a vector,  $V_j(t)$  given as

$$V_j(t) = \begin{bmatrix} V_1 \\ V_2 \\ \vdots \\ V_k \\ \vdots \\ V_j \end{bmatrix}. \quad (5.8)$$

Each batch's velocity is acquired by

$$V_j(t) = \frac{\max(X_{:j}) - \min(X_{:j})}{2} \quad (5.9)$$

Using the definition of RMSE, the best local for each particle,  $X_{best(ij)}$  with respect to least RMSE is accumulated as

$$X_{best(ij)}(t) = \begin{bmatrix} X_{best(11)} & X_{best(12)} & \cdots & X_{best(1k)} & \cdots & X_{best(1j)} \\ X_{best(21)} & X_{best(22)} & \cdots & X_{best(2k)} & \cdots & X_{best(2j)} \\ \vdots & \vdots & \ddots & \vdots & \ddots & \vdots \\ X_{best(l1)} & X_{best(l2)} & \cdots & X_{best(lk)} & \cdots & X_{best(lj)} \\ \vdots & \vdots & \ddots & \vdots & \ddots & \vdots \\ X_{best(i1)} & X_{best(i2)} & \cdots & X_{best(ik)} & \cdots & X_{best(ij)} \end{bmatrix}. \quad (5.10)$$

At time  $t$ , the best global position,  $X_{global(j)}$  which corresponds to the least RMSE of all the batches given in Eq. (5.10) is given by

$$X_{global(j)}(t) = \begin{bmatrix} X_{global(1)} & X_{global(2)} & \cdots & X_{global(k)} & \cdots & X_{global(j)} \\ X_{global(1)} & X_{global(2)} & \cdots & X_{global(k)} & \cdots & X_{global(j)} \\ \vdots & \vdots & \ddots & \vdots & \ddots & \vdots \\ X_{global(1)} & X_{global(2)} & \cdots & X_{global(k)} & \cdots & X_{global(j)} \\ \vdots & \vdots & \ddots & \vdots & \ddots & \vdots \\ X_{global(1)} & X_{global(2)} & \cdots & X_{global(k)} & \cdots & X_{global(j)} \end{bmatrix}. \quad (5.11)$$

The rows of the matrix given in Eq. (5.11) are the same as there exists only one best global solution for each particle batch at time  $t$ . The particle velocity is updated at each time interval using Eq. (5.12)

$$V_j(t+1) = V_j(t) + V_j(t-1). \quad (5.12)$$

And to update the current position, the following equation is used

$$X_{ij}(t+1) = X_{ij}(t) + \Delta X_{ij}(t). \quad (5.13)$$

In Eq. (5.13),  $\Delta X_{ij}(t)$  is represented by the finite difference equation given by

$$\Delta X_{ij}(t) = \kappa \{ X_{ij}(t-1) + f_1 [X_{best(j)} - X_{ij}(t)] + f_2 [X_{global(j)} - X_{ij}(t)] \}, \quad (5.14)$$

Here,  $f_1$  and  $f_2$  are the learning rates of the equation defined as

$$f_1 = f_{max(1)} + \frac{f_{max(1)} - f_{min(1)}}{i_{max}} (i_{max} - i), \quad (5.15)$$

$$f_2 = f_{max(2)} + \frac{f_{max(2)} - f_{min(2)}}{i_{max}} (i_{max} - i), \quad (5.16)$$

where,  $f_{max(1)}$ ,  $f_{max(2)}$  and  $f_{min(1)}$ ,  $f_{min(2)}$  are the maximum and minimum values of  $f_1$  and  $f_2$ , respectively and  $i_{max}$  is the total number of batches. The variable  $\kappa$  controls the position matrix such that  $V_j(t+1) \leq V_j(t)$ , which leads to negative velocity, satisfying the basic convergence criterion: i.e. for a particle to converge to its equilibrium point  $X_{ij}(t)V_j(t) < 0$ .

RMSE cost function is used to drive the particle positions and is given by

$$\text{RMSE} = \sqrt{\sum_{Q=R}^N \left\{ \sum_{P=S}^M \left( I_{dsT(\text{exp})}^{P,Q} - I_{dsT(\text{sim})}^{P,Q} \right)^2 \right\} / \sum_{P=S}^M I_{dsT(\text{exp})}^{P,Q}} \leq E_{r(\text{min})}. \quad (5.17)$$

In Eq. (5.17),  $E_{r(\text{min})}$  represents minimum error tolerance,  $I_{dsT(\text{exp})}$  and  $I_{dsT(\text{sim})}$  are the experimental and the simulated currents, respectively. Variables  $P$  and  $Q$  are the applied  $V_{gs}$  and  $V_{ds}$  having minimum value  $S$  and  $R$ , respectively and maximum value  $M$  and  $N$ , respectively.

PSO is designed to comply the following course:

- (i) to initialize velocity, position and swarm dimension;
- (ii) to define the cost function;
- (iii) to update the parameters locally;
- (iv) to find best parameters globally;
- (v) to update parameters according to global best and

- (vi) to go to step (iii) if  $E_{r(\min)}$  is not achieved or iterations are not complete, else terminate.

### 5.3 Results and Discussion

To check the validity of the proposed model, a set of devices has been selected and the detail of which is given in Table 5.1. To ensure the wider applicability of the proposed technique, the  $L_g$  of the chosen devices varies from 0.25  $\mu\text{m}$  to 0.7  $\mu\text{m}$ . By employing the developed MATLAB code, simulation variables were optimized and are shown in Table 5.2. It is pertinent to mention here that during optimization, the code engages Eqs. (5.4) and (5.17) and tries to figure out values of Eq. (5.4) unknown variables, which generate minimum error relevant to the experimental data. In conformity to the philosophy of PSO, global optimization was ensured through repeatability of results.

Figure 5.1 shows simulated and observed output characteristics of the four chosen devices of Table 5.1. These devices are exhibiting output characteristics with varying profile in the saturation region of operation. By examining Fig. 5.1(a) to (c), it is obvious that the shown characteristics offered two distinct features, which cannot be considered as routine features of a device operating under Shockley principle. First and the foremost is that, the devices at lower negative gate bias  $V_{gs} = -1 \text{ V}$  to  $V_{gs} = -2 \text{ V}$  give poor response relative to higher negative gate bias, say  $V_{gs} = -2 \text{ V}$  to  $V_{gs} = -3 \text{ V}$ . This pattern is repeated in all the four characteristics of Fig. 5.1 therefore, it is an intrinsic feature of the device rather a fabrication constraint. The 2<sup>nd</sup> important feature in the shown output characteristics of Fig. 5.1(a) to (c) is that in the saturation region, especially at  $V_{gs} = 0 \text{ V}$ , plots are exhibiting negative conductance. With increasing negative  $V_{gs}$ , the value of negative conductance is declining and at relatively higher negative  $V_{gs}$  this effect diminishes altogether. In Fig. 5.1(d), this effect is not visible, presumably because of low  $I_{ds}$ , which is in line with the response observed in other devices.

TABLE 5.1: Physical dimensions and constants of four ( $T_1 - T_4$ ) submicron GaN HEMTs, employed to establish the validity of the proposed model.

Device	$L_g$ ( $\mu\text{m}$ )	$W$ ( $\mu\text{m}$ )	$d$ (nm)	$\mu_0$ ( $\text{m}^2/\text{Vs}$ )	$V_T$ (V)
$T_1$ [141]	0.25	200	25	0.26	-5.6
$T_2$ [98]	0.30	50	18	0.15	-4.0
$T_3$ [153]	0.35	250	18	0.04	-3.5
$T_4$ [153]	0.70	25	30	0.05	-3.9

TABLE 5.2: Optimized values for the variables of the proposed model given by Eq. (5.4) for four submicron GaN HEMTs.  $I_{dss}$  is in mA.

Device	$I_{dss}$	$\alpha$	$\gamma$	$\lambda_1$	$\lambda_2$	$\lambda_3$	$\delta$	$\Delta$	$\eta$
$T_1$ [141]	183	0.233	-0.208	-0.009	0.189	-0.0195	0.027	-0.035	1.277
$T_2$ [98]	33	0.225	-0.329	-0.000	0.255	-0.010	1.018	-0.066	0.678
$T_3$ [153]	128	0.427	-0.014	-0.025	0.146	-0.033	1.233	-0.623	0.828
$T_4$ [153]	17	0.475	-1.059	-0.005	0.298	-0.070	0.025	-0.428	3.206

TABLE 5.3: RMS errors of different models for the device  $T_1$  at  $T = 298$  K. Observed average improvement in RMSE relative to the 2<sup>nd</sup> best model is 31% and is shown in bold.

RMS Error	Gate to Source Voltage, $V_{gs}$ (V)						
	0V	-1V	-2V	-3V	-4V	-5V	Avg.
Angelov [103]	0.889	<b>0.262</b>	0.775	0.475	1.136	0.793	0.721
Curtice [101]	0.548	0.427	0.496	0.279	<b>0.214</b>	<b>0.105</b>	0.344
McCament [102]	0.610	0.396	0.713	0.252	0.618	0.172	0.460
Dobes [104]	0.597	0.355	0.696	0.278	0.637	0.179	0.457
Islam [105]	1.733	0.504	1.065	1.182	1.011	1.024	1.086
Riaz [106]	0.759	0.807	0.643	0.524	1.209	0.816	0.793
Proposed	<b>0.102</b>	0.285	<b>0.315</b>	<b>0.215</b>	0.341	0.167	<b>0.237</b>

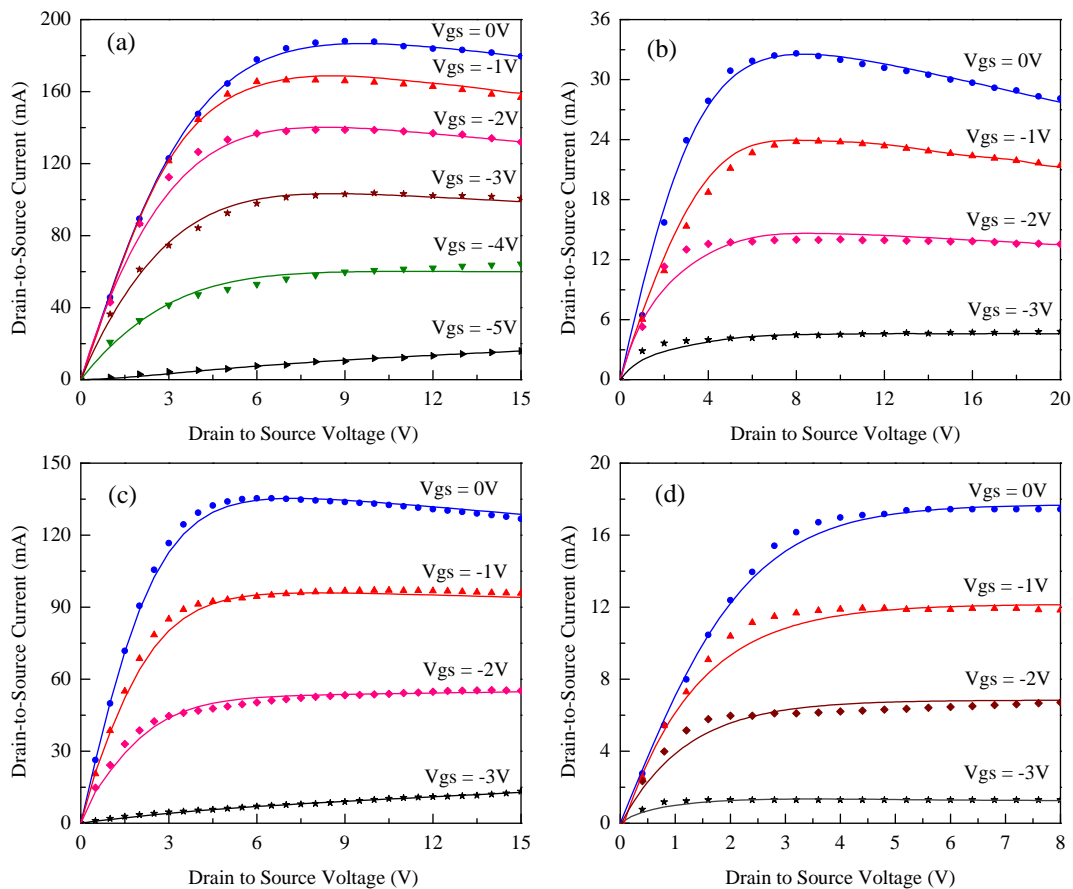


FIGURE 5.1: Simulated (line) and observed (symbols)  $I - V$  characteristics of GaN HEMTs having gate length: a)  $0.25 \mu\text{m}$ ; b)  $0.30 \mu\text{m}$ ; c)  $0.35 \mu\text{m}$  and d)  $0.70 \mu\text{m}$ .

TABLE 5.4: RMS errors in  $I - V$  characteristics of different numerical models for the device  $T_2$  at  $T = 298 \text{ K}$ . Observed improvement in average RMSE relative to the 2<sup>nd</sup> best model is 22% and is shown in bold.

RMS Error	Gate to Source Voltage, $V_{gs}$ (V)				
	0V	-1V	-2V	-3V	Avg.
Angelov [103]	0.153	0.157	0.256	<b>0.084</b>	0.163
Curtice [101]	0.292	0.221	0.169	0.126	0.202
McCamant [102]	0.423	0.569	0.718	0.729	0.609
Dobes [104]	0.435	0.585	0.697	0.773	0.622
Islam [105]	0.742	0.514	0.648	0.360	0.563
Riaz [106]	0.114	0.182	0.260	0.172	0.182
<b>Proposed</b>	<b>0.090</b>	<b>0.134</b>	<b>0.193</b>	0.094	<b>0.127</b>

TABLE 5.5: RMS errors in  $I-V$  characteristics of different numerical models for the device  $T_3$  at  $T = 298$  K. Observed improvement in average RMSE relative to the 2<sup>nd</sup> best model is 17% and is shown in bold.

RMS Error	Gate to Source Voltage, $V_{gs}$ (V)				
	0V	-1V	-2V	-3V	Avg.
Angelov [103]	0.205	0.300	0.353	0.203	0.265
Curtice [101]	0.302	0.083	<b>0.152</b>	<b>0.054</b>	0.147
McCamant [102]	1.159	2.269	2.363	2.682	2.193
Dobes [104]	1.694	2.298	2.464	2.548	2.251
Islam [105]	0.719	0.722	0.782	0.275	0.624
Riaz [106]	0.516	0.294	0.252	0.152	0.303
<b>Proposed</b>	<b>0.176</b>	<b>0.073</b>	0.180	0.059	<b>0.122</b>

An improved response of Schottky barrier gate at relatively higher negative  $V_{gs}$  shows that a simple square law expression will not suffice to simulate  $I-V$  characteristics of GaN HEMTs. A deviation from the square law was inevitable and the same was accommodated in the proposed model by the variable  $\delta$ . Since, in the saturation region of operation output conductance,  $g_d$  has got negative and positive slope dependent upon both  $V_{ds}$  and  $V_{gs}$  whose effect is taken care of by introducing the term  $(1 + \lambda_1 V_{ds} + \lambda_2 V_{gs})$  in the proposed model. Furthermore, the transition from linear to saturation region is dependent both on  $V_{gs}$  and  $V_{th}$ , and that effect is incorporated in the model using the term defined by  $V_{ds0}$  in Eq. (5.4).

Characteristics shown in Fig. 5.1 clearly demonstrate that the proposed model is accurate enough to simulate the  $I-V$  characteristics of GaN HEMTs of varying dimensions. Data shown in Tables 5.3 to 5.6 compare the performance of the proposed model with other models reported in literature [101–106]. Looking at average RMSE, it can be claimed that for the device  $T_1$ , the improvement offered by the proposed model is 31% relative to the 2<sup>nd</sup> best model, which in this case is Curtice model [101]. For the transistor  $T_2$ , the observed improvement is 22% when compared with Angelov model [103]. Furthermore, the proposed model gave an improvement of 17% and 50% for the transistors  $T_3$  and  $T_4$ , respectively, relative



TABLE 5.6: RMS errors in  $I - V$  characteristics of different numerical models for device  $T_4$  at  $T = 298$  K. Observed improvement in average RMSE relative to 2<sup>nd</sup> best model is 50% and is shown in bold.

RMS Error	Gate to Source Voltage, $V_{gs}$ (V)				
	0V	-1V	-2V	-3V	Avg.
Angelov [103]	0.148	0.137	0.128	0.052	0.116
Curtice [101]	0.174	0.115	0.175	0.120	0.146
McCamant [102]	0.384	0.644	0.697	0.704	0.607
Dobes [104]	0.375	0.625	0.669	0.758	0.606
Islam [105]	0.271	0.399	0.401	0.226	0.324
Riaz [106]	0.167	0.124	0.174	0.117	0.145
<b>Proposed</b>	<b>0.068</b>	<b>0.066</b>	<b>0.067</b>	<b>0.034</b>	<b>0.058</b>

once again Curtice as the 2<sup>nd</sup> best model. So in general, it can be said that Curtice model is the 2<sup>nd</sup> best observed model for predicting the output characteristics of GaN HEMTs. However, the data showed that, the proposed model has outperformed the other models in simulating the output characteristics of submicron GaN HEMTs. Hence, it can be a preferred choice for CAD software where GaN HEMTs are involved.

Involving the data given in Table 5.2 and using Eq. (5.5),  $g_d$  of the devices under consideration is plotted and shown in Fig. 5.2. Once again, it can be seen that the simulation follows reasonably well the experimental data both in linear as well as in saturation region of operation. In general,  $g_d$  declines sharply as a function of  $V_{ds}$  however, it saturates after the onset of current saturation and also have negative values for the devices  $T_1$  to  $T_3$ . This is so, because these devices have tangible decline in  $I_{ds}$  with increasing values of  $V_{ds}$  as shown in Fig. 5.1. The decline in  $I_{ds}$  generates a negative resistance, which is associated with inter valley scattering in case of GaAs MESFETs [154] and for GaN HEMTs it is possibly caused by the self heating of the device, which reduces  $\mu$  and hence  $v_s$ .

Apart from the self heating, the device characteristics could be affected by the ambient temperature in which it is being operated. As GaN HEMTs are designed for harsh environment and power related applications where temperature is usually

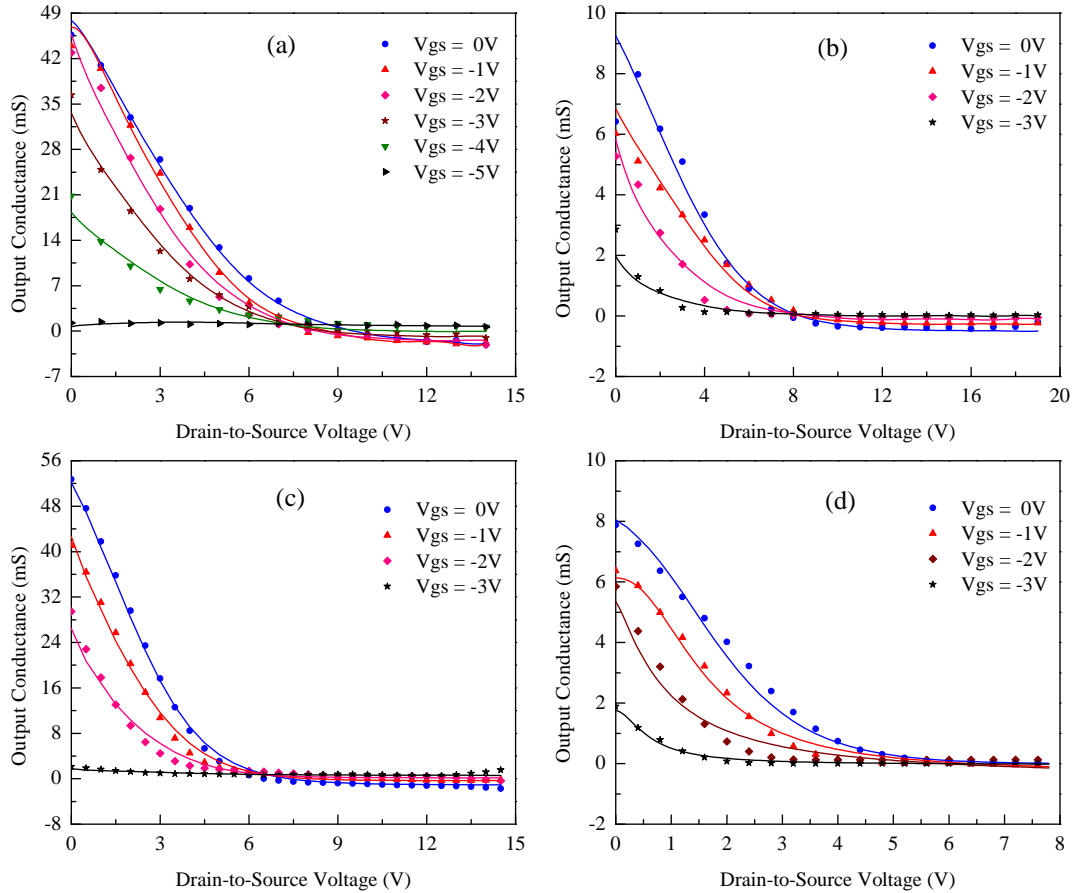


FIGURE 5.2: Simulated and observed output conductance of GaN HEMTs having gate length: a)  $0.25 \mu\text{m}$ ; b)  $0.30 \mu\text{m}$ ; c)  $0.35 \mu\text{m}$  and d)  $0.70 \mu\text{m}$ .

higher than the room temperature, it would be therefore appropriate to check the performance of the proposed model at elevated temperature. In this connection a GaN HEMT having  $L_g = 0.12 \mu\text{m}$  and  $W = 50 \mu\text{m}$  is selected [155] and its output characteristics at three different ambient temperatures, both simulated and measured, are shown in Fig. 5.3. Simulation once again showed a reasonable compliance with experimental data demonstrating the validity of the proposed model for elevated temperature applications.

Table 5.7 shows a comparative assessment of RMSE for a  $0.12 \mu\text{m}$  GaN HEMT at different temperatures. Examining the data of the table, it is once again obvious that the proposed model performance, as a function of temperature, is better than the other models. This suggests that the proposed model can simulate the device characteristics for an environment where the temperature is much higher ( $T = 773 \text{ K}$ ) than the room temperature. The reason that the proposed model is performing

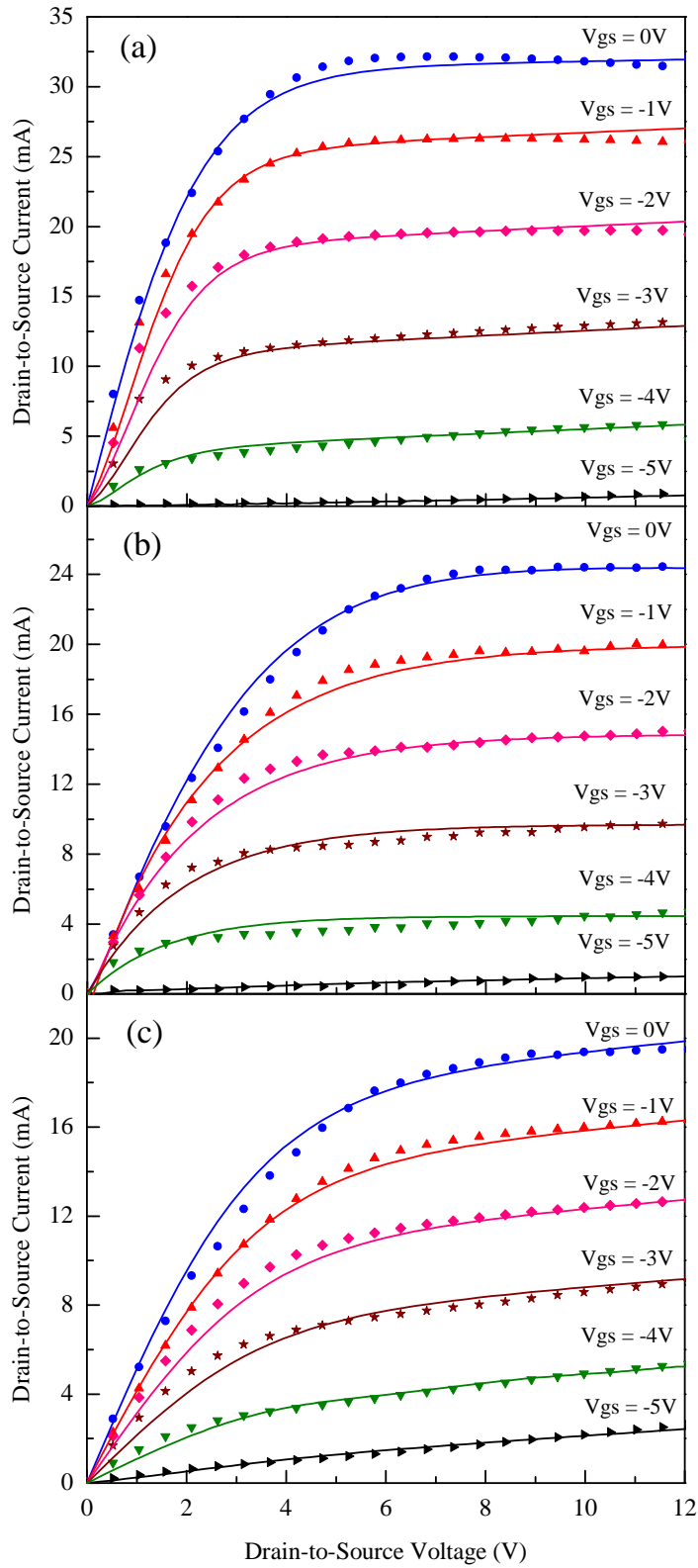


FIGURE 5.3: Temperature dependent simulated (line) and observed (symbols) output characteristics of a  $0.12 \mu\text{m}$  gate length GaN HEMT [155]: a)  $T = 298$  K; b)  $T = 573$  K and c)  $T = 773$  K.

TABLE 5.7: Temperature dependent RMS errors in  $I - V$  characteristics of different numerical models for a  $0.12 \mu\text{m}$  gate length GaN HEMT [155] at various ambient temperatures. Lowest RMSE are shown in bold.

RMS Error	$T = 298 \text{ K}$	$T = 573 \text{ K}$	$T = 773 \text{ K}$
Angelov [103]	0.240	0.205	0.204
Curtice [101]	0.162	0.185	0.117
McCamant [102]	0.235	0.199	0.156
Dobes [104]	0.221	0.187	0.140
Islam [105]	0.585	0.395	0.254
Riaz [106]	0.188	0.188	0.113
<b>Proposed</b>	<b>0.156</b>	<b>0.134</b>	<b>0.096</b>

better than the other models under consideration is, that the proposed model is especially designed, keeping in view the effects of: a) self heating; b) ambient heating and c)  $g_m$  appearance at relatively higher negative gate bias.

Figure 5.4 shows variation in  $g_m$  as a function of  $V_{gs}$  with  $V_{ds}$  as a constant. The solid lines of the figure are attained from Eq. (5.6) after attaining a DC fit as shown in Fig. 5.3; whereas, symbols show experimental data at different temperatures. It is observed that the peak  $g_m$  is appearing at  $V_{gs} \approx -2.5 \text{ V}$  and this peak is reducing and flattening with increasing temperature. Appearing of the peak  $g_m$  at relatively higher negative gate bias is a clear indication that at  $V_{gs} \approx -2.5 \text{ V}$ , Schottky barrier gate is more effective than prior or after that bias. It is pertinent to mention here that AlGaN layer as shown in Fig. 1.4 must not contribute in HEMT operation. To get an appropriate HEMT's operation, this layer must be designed such that it is fully depleted by Schottky barrier built-in potential at  $V_{gs} = 0 \text{ V}$ . In such a case, when  $V_{gs} < 0 \text{ V}$ , for an  $n$ -channel device, the gate depletion moves towards 2-DEG and its movement is a non-linear movement given by  $V_{gs} \propto d^2$ . A standard profile of  $\sqrt{V_{gs}} \sim d$  plot represents more effectiveness of the gate for smaller magnitude of  $V_{gs}$  and at relatively higher magnitude, its profile almost saturates and a further increase may lead to the breakdown of the device. The observed shifting of the  $g_m$  peak towards higher negative  $V_{gs}$  values is against this principle and therefore, difficult to explain by Shockley square law expression.

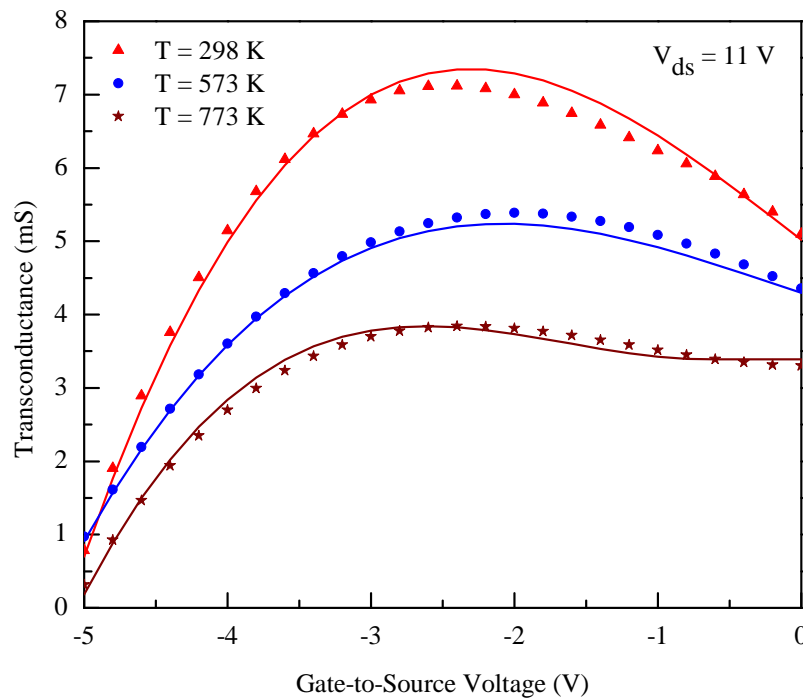


FIGURE 5.4: Variation in transconductance as a function of temperature of a  $0.12 \mu\text{m}$  gate length GaN HEMT. Lines indicate simulated results whilst symbols show experimental transconductance.

A plausible explanation of the shifting of the  $g_m$  peak towards a relatively higher negative gate bias could be that at  $V_{gs} = 0 \text{ V}$  and  $V_{ds} \geq V_{ds(\text{sat})}$ , a contact is in making between the depletion and 2-DEG of the device. It is assumed that this contact is so small that its control on the drifting carriers of 2-DEG is relatively weak. With increasing  $V_{gs}$ , the depletion penetration into 2-DEG increases, which naturally gives the Schottky barrier depletion an efficient control upon the device  $I_{ds}$ ; translating it to improved  $g_m$ . Values of  $V_{gs}$  where the gate depletion gets effective control upon  $I_{ds}$  will define a peak value of  $g_m$ . This effect is addressed in the proposed model and owing to that the performance of the proposed model is relatively better than the other models listed in Table 5.7.

Table 5.8 represents a comparative analysis of different numerical models to predict the transfer characteristics of GaN HEMTs as a function of temperature. It is obvious from the data of the table that the proposed technique offers improved performance at various temperatures under consideration. At  $T = 298 \text{ K}$ , the observed improvement is  $\sim 25\%$  relative to the second best model, i.e. Curtice

TABLE 5.8: Temperature dependent RMS errors in transfer characteristics of different numerical models at  $V_{ds} = 11$  V for a  $0.12 \mu\text{m}$  gate length GaN HEMT [155]. Lowest RMSE are shown in bold.

Model	T = 298 K	T = 573 K	T = 773 K
Angelov [103]	0.475	0.317	0.484
Curtice [101]	0.235	0.153	0.176
McCamant [102]	0.323	0.155	0.248
Dobes [104]	0.380	0.159	0.247
Islam [105]	0.742	0.395	0.449
Riaz [106]	0.252	0.191	0.212
<b>Proposed</b>	<b>0.177</b>	<b>0.127</b>	<b>0.135</b>

model, and at  $T = 573$  K and  $T = 773$  K, the improvement exhibited by the proposed technique was  $\sim 17\%$  and  $\sim 23\%$ , respectively.

Another important feature ought to be addressed in GaN HEMT while simulating its characteristics is the presence of positive/negative  $g_d$  in the saturation region of operation. The nature of  $g_d$  for the devices under discussion is summarized in Fig. 5.5. The  $y$ -axis is divided into two portion: a) positive conductance region and b) negative conductance region. Each ( $\bullet$ ) of the plot is representing the slope of a device at  $V_{gs} = 0$  V. It is obvious from the plot that the devices offering relatively higher power have negative  $g_d$  whilst those devices having relatively lower output power, their  $g_d$  is positive at  $V_{gs} = 0$  V and  $V_{ds} \geq V_{ds(\text{sat})}$ . In conventional CAD models this feature is not fully addressed, resulting into a relatively poor simulation accuracy. We tried to accommodate this affect by defining a term in Eq. (5.4), which simulate the dependence of  $g_d$  both on  $V_{gs}$  and  $V_{ds}$ . This made the proposed model more versatile and suitable for CAD software.

## 5.4 Summary

In this chapter, a non-linear model is proposed to simulate the DC characteristics of submicron GaN HEMTs. The model takes into account dependence of

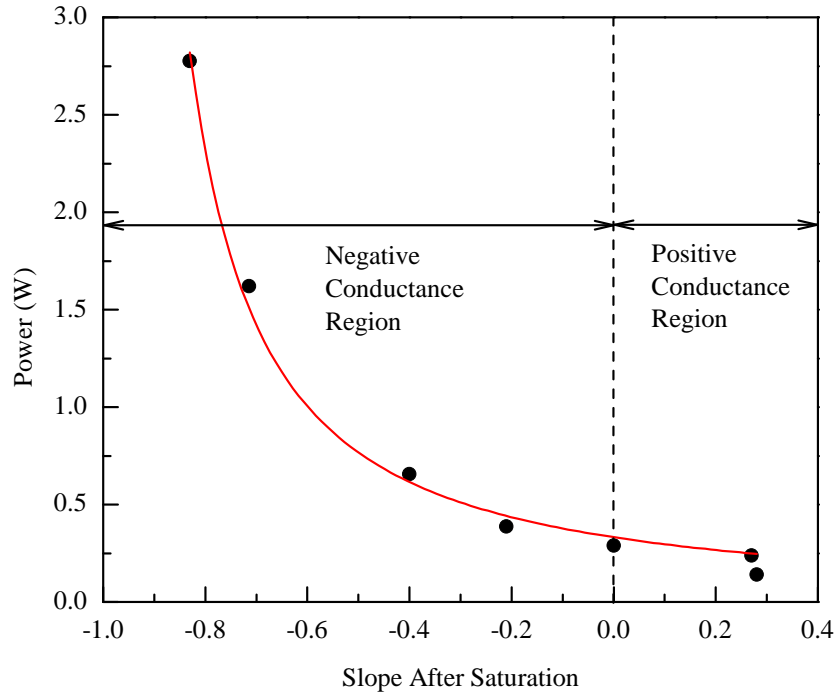


FIGURE 5.5: Slope of  $I - V$  curves of GaN HEMTs and associated power after the onset of saturation at  $V_{gs} = 0$  V.

output conductance on the device drain and gate bias and simulates both positive and negative conductance to a good degree of accuracy. Appearance of peak transconductance to a relatively higher negative gate bias is a frequently observed phenomenon in GaN HEMTs, and the proposed model has the ability to simulate such characteristics with improved accuracy. To check the validity of the proposed model, a comparative study is carried out by selected devices of varying lengths and widths. The proposed model, in predicting the output characteristics of submicron GaN HEMTs, exhibited improvement in root means square errors from 17% to 50%, relative to other such models reported in literature. The accuracy of the model is also checked at elevated temperature i.e. up to 773 K and was found significantly better than its counterparts. As, the proposed model is based on a single expression, it is therefore easy to handle with and can comfortably be used in computer aided design software to assess the temperature dependent performance of GaN HEMTs for their possible integration into power circuitries.

# Chapter 6

## Conclusion and Future Work

This thesis discusses the 3<sup>rd</sup> generation wide bandgap semiconductors (SiC and GaN) and their potential use in microelectronic industry. At high power and in harsh environment, deterioration in a semiconductor device characteristics is a natural phenomenon and the same has been dually emphasized in this thesis. However, it is also discussed that GaN HEMTs have higher resilience to these changes, because of high thermal conductivity and wide bandgap nature of the device material.

The intrinsic carrier concentration ( $n_i$ ) of a semiconductor material is a temperature-dependent parameter. As temperature increases, so does the carrier generation rate. For GaN semiconductor, the dependence of  $n_i$  on temperature is five times weaker than for Si, making devices more robust for high-temperature operation. Therefore, the low  $n_i$  at high temperature coupled with the high breakdown field due to the wide bandgap make GaN-based devices highly suitable for use in elevated-temperature applications.

Wide bandgap devices such as GaN HEMTs have proven to be superior to their counterparts due to their relatively: (a) high carriers mobility, (b) high saturation velocity and (c) high breakdown voltage, making them preferred candidates for use in high-temperature applications in the microwave regime. To achieve increased drain current, high sheet charge concentration ( $n_s$ ) is required. Use of an



AlGa<sub>N</sub>/Ga<sub>N</sub> heterojunction in HEMTs results in a relatively high value of  $n_s$  in the form of a 2-DEG, enabling the device to provide high drain current for given bias.

In addition to the superior and well-controlled material characteristics of AlGa<sub>N</sub>/Ga<sub>N</sub> HEMTs, the characteristics of such devices can be further improved by optimizing fabrication parameters, one of the most important of which is the quality of the device Schottky barrier junction ( $\phi_b$ ), which is also sensitive to temperature. By their very design, AlGa<sub>N</sub>/Ga<sub>N</sub> HEMTs are meant to be operated at relatively high bias, which can result in modification of  $\phi_b$ . Such a modification has direct impact on the device output current, rendering the characteristics of the device temperature dependent.

It is an established fact that carriers mobility is sensitive to lattice temperature. In general, at high bias, the strength of the electric field underneath the Schottky barrier causes the lattice temperature to rise. The lattice temperature also rises when the device is operated in harsh environment. At elevated temperature, the lattice vibrates with increased amplitude, thus offering a greater obstacle to flow of free carriers; resulting into reduced carrier mobility.

The characteristics of a HEMT device are primarily determined by  $n_s$ , which is mainly dependent on the bandgap discontinuity ( $\Delta E_c$ ), determined by the layer structure of the HEMT. The position of the Fermi level ( $E_F$ ), which is also a temperature-dependent parameter, determines the  $n_s$  available in the layer structure of the device, which can possibly tunnel to the quantum states at the interface of the layers defining the 2-DEG. Therefore, any variation in the temperature will cause a change in  $E_F$ , eventually translating into a change in  $n_s$ .

For improved device understanding, especially at elevated temperature and at high bias, it is important that all aforementioned variables be considered while developing a Ga<sub>N</sub> HEMT model. In this research, as a first part, an analytical model has been developed to predict the temperature dependent  $I - V$  characteristics of AlGa<sub>N</sub>/Ga<sub>N</sub> HEMTs. The developed model incorporated the temperature-dependent variation in the Schottky barrier height,  $\phi_b(T)$ , bandgap discontinuity,

$\Delta E_c(T)$ , sheet carrier concentration of 2-DEG,  $n_s(T)$ , saturation velocity,  $v_{sat}(T)$ , and carrier mobility,  $\mu(T)$ . It has been demonstrated that, with increasing ambient temperature, there was a decrease in  $\phi_b$ , an increase in  $n_s$ , a decrease in the  $v_{sat}$  of 2-DEG carriers, and a decrease in  $\mu_T$ . The degradation in the  $I-V$  characteristics of AlGaIn/GaN HEMTs at elevated temperature was accurately modeled. It is demonstrated that the deterioration in the device performance is primarily associated with reduced  $\mu_T$  and  $v_{sat}$ . The developed model results were compared with other reported models intended for prediction of temperature-dependent  $I-V$  characteristics. RMSE values indicated that the developed model can simulate the temperature-dependent  $I-V$  characteristics of GaN HEMTs with at least 39% improved accuracy.

Apart from power applications, GaN HEMT is also a promising competitor for high frequency operations due to its relatively high saturation velocity. Moreover, the piezoelectric and spontaneous polarization effects present in GaN HEMTs result in a high density 2-DEG at the AlGaIn/GaN hetero-interface. Allowing an AlGaIn/GaN HEMT to maintain much higher current density than other III-V group HEMTs. Contrary to earlier reported data, our study showed that as the temperature increases, the generation of  $n_s$  also increases, which effectively controls the channel current and thus, the device performance. So an accurate charge control model to assess  $n_s$  is needed, encompassing all the temperature dependent physical parameters of the device.

It is an established fact that change in temperature causes a change in the AC performance of the device so, an accurate knowledge of temperature dependent AC performance of the device is essential for its optimal use, especially in harsh environments. Different AC models have been developed so far to predict the temperature based performance of the device but, either they are too complex to handle or their accuracy deteriorates with increasing values of temperature.

For microwave applications, gate length of the device is reduced to submicron regime, which affects the device channel conditions, and as a result there is a considerable rise in the channel temperature which modifies the device characteristics.

These effects are frequently observed in submicron devices where the field underneath the Schottky barrier reaches  $\sim 10^6 \text{cm}^{-1}$ . Thus, channel heating effects are more pronounced for the devices having smaller dimensions but with relatively high drain current to meet specific power requirements.

There is no global mechanism which can be employed to assess the channel temperature due to self-heating because, it is device geometry dependent and therefore, it will vary from device to device. Dependence of GaN HEMT performance on numerous parameters requires a compact model to simulate the device characteristics both at room as well as at elevated temperature. A compact device model would be the one which can predict  $I_{ds}$  as a function of  $V_{ds}$  and  $V_{gs}$  bias. It should adequately address the influence of ambient temperature and self-heating on the device characteristics. Moreover, the model should also explain changes in  $I_{ds}$  with varying device physical parameters; such as gate length, gate width, threshold voltage and  $n_s$  etc. It should also have the flexibility to be employed in simulation software, to extend the device knowledge into circuits involving GaN HEMTs.

As a second part of this research work, we have developed a technique, which predicts temperature dependent AC parameters of submicron GaN HEMTs using DC characteristics. The technique by employing the device physical parameters generates, initially, the DC characteristics, and once a good degree of accuracy is achieved between the modeled and the observed DC characteristics, AC small signal parameters of the devices are then assessed. In the proposed technique, a relatively simplified approach is adopted to evaluate  $n_s(T)$  of a HEMT. Ambient and self-heating effects are incorporated in  $n_s(T)$  and in other parameters for the improved assessment of the device characteristics. Modeled DC data is then engaged to predict intrinsic AC parameters of the device. Validity of the proposed technique is established using experimental data of AlGaIn/GaN HEMTs at varying temperatures. The technique was further extended and S-parameters of GaN HEMTs were calculated by using assessed AC small signal parameters. Assessed and the experimental S-parameters were compared and a good degree of accuracy

was demonstrated to ensure the validity of the developed technique. The technique, thus developed could be used as a tool to assess temperature dependent intrinsic AC parameters of GaN HEMTs.

There are very few models reported in literature, which can simulate GaN HEMT characteristics for power related applications. Physics based models are too complicated to be employed in a circuit simulation software. Semi-physics or numerical techniques are usually used to predict fundamental characteristics of the device in computer aided design (CAD). Numerical models developed for GaAs MESFETs are being used to simulate  $I - V$  characteristic of GaN HEMTs. GaAs MESFETs models are bound to lose their accuracy when the device characteristics exhibit noticeable self-heating effects. It is, therefore, pertinent to have a numerical model for GaN HEMTs which can simulate the  $I - V$  characteristics as a function of  $V_{ds}$  and  $V_{gs}$ , with a good degree of accuracy, and the model should be compact enough to be employed in CAD.

As a third part in this research, an attempt has been made to develop a compact model for submicron GaN HEMTs and to assess its accuracy comparative to other such models reported in literature. In this respect, a non-linear single expression based model is developed to simulate the DC characteristics of GaN HEMTs. The model takes into account dependence of output conductance on  $V_{ds}$  and  $V_{gs}$  and simulates both positive and negative conductance to a good degree of accuracy. Appearance of peak transconductance to a relatively higher negative gate bias is a routinely observed phenomenon in GaN HEMTs, and the proposed model has the ability to simulate such characteristics with improved accuracy. To check the validity of the proposed model, a comparative study is carried out by selected devices of varying lengths and widths. It has been established that the proposed model offers at 17% improved performance for the output characteristics of GaN HEMTs relative to other such models reported in literature. The accuracy of the model is also checked at elevated temperature and was found significantly better than its counterparts. As, the proposed model is based on a single expression, it is therefore easy to handle with and can comfortably be used in CAD software to

assess the temperature dependent performance of GaN HEMTs for their possible integration into power circuitries.

## 6.1 Future Work

GaN HEMT is a futuristic device and it is assumed that it will stay in the industry for decades to come. It has the ability to handle high power and frequency both collectively and individually. Therefore, its potential in industrial applications is phenomenal. To extend this work further, based on the understanding developed in this research, following suggestions are proposed:

1. Degradation in the device performance at elevated temperature is primarily associated with temperature dependent mobility,  $\mu_T$ , which is assumed to be reducing with increasing values of temperature. It would be fundamentally very valuable contribution to split the drain current density,  $J_d$  into two components i.e.  $J_d = J_{d1} + J_{d2}$ ; such that  $J_{d1} = qEn_{s1}\mu_{T1}$  and  $J_{d2} = qEn_{s2}\mu_{T2}$ , where  $n_{s1}$  represents carriers having mobility  $\mu_{T1}$  and defines current  $J_{d1}$ , and  $n_{s2}$  represents carriers having mobility  $\mu_{T2}$ , and defines current  $J_{d2}$ . Such a split could possibly facilitate in understanding the basic cause of negative conductance in the saturation region of operation, which eventually dies down with increasing values of  $V_{gs}$ . If it could be established that  $n_s = n_{s1} + n_{s2}$ , where  $n_{s1}$  and  $n_{s2}$  are bias dependent, then another possible cause of negative output conductance, which is not considered in this thesis, could be the reduction in  $\mu_T$  due to changed quantized locations of corresponding carriers. In that case, it would be the electron population controlled phenomenon, in a given quantized state, rather something associated entirely with the lattice vibration.
2. Shift of  $g_m$  peak towards higher negative  $V_{gs}$ , which is considered an adverse effect in the device performance could possibly be avoided by tailoring the 2-DEG layer of the device and the quality of the Schottky barrier with the

surety that there does not exist any parasitic FET. Experimentation in this respect may be carried out by designing devices with etch stop layer and controlling the surface state density of the Schottky barrier to assess the cause of this shift; originated either from the layer structure or an intrinsic nature of the device which could be associated with other parameters such as  $n_s$  etc.

3. Evaluation of GaN HEMT  $n_s$  variation because of the impact ionization and its subsequent effect on the device  $J_d$  would be another interesting research avenue which can be pursued.
4. In our numerical model we have proposed a single non-linear expression to simulate  $I-V$  characteristics of the device both at room as well as at elevated temperature. This work can be further extended to develop AC model of the device on similar approach for its comprehensive utility in CAD.
5. The developed numerical model could be extended to incorporate breakdown region of operation of the device; to enable a designer to study the reliability of the device under extreme scenario.
6. Finally, it is also suggested that the analytical model developed in this thesis could take into account substrate trapping effects, which could be a significant contributory factor at elevated temperature. These effects might be investigated for the completeness of the model.

# Bibliography

- [1] R. K. Baruah and R. P. Paily, “High-temperature effects on device performance of a junctionless transistor,” in *Emerging Electronics (ICEE), 2012 International Conference on*. IEEE, 2012, pp. 1–4.
- [2] J. Millan, P. Godignon, X. Perpina, A. Pérez-Tomás, and J. Rebollo, “A survey of wide bandgap power semiconductor devices,” *IEEE Transactions on Power Electronics*, vol. 29, no. 5, pp. 2155–2163, 2014.
- [3] B. Ozpineci and L. M. Tolbert, *Comparison of wide-bandgap semiconductors for power electronics applications*. United States. Department of Energy, 2004.
- [4] L. Łukasiak and A. Jakubowski, “History of semiconductors,” *Journal of Telecommunications and Information Technology*, pp. 3–9, 2010.
- [5] F. Medjdoub, N. Waldhoff, M. Zegaoui, B. Grimbert, N. Rolland, and P. Rolland, “Low-noise microwave performance of AlN/GaN HEMTs grown on silicon substrate,” *IEEE Electron Device Letters*, vol. 32, no. 9, pp. 1230–1232, 2011.
- [6] R. S. Pengelly, S. M. Wood, J. W. Milligan, S. T. Sheppard, and W. L. Pribble, “A review of GaN on SiC high electron-mobility power transistors and MMICs,” *IEEE Transactions on Microwave Theory and Techniques*, vol. 60, no. 6, pp. 1764–1783, 2012.
- [7] M. Willander, M. Friesel, Q.-u. Wahab, and B. Straumal, “Silicon carbide and diamond for high temperature device applications,” *Journal of Materials Science: Materials in Electronics*, vol. 17, no. 1, pp. 1–25, 2006.

- 
- [8] S. A. Eliza, “Modeling of AlGaN/GaN high electron mobility transistor for sensors and high-temperature circuit applications,” PhD Dissertation 2008.
- [9] U. K. Mishra, P. Parikh, and Y.-F. Wu, “AlGaN/GaN HEMTs—an overview of device operation and applications,” *Proceedings of the IEEE*, vol. 90, no. 6, pp. 1022–1031, 2002.
- [10] A. Lebedev and V. Chelnokov, “Wide-gap semiconductors for high-power electronics,” *Semiconductors*, vol. 33, no. 9, pp. 999–1001, 1999.
- [11] E. Johnson, “Physical limitations on frequency and power parameters of transistors (Performance limits of transistor set by product of dielectric breakdown voltage and minority-carrier saturated drift velocity),” *RCA Review*, vol. 26, pp. 163–177, 1965.
- [12] B. Baliga, “Semiconductors for high-voltage, vertical channel field-effect transistors,” *Journal of Applied Physics*, vol. 53, no. 3, pp. 1759–1764, 1982.
- [13] C. Hu, *Modern semiconductor devices for integrated circuits*. Prentice Hall, 2010.
- [14] M. Asif Khan, J. Kuznia, D. Olson, W. Schaff, J. Burm, and M. Shur, “Microwave performance of a 0.25  $\mu\text{m}$  gate AlGaN/GaN heterostructure field effect transistor,” *Applied Physics Letters*, vol. 65, no. 9, pp. 1121–1123, 1994.
- [15] M. Guz, D. Sanderlin, B. H. Sin, M. de Rooij, T. McDonald, P. Le, A. Young, M. Seeman, and J. Walker, “IEEE ITRW working group position paper—system integration and application: Gallium Nitride: Identifying and addressing challenges to realize the full potential of GaN in power conversion applications,” *IEEE Power Electronics Magazine*, vol. 5, no. 2, pp. 34–39, 2018.
- [16] R. Lossy, N. Chaturvedi, P. Heymann, J. Würfl, S. Müller, and K. Köhler, “Large area AlGaN/GaN HEMTs grown on insulating silicon carbide substrates,” *Physica Status Solidi (A)*, vol. 194, no. 2, pp. 460–463, 2002.



- [17] M. Huque, S. Eliza, T. Rahman, H. Huq, and S. Islam, “Temperature dependent analytical model for current–voltage characteristics of AlGa<sub>N</sub>/Ga<sub>N</sub> power HEMT,” *Solid-State Electronics*, vol. 53, no. 3, pp. 341–348, 2009.
- [18] H. Xiao-Guang, Z. De-Gang, and J. De-Sheng, “Formation of two-dimensional electron gas at AlGa<sub>N</sub>/Ga<sub>N</sub> heterostructure and the derivation of its sheet density expression,” *Chinese Physics B*, vol. 24, no. 6, pp. 1–6, 2015.
- [19] D. A. Neamen *et al.*, *Semiconductor physics and devices*. McGraw-Hill New York, 1997, vol. 3.
- [20] C. S. Chang and H. R. Fetterman, “An analytic model for high-electron-mobility transistors,” *Solid-State Electronics*, vol. 30, no. 5, pp. 485–491, 1987.
- [21] K. Lee, M. S. Shur, T. Drummond, and H. Morkoc, “Current-voltage and capacitance-voltage characteristics of modulation-doped field-effect transistors,” *IEEE Transactions on Electron Devices*, vol. 30, no. 3, pp. 207–212, 1983.
- [22] M. K. Chattopadhyay and S. Tokekar, “Thermal model for DC characteristics of AlGa<sub>N</sub>/Ga<sub>N</sub> HEMTs including self-heating effect and non-linear polarization,” *Microelectronics Journal*, vol. 39, no. 10, pp. 1181–1188, 2008.
- [23] M. A. Alim, A. A. Rezazadeh, and C. Gaquiere, “Temperature effect on DC and equivalent circuit parameters of 0.15  $\mu\text{m}$  gate length Ga<sub>N</sub>/SiC HEMT for microwave applications,” *IEEE Transactions on Microwave Theory and Techniques*, vol. 64, no. 11, pp. 3483–3491, 2016.
- [24] —, “Small signal model parameters analysis of Ga<sub>N</sub> and GaAs based HEMTs over temperature for microwave applications,” *Solid-State Electronics*, vol. 119, pp. 11–18, 2016.
- [25] X. Wang, G. Hu, Z. Ma, J. Ran, C. Wang, H. Xiao, J. Tang, J. Li, J. Wang, Y. Zeng *et al.*, “AlGa<sub>N</sub>/Al<sub>N</sub>/Ga<sub>N</sub>/SiC HEMT structure with high mobility

- GaN thin layer as channel grown by MOCVD,” *Journal of Crystal Growth*, vol. 298, pp. 835–839, 2007.
- [26] U. K. Mishra, L. Shen, T. E. Kazior, and Y.-F. Wu, “GaN-based RF power devices and amplifiers,” *Proceedings of the IEEE*, vol. 96, no. 2, pp. 287–305, 2008.
- [27] Z. Fan, M. Nakarmi, J. Lin, and H. Jiang, “Delta-doped AlGaIn/GaN heterostructure field-effect transistors with incorporation of AlN epilayers,” *MRS Online Proceedings Library Archive*, vol. 798, 2003.
- [28] T. Kikkawa, K. Imanishi, M. Kanamura, and K. Joshin, “Recent progress of highly reliable GaN-HEMT for mass production,” in *CS MANTECH Conference*, 2006, pp. 171–174.
- [29] L. Shen, R. Coffie, D. Buttari, S. Heikman, A. Chakraborty, A. Chini, S. Keller, S. DenBaars, and U. Mishra, “High-power polarization-engineered GaN/AlGaIn/GaN HEMTs without surface passivation,” *IEEE Electron Device Letters*, vol. 25, no. 1, pp. 7–9, 2004.
- [30] A. Koudymov, V. Adivarahan, J. Yang, G. Simin, and M. A. Khan, “Mechanism of current collapse removal in field-plated nitride HFETs,” *IEEE Electron Device Letters*, vol. 26, no. 10, pp. 704–706, 2005.
- [31] O. Ambacher, J. Smart, J. Shealy, N. Weimann, K. Chu, M. Murphy, W. Schaff, L. Eastman, R. Dimitrov, L. Wittmer *et al.*, “Two-dimensional electron gases induced by spontaneous and piezoelectric polarization charges in N- and Ga-face AlGaIn/GaN heterostructures,” *Journal of Applied Physics*, vol. 85, no. 6, pp. 3222–3233, 1999.
- [32] O. Ambacher, B. Foutz, J. Smart, J. Shealy, N. Weimann, K. Chu, M. Murphy, A. Sierakowski, W. Schaff, L. Eastman *et al.*, “Two dimensional electron gases induced by spontaneous and piezoelectric polarization in undoped and doped AlGaIn/GaN heterostructures,” *Journal of Applied Physics*, vol. 87, no. 1, pp. 334–344, 2000.

- [33] Q. Guo and A. Yoshida, "Temperature dependence of band gap change in InN and AlN," *Japanese Journal of Applied Physics*, vol. 33, no. 5R, pp. 2453–2456, 1994.
- [34] I. Vurgaftman, J. Meyer, and L. Ram-Mohan, "Band parameters for III–V compound semiconductors and their alloys," *Journal of Applied Physics*, vol. 89, no. 11, pp. 5815–5875, 2001.
- [35] X. Dang, P. Asbeck, E. Yu, G. Sullivan, M. Chen, B. McDermott, K. Boutros, and J. Redwing, "Measurement of drift mobility in AlGaIn/GaN heterostructure field-effect transistor," *Applied Physics Letters*, vol. 74, no. 25, pp. 3890–3892, 1999.
- [36] S. E. A. Hosseini and S. E. Hosseini, "Accurate analytical model for current–voltage and small-signal characteristics of  $\text{Al}_m\text{Ga}_{1-m}\text{N}/\text{GaN}$  modulation-doped field-effect transistors," *Japanese Journal of Applied Physics*, vol. 49, no. 7R, pp. 1–6, 2010.
- [37] A. Stocco, "Reliability and failure mechanisms of gan hemt devices suitable for high-frequency and high-power applications," PhD Dissertation 2012.
- [38] A. A. Fletcher and D. Nirmal, "A survey of gallium nitride HEMT for RF and high power applications," *Superlattices and Microstructures*, vol. 109, pp. 519–537, 2017.
- [39] D. Maier, M. Alomari, N. Grandjean, J.-F. Carlin, M.-A. Diforte-Poisson, C. Dua, A. Chuvilin, D. Troadec, C. Gaquière, U. Kaiser *et al.*, "Testing the temperature limits of GaN-based HEMT devices," *IEEE Transactions on Device and Materials Reliability*, vol. 10, no. 4, pp. 427–436, 2010.
- [40] P. Moens, A. Banerjee, M. Uren, M. Meneghini, S. Karboyan, I. Chatterjee, P. Vanmeerbeek, M. Cäsar, C. Liu, A. Salih *et al.*, "Impact of buffer leakage on intrinsic reliability of 650V AlGaIn/GaN HEMTs," in *2015 IEEE International Electron Devices Meeting (IEDM)*. IEEE, 2015, pp. 35.2.1–35.2.4.

- [41] G. Meneghesso, M. Meneghini, I. Rossetto, D. Bisi, S. Stoffels, M. Van Hove, S. Decoutere, and E. Zanoni, "Reliability and parasitic issues in GaN-based power HEMTs: A review," *Semiconductor Science and Technology*, vol. 31, no. 9, pp. 1–10, 2016.
- [42] J. Gao, *RF and microwave modeling and measurement techniques for field effect transistors*. SciTec, PhD Dissertation 2010.
- [43] L. M. Tolbert, B. Ozpineci, S. K. Islam, and M. S. Chinthavali, "Wide bandgap semiconductors for utility applications," *Semiconductors*, vol. 1, pp. 1–5, 2003.
- [44] J. Millán, P. Godignon, and A. Pérez-Tomás, "Wide band gap semiconductor devices for power electronics," *Automatika: časopis za Automatiku, Mjerenje, Elektroniku, Računarstvo i Komunikacije*, vol. 53, no. 2, pp. 107–116, 2012.
- [45] J. Hostetler, P. Alexandrov, X. Li, L. Fursin, and A. Bhalla, "6.5 kV SiC normally-off JFETs technology status," in *2014 IEEE Workshop on Wide Bandgap Power Devices and Applications (WiPDA)*. IEEE, 2014, pp. 143–146.
- [46] F. Iacopi, M. Van Hove, M. Charles, and K. Endo, "Power electronics with wide bandgap materials: Toward greener, more efficient technologies," *MRS Bulletin*, vol. 40, no. 5, pp. 390–395, 2015.
- [47] K. Li, P. Evans, and M. Johnson, "SiC/GaN power semiconductor devices theoretical comparison and experimental evaluation," in *2016 IEEE Vehicle Power and Propulsion Conference (VPPC)*. IEEE, 2016, pp. 1–6.
- [48] W. C. Johnson, J. Parson, and M. Crew, "Nitrogen compounds of gallium. III," *The Journal of Physical Chemistry*, vol. 36, no. 10, pp. 2651–2654, 1932.

- [49] R. Juza and H. Hahn, "Über die kristallstrukturen von  $\text{Cu}_3\text{N}$ , GaN und InN metallamide und metallnitride," *Zeitschrift für Anorganische und Allgemeine Chemie*, vol. 239, no. 3, pp. 282–287, 1938.
- [50] H. á. Maruska and J. Tietjen, "The preparation and properties of vapor-deposited single-crystal-line GaN," *Applied Physics Letters*, vol. 15, no. 10, pp. 327–329, 1969.
- [51] M. A. Khan, J. Van Hove, J. Kuznia, and D. Olson, "High electron mobility GaN/ $\text{Al}_x\text{Ga}_{1-x}\text{N}$  heterostructures grown by low-pressure metalorganic chemical vapor deposition," *Applied Physics Letters*, vol. 58, no. 21, pp. 2408–2410, 1991.
- [52] M. Asif Khan, A. Bhattarai, J. Kuznia, and D. Olson, "High electron mobility transistor based on a GaN- $\text{Al}_x\text{Ga}_{1-x}\text{N}$  heterojunction," *Applied Physics Letters*, vol. 63, no. 9, pp. 1214–1215, 1993.
- [53] A. Bykhovski, B. Gelmont, and M. Shur, "The influence of the strain-induced electric field on the charge distribution in GaN-AlN-GaN structure," *Journal of Applied Physics*, vol. 74, no. 11, pp. 6734–6739, 1993.
- [54] A. Ozgur, W. Kim, Z. Fan, A. Botchkarev, A. Salvador, S. Mohammad, B. Sverdlov, and H. Morkoc, "High transconductance normally-off GaN MODFETs," *Electronics Letters*, vol. 31, no. 16, pp. 1389–1390, 1995.
- [55] P. Asbeck, E. Yu, S. Lau, G. Sullivan, J. Van Hove, and J. Redwing, "Piezoelectric charge densities in AlGaN/GaN HFETs," *Electronics Letters*, vol. 33, no. 14, pp. 1230–1231, 1997.
- [56] F. Ren, M. Hong, S. Chu, M. Marcus, M. Schurman, A. Baca, S. Pearton, and C. Abernathy, "Effect of temperature on  $\text{Ga}_2\text{O}_3(\text{Gd}_2\text{O}_3)/\text{GaN}$  metal-oxide-semiconductor field-effect transistors," *Applied Physics Letters*, vol. 73, no. 26, pp. 3893–3895, 1998.

- [57] Y.-F. Wu, B. Keller, P. Fini, S. Keller, T. Jenkins, L. Kehias, S. Denbaars, and U. Mishra, "High Al-content AlGa<sub>N</sub>/Ga<sub>N</sub> MODFETs for ultrahigh performance," *IEEE Electron Device Letters*, vol. 19, no. 2, pp. 50–53, 1998.
- [58] S. Yoshida and J. Suzuki, "High-temperature reliability of Ga<sub>N</sub> metal semiconductor field-effect transistor and bipolar junction transistor," *Journal of Applied Physics*, vol. 85, no. 11, pp. 7931–7934, 1999.
- [59] A. Zhang, G. Dang, F. Ren, J. Han, A. Baca, R. Shul, H. Cho, C. Monier, X. Cao, C. Abernathy *et al.*, "Direct-current characteristics of pnp AlGa<sub>N</sub>/Ga<sub>N</sub> heterojunction bipolar transistors," *Applied Physics Letters*, vol. 76, no. 20, pp. 2943–2945, 2000.
- [60] F. Semond, P. Lorenzini, N. Grandjean, and J. Massies, "High-electron-mobility AlGa<sub>N</sub>/Ga<sub>N</sub> heterostructures grown on Si (111) by molecular-beam epitaxy," *Applied Physics Letters*, vol. 78, no. 3, pp. 335–337, 2001.
- [61] Y. Cai, Y. Zhou, K. M. Lau, and K. J. Chen, "Control of threshold voltage of AlGa<sub>N</sub>/Ga<sub>N</sub> HEMTs by fluoride-based plasma treatment: From depletion mode to enhancement mode," *IEEE Transactions on Electron Devices*, vol. 53, no. 9, pp. 2207–2215, 2006.
- [62] Y. Uemoto, M. Hikita, H. Ueno, H. Matsuo, H. Ishida, M. Yanagihara, T. Ueda, T. Tanaka, and D. Ueda, "Gate injection transistor (GIT): A normally-off AlGa<sub>N</sub>/Ga<sub>N</sub> power transistor using conductivity modulation," *IEEE Transactions on Electron Devices*, vol. 54, no. 12, pp. 3393–3399, 2007.
- [63] S. Tripathy, V. K. Lin, S. B. Dolmanan, J. P. Tan, R. Kajen, L. K. Bera, S. L. Teo, M. K. Kumar, S. Arulkumaran, G. I. Ng *et al.*, "AlGa<sub>N</sub>/Ga<sub>N</sub> two-dimensional-electron gas heterostructures on 200 mm diameter Si (111)," *Applied Physics Letters*, vol. 101, no. 8, pp. 1–5, 2012.
- [64] Y. Zhang, M. Sun, S. J. Joglekar, T. Fujishima, and T. Palacios, "Threshold voltage control by gate oxide thickness in fluorinated Ga<sub>N</sub> metal-oxide-semiconductor high-electron-mobility transistors," *Applied Physics Letters*, vol. 103, no. 3, pp. 1–5, 2013.

- [65] K. Boutros, M. Regan, P. Rowell, D. Gotthold, R. Birkhahn, and B. Brar, "High performance GaN HEMTs at 40 GHz with power density of 2.8 W/mm," in *IEEE International Electron Devices Meeting (IEDM'03) Technical Digest*. IEEE, 2003, pp. 12.5.1–12.5.2.
- [66] M. Akita, S. Kishimoto, and T. Mizutani, "High-frequency measurements of AlGaN/GaN HEMTs at high temperatures," *IEEE Electron Device Letters*, vol. 22, no. 8, pp. 376–377, 2001.
- [67] S. Nuttinck, B. Banerjee, S. Venkataraman, J. Laskar, and M. Harris, "High temperature performances of AlGaN/GaN power HFETs," in *2003 IEEE MTT-S International Microwave Symposium Digest*, vol. 1. IEEE, 2003, pp. 221–223.
- [68] T. Palacios, A. Chakraborty, S. Rajan, C. Poblenz, S. Keller, S. DenBaars, J. Speck, and U. Mishra, "High-power AlGaN/GaN HEMTs for Ka-band applications," *IEEE Electron Device Letters*, vol. 26, no. 11, pp. 781–783, 2005.
- [69] M. Micovic, A. Kurdoghlian, P. Hashimoto, M. Hu, M. Antcliffe, P. Willadsen, W. Wong, R. Bowen, I. Milosavljevic, A. Schmitz *et al.*, "GaN HFET for W-band power applications," in *International Electron Devices Meeting (IEDM'06)*. IEEE, 2006, pp. 1–3.
- [70] S. Arulkumaran, Z. Liu, G. Ng, W. Cheong, R. Zeng, J. Bu, H. Wang, K. Radhakrishnan, and C. Tan, "Temperature dependent microwave performance of AlGaN/GaN high-electron-mobility transistors on high-resistivity silicon substrate," *Thin Solid Films*, vol. 515, no. 10, pp. 4517–4521, 2007.
- [71] M. Chunlei, G. Guodong, and L. Yuanjie, "A high performance InAlN/GaN HEMT with low  $R_{on}$  and gate leakage," *Journal of Semiconductors*, vol. 37, no. 2, p. 024009, 2016.
- [72] R. Gaska, A. Osinsky, J. Yang, and M. S. Shur, "Self-heating in high-power AlGaIn-GaN HFETs," *IEEE Electron Device Letters*, vol. 19, no. 3, pp. 89–91, 1998.

- [73] I. Ahmad, V. Kasisomayajula, D. Song, L. Tian, J. Berg, and M. Holtz, "Self-heating in a GaN based heterostructure field effect transistor: Ultraviolet and visible Raman measurements and simulations," *Journal of Applied Physics*, vol. 100, no. 11, pp. 1–7, 2006.
- [74] Y.-R. Wu and J. Singh, "Transient study of self-heating effects in AlGaIn/GaN HFETs: Consequence of carrier velocities, temperature, and device performance," *Journal of Applied Physics*, vol. 101, no. 11, pp. 1–5, 2007.
- [75] M. Hosch, J. Pomeroy, A. Sarua, M. Kuball, H. Jung, and H. Schumacher, "Field dependent self-heating effects in high-power AlGaIn/GaN HEMTs," in *CS Mantech Conference*, 2009, pp. 18–21.
- [76] I. Daumiller, C. Kirchner, M. Kamp, K. Ebeling, and E. Kohn, "Evaluation of the temperature stability of AlGaIn/GaN heterostructure FETs," *IEEE Electron Device Letters*, vol. 20, no. 9, pp. 448–450, 1999.
- [77] S. Arulkumaran, T. Egawa, H. Ishikawa, and T. Jimbo, "High-temperature effects of AlGaIn/GaN high-electron-mobility transistors on sapphire and semi-insulating SiC substrates," *Applied Physics Letters*, vol. 80, no. 12, pp. 2186–2188, 2002.
- [78] R. Cuervo, J. Pedrós, A. Navarro, A. Brana, J. Pau, E. Muñoz, and F. Calle, "High temperature assessment of nitride-based devices," *Journal of Materials Science: Materials in Electronics*, vol. 19, no. 2, pp. 189–193, 2008.
- [79] D. Donoval, M. Florovič, D. Gregušová, J. Kováč, and P. Kordoš, "High-temperature performance of AlGaIn/GaN HFETs and MOSHFETs," *Microelectronics Reliability*, vol. 48, no. 10, pp. 1669–1672, 2008.
- [80] M. Florovic, P. Kordos, D. Donoval, D. Gregusova, and J. Kováč, "Performance of AlGaIn/GaN heterostructure field-effect transistors at higher ambient temperatures," *Journal of Electrical Engineering-Bratislava*, vol. 59, no. 1, pp. 53–56, 2008.



- [81] F. Husna, M. Lachab, M. Sultana, V. Adivarahan, Q. Fareed, and A. Khan, "High-Temperature Performance of AlGa<sub>N</sub>/Ga<sub>N</sub> MOSHEMT With SiO<sub>2</sub> Gate Insulator Fabricated on Si (111) Substrate," *IEEE Transactions on Electron Devices*, vol. 59, no. 9, pp. 2424–2429, 2012.
- [82] S. Martin-Horcajo, A. Wang, M.-F. Romero, M. J. Tadjer, and F. Calle, "Simple and accurate method to estimate channel temperature and thermal resistance in AlGa<sub>N</sub>/Ga<sub>N</sub> HEMTs," *IEEE Transactions on Electron Devices*, vol. 60, no. 12, pp. 4105–4111, 2013.
- [83] S. Muhtadi, S. Hwang, A. Coleman, F. Asif, A. Lunev, M. Chandrashekhar, and A. Khan, "High temperature operation of n-AlGa<sub>N</sub> channel metal semiconductor field effect transistors on low-defect AlN templates," *Applied Physics Letters*, vol. 110, no. 19, pp. 1–4, 2017.
- [84] S. S. Islam and A. M. Anwar, "Temperature-dependent nonlinearities in Ga<sub>N</sub>/AlGa<sub>N</sub> HEMTs," *IEEE Transactions on Electron Devices*, vol. 49, no. 5, pp. 710–717, 2002.
- [85] A. Ahmed, S. S. Islam, and A. Anwar, "Frequency and temperature dependence of gain compression in Ga<sub>N</sub>/AlGa<sub>N</sub> HEMT amplifiers," *Solid-State Electronics*, vol. 47, no. 2, pp. 339–344, 2003.
- [86] D. Liu, J. Lee, and W. Lu, "Temperature-dependent microwave noise performances of AlGa<sub>N</sub>/Ga<sub>N</sub> HEMTs with post-gate annealing," *Physica Status Solidi (C)*, vol. 2, no. 7, pp. 2659–2662, 2005.
- [87] T. Palacios, A. Chakraborty, S. Keller, U. K. Mishra *et al.*, "Study of impact of access resistance on high-frequency performance of AlGa<sub>N</sub>/Ga<sub>N</sub> HEMTs by measurements at low temperatures," *IEEE Electron Device Letters*, vol. 27, no. 11, pp. 877–880, 2006.
- [88] M. Thorsell, K. Andersson, M. Fagerlind, M. Sudow, P.-A. Nilsson, and N. Rorsman, "Thermal characterization of the intrinsic noise parameters for AlGa<sub>N</sub>/Ga<sub>N</sub> HEMTs," in *2008 IEEE MTT-S International Microwave Symposium Digest*. IEEE, 2008, pp. 463–466.

- [89] Z. Liu, S. Arulkumaran, and G. Ng, "Temperature dependent microwave noise parameters and modeling of AlGa<sub>N</sub>/Ga<sub>N</sub> HEMTs on Si substrate," in *2009 IEEE MTT-S International Microwave Symposium Digest (MTT'09)*. IEEE, 2009, pp. 777–780.
- [90] A. M. Darwish, A. A. Ibrahim, and H. A. Hung, "Temperature dependence of Ga<sub>N</sub> HEMT small signal parameters," *International Journal of Microwave Science and Technology*, vol. 2011, pp. 1–4, 2011.
- [91] G. Crupi, G. Avolio, A. Raffo, P. Barmuta, D. M.-P. Schreurs, A. Caddemi, and G. Vannini, "Investigation on the thermal behavior of microwave Ga<sub>N</sub> HEMTs," *Solid-State Electronics*, vol. 64, no. 1, pp. 28–33, 2011.
- [92] J.-W. Lee and K. J. Webb, "A temperature-dependent nonlinear analytic model for AlGa<sub>N</sub>-Ga<sub>N</sub> HEMTs on SiC," *IEEE Transactions on Microwave Theory and Techniques*, vol. 52, no. 1, pp. 2–9, 2004.
- [93] Y. Chang, K. Tong, and C. Surya, "Numerical simulation of current–voltage characteristics of AlGa<sub>N</sub>/Ga<sub>N</sub> HEMTs at high temperatures," *Semiconductor Science and Technology*, vol. 20, no. 2, pp. 188–192, 2005.
- [94] H. F. Huq and S. K. Islam, "Effect of temperature variation on the characteristics of microwave power AlGa<sub>N</sub>/Ga<sub>N</sub> MODFET," *International Journal of Infrared and Millimeter Waves*, vol. 26, no. 11, pp. 1501–1512, 2005.
- [95] H. F. Huq, "Temperature dependent analytical modeling, simulation and characterizations of HEMTs in gallium nitride process," PhD Dissertation 2006.
- [96] M. K. Chattopadhyay and S. Tokekar, "Temperature and polarization dependent polynomial based non-linear analytical model for gate capacitance of Al<sub>m</sub>Ga<sub>1-m</sub>N/Ga<sub>N</sub> MODFET," *Solid-State Electronics*, vol. 50, no. 2, pp. 220–227, 2006.
- [97] Y.-H. Wang, Y. C. Liang, G. S. Samudra, T.-F. Chang, C.-F. Huang, L. Yuan, and G.-Q. Lo, "Modelling temperature dependence on AlGa<sub>N</sub>/Ga<sub>N</sub>

- power HEMT device characteristics,” *Semiconductor Science and Technology*, vol. 28, no. 12, pp. 1–10, 2013.
- [98] S. Arulkumaran, G. I. Ng, S. Vicknesh, H. Wang, K. S. Ang, J. P. Y. Tan, V. K. Lin, S. Todd, G.-Q. Lo, and S. Tripathy, “Direct current and microwave characteristics of sub-micron AlGa<sub>N</sub>/Ga<sub>N</sub> high-electron-mobility transistors on 8-inch Si (111) substrate,” *Japanese Journal of Applied Physics*, vol. 51, no. 11R, pp. 1–4, 2012.
- [99] Z. J. Shen, G. Sabui, Z. Miao, and Z. Shuai, “Wide-bandgap solid-state circuit breakers for DC power systems: device and circuit considerations,” *IEEE Transactions on Electron Devices*, vol. 62, no. 2, pp. 294–300, 2015.
- [100] S. Martin-Horcajo, A. Wang, M. Romero, M. Tadjer, A. Koehler, T. Anderson, and F. Calle, “Impact of device geometry at different ambient temperatures on the self-heating of Ga<sub>N</sub>-based HEMTs,” *Semiconductor Science and Technology*, vol. 29, no. 11, pp. 1–9, 2014.
- [101] W. R. Curtice and M. Ettenberg, “A nonlinear GaAs FET model for use in the design of output circuits for power amplifiers,” *IEEE Transactions on Microwave Theory and Techniques*, vol. 33, no. 12, pp. 1383–1394, 1985.
- [102] A. J. McCamant, G. D. McCormack, and D. H. Smith, “An improved GaAs MESFET model for SPICE,” *IEEE Transactions on Microwave Theory and Techniques*, vol. 38, no. 6, pp. 822–824, 1990.
- [103] I. Angelov, N. Rorsman, J. Stenarson, M. Garcia, and H. Zirath, “An empirical table-based FET model,” *IEEE Transactions on Microwave Theory and Techniques*, vol. 47, no. 12, pp. 2350–2357, 1999.
- [104] J. Dobes, “Using modified GaAs FET model function for the accurate representation of PHEMTs and varactors,” in *Proceedings of the 12<sup>th</sup> IEEE Mediterranean Electrotechnical Conference*, vol. 1. IEEE, 2004, pp. 35–38.

- [105] M. Islam and M. Zaman, “A seven-parameter nonlinear  $I - V$  characteristics model for sub- $\mu\text{m}$  range GaAs MESFETs,” *Solid-State Electronics*, vol. 48, no. 7, pp. 1111–1117, 2004.
- [106] M. Riaz, M. M. Ahmed, and U. Munir, “An improved model for current voltage characteristics of submicron SiC MESFETs,” *Solid-State Electronics*, vol. 121, pp. 54–61, 2016.
- [107] H. A. Mantooth, K. Peng, E. Santi, and J. L. Hudgins, “Modeling of wide bandgap power semiconductor devices-Part I,” *IEEE Transactions on Electron Devices*, vol. 62, no. 2, pp. 423–433, 2015.
- [108] E. Santi, K. Peng, H. A. Mantooth, and J. L. Hudgins, “Modeling of wide-bandgap power semiconductor devices-Part II,” *IEEE Transactions on Electron Devices*, vol. 62, no. 2, pp. 434–442, 2015.
- [109] R. Rodríguez, B. González, J. García, F. M. Yigletu, J. M. Tirado, B. Iñiguez, and A. Nunez, “Numerical simulation and compact modelling of AlGa<sub>N</sub>/Ga<sub>N</sub> HEMTs with mitigation of self-heating effects by substrate materials,” *Physica Status Solidi (A)*, vol. 212, no. 5, pp. 1130–1136, 2015.
- [110] K. Jena, R. Swain, and T. R. Lenka, “Modeling and comparative analysis of DC characteristics of AlGa<sub>N</sub>/Ga<sub>N</sub> HEMT and MOSHEMT devices,” *International Journal of Numerical Modelling: Electronic Networks, Devices and Fields*, vol. 29, no. 1, pp. 83–92, 2016.
- [111] W. E. Muhea, F. M. Yigletu, R. Cabré-Rodon, and B. Iñiguez, “Analytical model for Schottky barrier height and threshold voltage of AlGa<sub>N</sub>/Ga<sub>N</sub> HEMTs with piezoelectric effect,” *IEEE Transactions on Electron Devices*, vol. 65, no. 3, pp. 901–907, 2018.
- [112] R. Sun, Y. C. Liang, Y.-C. Yeo, Y.-H. Wang, and C. Zhao, “Design of power integrated circuits in full AlGa<sub>N</sub>/Ga<sub>N</sub> MIS-HEMT configuration for power conversion,” *Physica Status Solidi (A)*, vol. 214, no. 3, pp. 1–9, 2017.

- [113] A. Ahmed, S. S. Islam, and A. Anwar, "A temperature-dependent nonlinear analysis of GaN/AlGa<sub>N</sub> HEMTs using Volterra series," *IEEE Transactions on Microwave Theory and Techniques*, vol. 49, no. 9, pp. 1518–1524, 2001.
- [114] J. Albrecht, R. Wang, P. Ruden, M. Farahmand, and K. Brennan, "Electron transport characteristics of GaN for high temperature device modeling," *Journal of Applied Physics*, vol. 83, no. 9, pp. 4777–4781, 1998.
- [115] D. A. Neaman, *Semiconductor physics and devices*. Irwin Chicago, 1992.
- [116] J. Zolper, "A review of junction field effect transistors for high-temperature and high-power electronics," *Solid-State Electronics*, vol. 42, no. 12, pp. 2153–2156, 1998.
- [117] G. Greco, F. Giannazzo, and F. Roccaforte, "Temperature dependent forward current-voltage characteristics of Ni/Au Schottky contacts on AlGa<sub>N</sub>/Ga<sub>N</sub> heterostructures described by a two diodes model," *Journal of Applied Physics*, vol. 121, no. 4, pp. 1–6, 2017.
- [118] T. Maeda, M. Okada, M. Ueno, Y. Yamamoto, T. Kimoto, M. Horita, and J. Suda, "Temperature dependence of barrier height in Ni/n-GaN Schottky barrier diode," *Applied Physics Express*, vol. 10, no. 5, pp. 1–4, 2017.
- [119] M. M. Ahmed, "Schottky barrier depletion modification-a source of output conductance in submicron GaAs MESFETs," *IEEE Transactions on Electron Devices*, vol. 48, no. 5, pp. 830–834, 2001.
- [120] M. Shur, B. Gelmont, and M. A. Khan, "Electron mobility in two-dimensional electron gas in AlGa<sub>N</sub>/Ga<sub>N</sub> heterostructures and in bulk Ga<sub>N</sub>," *Journal of Electronic Materials*, vol. 25, no. 5, pp. 777–785, 1996.
- [121] N. Shigekawa, K. Shiojima, and T. Suemitsu, "Optical study of high-biased AlGa<sub>N</sub>/Ga<sub>N</sub> high-electron-mobility transistors," *Journal of Applied Physics*, vol. 92, no. 1, pp. 531–535, 2002.

- [122] C. Oxley and M. Uren, “Measurements of unity gain cutoff frequency and saturation velocity of a GaN HEMT transistor,” *IEEE Transactions on Electron Devices*, vol. 52, no. 2, pp. 165–169, 2005.
- [123] A. S. Yalamarthy and D. G. Senesky, “Strain-and temperature-induced effects in AlGa<sub>N</sub>/Ga<sub>N</sub> high electron mobility transistors,” *Semiconductor Science and Technology*, vol. 31, no. 3, pp. 1–10, 2016.
- [124] Y. P. Varshni, “Temperature dependence of the energy gap in semiconductors,” *Physica*, vol. 34, no. 1, pp. 149–154, 1967.
- [125] N. DasGupta and A. DasGupta, “An analytical expression for sheet carrier concentration vs gate voltage for HEMT modelling,” *Solid-State Electronics*, vol. 36, no. 2, pp. 201–203, 1993.
- [126] N. Dasgupta and A. Dasgupta, “A new SPICE MOSFET level 3-like model of HEMT’s for circuit simulation,” *IEEE Transactions on Electron Devices*, vol. 45, no. 7, pp. 1494–1500, 1998.
- [127] C. G. Sodini, P.-K. Ko, and J. L. Moll, “The effect of high fields on MOS device and circuit performance,” *IEEE Transactions on Electron Devices*, vol. 31, no. 10, pp. 1386–1393, 1984.
- [128] F. Schwierz, “An electron mobility model for wurtzite Ga<sub>N</sub>,” *Solid-State Electronics*, vol. 49, no. 6, pp. 889–895, 2005.
- [129] M. Ahmed, M. Riaz, and U. Ahmed, “An improved model for the  $I - V$  characteristics of submicron SiC MESFETs by evaluating the potential distribution inside the channel,” *Journal of Computational Electronics*, vol. 16, no. 3, pp. 514–525, 2017.
- [130] D. Bratton and J. Kennedy, “Defining a standard for particle swarm optimization,” in *2007 IEEE Swarm Intelligence Symposium (SIS)*, 2007, pp. 120–127.
- [131] M. M. Ahmed, H. Ahmed, and P. H. Ladbrooke, “Effects of interface states on submicron GaAs metal–semiconductor field-effect transistors assessed by

- gate leakage current,” *Journal of Vacuum Science & Technology B: Microelectronics and Nanometer Structures Processing, Measurement, and Phenomena*, vol. 13, no. 4, pp. 1519–1525, 1995.
- [132] J. Kuzmik, M. Ľapajna, L. Valik, M. Molnar, D. Donoval, C. Fleury, D. Pogany, G. Strasser, O. Hilt, F. Brunner *et al.*, “Self-heating in GaN transistors designed for high-power operation,” *IEEE Transactions on Electron Devices*, vol. 61, no. 10, pp. 3429–3434, 2014.
- [133] P. H. Ladbrooke, *MMIC Design: GaAs FETs and HEMTs*. Artech House Publishers, 1989.
- [134] M. Khan, U. Ahmed, M. Ahmed, and S. Rehman, “An improved model to assess temperature-dependent DC characteristics of submicron GaN HEMTs,” *Journal of Computational Electronics*, pp. 1–10, 2018.
- [135] A. Zhang, L. Zhang, Z. Tang, X. Cheng, Y. Wang, K. J. Chen, and M. Chan, “Analytical modeling of capacitances for GaN HEMTs, including parasitic components,” *IEEE Transactions on Electron Devices*, vol. 61, no. 3, pp. 755–761, 2014.
- [136] M. Riaz, M. M. Ahmed, U. Rafique, and U. F. Ahmed, “Assessment of intrinsic small signal parameters of submicron SiC MESFETs,” *Solid-State Electronics*, vol. 139, pp. 80–87, 2018.
- [137] X. Cheng, M. Li, and Y. Wang, “An analytical model for current–voltage characteristics of AlGaN/GaN HEMTs in presence of self-heating effect,” *Solid-State Electronics*, vol. 54, no. 1, pp. 42–47, 2010.
- [138] K. Shirakawa, H. Oikawa, T. Shimura, T. Kawasaki, Y. Ohashi, T. Saito, and Y. Daido, “An approach to determining an equivalent circuit for HEMTs,” *IEEE Transactions on Microwave Theory and Techniques*, vol. 43, no. 3, pp. 499–503, 1995.

- [139] D. A. Frickey, "Conversions between S, Z, Y, H, ABCD, and T parameters which are valid for complex source and load impedances," *IEEE Transactions on Microwave Theory and Techniques*, vol. 42, no. 2, pp. 205–211, 1994.
- [140] S. Vitanov, V. Palankovski, S. Maroldt, and R. Quay, "High-temperature modeling of AlGa<sub>N</sub>/Ga<sub>N</sub> HEMTs," *Solid-State Electronics*, vol. 54, no. 10, pp. 1105–1112, 2010.
- [141] M. A. Alim, A. A. Rezazadeh, and C. Gaquiere, "Thermal characterization of DC and small-signal parameters of 150 nm and 250 nm gate-length AlGa<sub>N</sub>/Ga<sub>N</sub> HEMTs grown on a SiC substrate," *Semiconductor Science and Technology*, vol. 30, no. 12, pp. 1–10, 2015.
- [142] J. L. Hudgins, G. S. Simin, E. Santi, and M. A. Khan, "An assessment of wide bandgap semiconductors for power devices," *IEEE Transactions on Power Electronics*, vol. 18, no. 3, pp. 907–914, 2003.
- [143] K. Shenai, R. S. Scott, and B. J. Baliga, "Optimum semiconductors for high-power electronics," *IEEE Transactions on Electron Devices*, vol. 36, no. 9, pp. 1811–1823, 1989.
- [144] M. Ahmed, "Effects of sintering on Au/Ti/GaAs Schottky barrier submicron metal-semiconductor field-effect transistors characteristics," *Journal of Vacuum Science & Technology B: Microelectronics and Nanometer Structures Processing, Measurement, and Phenomena*, vol. 16, no. 4, pp. 2034–2037, 1998.
- [145] A. B. Khan, M. Sharma, M. Siddiqui, and S. Anjum, "Performance analysis of AC and DC characteristics of AlGa<sub>N</sub>/Ga<sub>N</sub> HEMT at various temperatures," *Transactions on Electrical and Electronic Materials*, pp. 1–6, 2018.
- [146] I. Batarseh and A. Harb, "Review of switching concepts and power semiconductor devices," in *Power Electronics*. Springer, 2018, pp. 25–91.



- [147] “12 W/mm AlGa<sub>N</sub>-Ga<sub>N</sub> HFETs on silicon substrates, author=Johnson, JW and Piner, EL and Vescan, A and Therrien, R and Rajagopal, P and Roberts, JC and Brown, JD and Singhal, S and Linthicum, KJ,” *IEEE Electron Device Letters*, vol. 25, no. 7, pp. 459–461, 2004.
- [148] D. Ducatteau, A. Minko, V. Hoel, E. Morvan, E. Delos, B. Grimbert, H. Lahreche, P. Bove, C. Gaquiere, J. De Jaeger *et al.*, “Output power density of 5.1/W/mm at 18 GHz with an AlGa<sub>N</sub>/Ga<sub>N</sub> HEMT on Si substrate,” *IEEE Electron Device Letters*, vol. 27, no. 1, pp. 7–9, 2006.
- [149] D. Marti, S. Tirelli, A. R. Alt, J. Roberts, and C. Bolognesi, “150-GHz cutoff frequencies and 2-W/mm output power at 40 GHz in a millimeter-wave AlGa<sub>N</sub>/Ga<sub>N</sub> HEMT technology on silicon,” *IEEE Electron Device Letters*, vol. 33, no. 10, pp. 1372–1374, 2012.
- [150] K. Ma, N. He, M. Liserre, and F. Blaabjerg, “Frequency-domain thermal modeling and characterization of power semiconductor devices,” *IEEE Transactions on Power Electronics*, vol. 31, no. 10, pp. 7183–7193, 2016.
- [151] M. Nazari, B. L. Hancock, E. L. Piner, and M. W. Holtz, “Self-heating profile in an AlGa<sub>N</sub>/Ga<sub>N</sub> heterojunction field-effect transistor studied by ultraviolet and visible micro-Raman spectroscopy,” *IEEE Transactions on Electron Devices*, vol. 62, no. 5, pp. 1467–1472, 2015.
- [152] J. L. Awange, B. Paláncz, R. H. Lewis, and L. Völgyesi, “Particle swarm optimization,” in *Mathematical Geosciences*. Springer, 2018, pp. 167–184.
- [153] F. M. Yigletu, S. Khandelwal, T. A. Fjeldly, and B. Iñiguez, “Compact charge-based physical models for current and capacitances in AlGa<sub>N</sub>/Ga<sub>N</sub> HEMTs,” *IEEE Transactions on Electron Devices*, vol. 60, no. 11, pp. 3746–3752, 2013.
- [154] M. M. Ahmed, “Abrupt negative differential resistance in ungated GaAs FET’s,” *IEEE Transactions on Electron Devices*, vol. 44, no. 11, pp. 2031–2033, 1997.

- [155] W. Tan, M. Uren, P. Fry, P. Houston, R. Balmer, and T. Martin, “High temperature performance of AlGaN/GaN HEMTs on Si substrates,” *Solid-State Electronics*, vol. 50, no. 3, pp. 511–513, 2006.